

Computational Modeling of Turbulent Ethanol Spray Flames in a Hot Diluted Coflow using OpenFOAM

Tariq Ahmed Abul Kalam Azad

Master of Science Thesis
P&E Report Number: 2686

Computational Modeling of Turbulent Ethanol Spray Flames in a Hot Diluted Coflow using OpenFOAM

MASTER OF SCIENCE THESIS

For the degree of Master of Science in Mechanical Engineering
Track - Sustainable Process and Energy Technology at Delft University of
Technology

Tariq Ahmed Abul Kalam Azad

August 27, 2015

Faculty of Mechanical, Maritime and Materials Engineering (3mE) · Delft University of
Technology

DELFT UNIVERSITY OF TECHNOLOGY
DEPARTMENT OF PROCESS AND ENERGY TECHNOLOGY

The undersigned hereby certify that they have read and recommend to the Faculty of Mechanical, Maritime and Materials Engineering (3mE) for acceptance of a thesis entitled
COMPUTATIONAL MODELING OF TURBULENT ETHANOL SPRAY FLAMES IN A HOT DILUTED
COFLOW USING OPENFOAM

by

TARIQ AHMED ABUL KALAM AZAD

in partial fulfilment of the requirements for the Degree of
MASTER OF SCIENCE MECHANICAL ENGINEERING

Dated: August 27, 2015

Supervisor(s):

Prof. Dr. D.J.E.M. Roekaerts

Likun Ma, Msc

Reader(s):

Dr. ir. Mark J. Tummers

Dr. Arvind Gangoli Rao

Acknowledgements

Pursuing Master's at TU Delft was an important decision of my life and I would like to thank these people for helping me achieve this formidable task of obtaining Master's degree from TU Delft.

Firstly, I would like to express my sincere gratitude to my research supervisor Prof. Dr. Dirk Roekaerts for his immense support and guidance towards the completion of my thesis with his invaluable knowledge on combustion and multiphase flows. I would also like to thank my daily supervisor, Mr. Likun Ma for his enthusiasm and technical suggestions in shaping the course of my project. He is always willing to discuss any doubts and give feedback in my research work. I would also like to thank the examination committee for taking their time in reading my work and evaluating it. This thesis work was sponsored by NWO Physical Sciences for the use of supercomputer facilities.

Finally I would like to thank my parents for their faith in my life's decisions and being a constant moral support throughout my life. I wouldn't have been able to achieve any of this without their love and motivation. I would also like to thank all my friends here in Delft and India for making my life a lot easier.

Abstract

Spray combustion finds a wide range of application in gas turbines, internal combustion engines, industrial furnaces, etc. In turbulent spray combustion, liquid fuel is injected into the combustion chamber in the form of droplets. In order to improve the combustion efficiency and to reduce the thermal NO_x emissions released during combustion, spray combustion could be operated in flameless mode. In a flameless combustion, the oxidizer is mixed with recirculated hot combustion gases to preheat and to dilute it. The dilution of oxidizer results in lower peak combustion temperature which reduces the NO_x emissions and oxidizer preheating improves the thermal efficiency of combustion. In order to fully understand the combustion mechanics for its effective implementation in various applications, numerical simulations of flameless turbulent spray combustion are potentially useful because simulations are cost effective and serve as basis for further experimental studies based on the validation of numerical models.

Turbulent spray combustion is a complex phenomenon involving two phases namely the gaseous phase and liquid phase. These two phases interact with each other through mass, momentum and energy transfer between them. This is complicated further by the interaction between the turbulence in the flow field and chemistry of the reacting species. Hence simplified models are necessary to simulate and understand the phenomenon of turbulent spray combustion. In this thesis, numerical validation study of turbulent ethanol spray flame using open-source software package OpenFOAM is carried out for the experiments done in Delft Spray-in-Hot-Coflow (DSHC) burner operated in flameless mode. The modeling approach used is Reynolds Averaged Navier Stokes simulations (RANS) with Eulerian-Lagrangian framework for the continuous phase and discrete phase respectively.

Models like evaporation and turbulence models used in the sprayFoam solver are optimized for the spray combustion and validated with experimental data for one flame. The evaporation models studied are Gradient diffusion model and Spalding model. It is found that Gradient diffusion model gives better prediction of droplet properties at higher axial locations than Spalding model. The standard and realizable $k-\varepsilon$ model turbulence models comparative analysis showed that standard $k-\varepsilon$ model has much better gas phase temperature prediction than realizable $k-\varepsilon$ model due to the dependence of combustion model (Partially Stirred Reactor model) on the turbulence mixing frequency, ε/k . These optimized models are extended to simulation of H_I and H_{III} flames. The peak gas phase temperature was under-predicted by the PaSR model. The results showed the importance of analyzing the different initial spray conditions.

Table of Contents

List of Figures.....	III
List of Tables.....	VII
Chapter 1.....	1
Introduction.....	1
1.1 Biofuels	1
1.1.1 Ethanol.....	1
1.2 Flameless Combustion	2
1.3 Turbulent spray combustion.....	3
1.4 Computational approaches	4
1.5 Experimental setup.....	5
1.5.1 Burner design configuration	5
1.5.2 Measurement techniques	7
1.5.3 Experimental data	7
1.6 Research Objective.....	8
1.7 Outline.....	8
Chapter 2.....	9
Computational Model for Spray Combustion.....	9
2.1 Gas Phase equations	9
2.2 Turbulence Models.....	10
2.2.1 Standard k- ϵ model	11
2.2.2 Realizable k- ϵ model	11
2.3 Chemical Kinetics	12
2.4 Combustion Model.....	13
Partially Stirred Reactor Model	13
2.5 Spray/Discrete Phase modeling.....	16
2.5.1 Droplet Motion	17
2.5.2 Injection Model.....	19
2.5.3 Evaporation model.....	22
Chapter 3.....	27
OpenFOAM	27
3.1 sprayFoam	27

3.1.1 Numerical Schemes	28
3.2 Solutions convergence check for H _{II} flame simulation	30
3.3 Postprocessing	33
Chapter 4.....	35
Results and Discussion	35
4.1 Injector pressure optimization	37
4.2 Model Comparisons	47
4.2.1 Evaporation model.....	47
4.2.2 Turbulence model.....	52
4.3 MILD combustion phenomenon in H _{II} flame	53
4.4 Effect of coflow conditions on ethanol spray flames	55
4.4.1 H _I flame	55
4.4.2 H _{III} flame.....	60
4.4.3 Comparison between H _I , H _{II} and H _{III} flames	64
Chapter 5.....	67
Conclusions and Recommendations	67
Bibliography	71
Appendix	75
A.1 Model comparison for Chemical kinetics	75
A.2 Pressure optimization with Spalding Evaporation model	79
A.3 Spray properties used in simulations	82

List of Figures

Figure 1.1 Green House emissions for ethanol as transportation fuel- gCO ₂ eq/km (Nelson, 2014).....	2
Figure 1.2 Conventional (top) and Flameless (bottom) mode for gas burner (Milani & Wüning, 2002).....	3
Figure 1.3 DSHC Burner Schematic (Correia Rodrigues H. , Tummers, Roekaerts, & van Veen, 2015)	6
Figure 2.1 Partially Stirred Reactor Model Reaction Scheme (Karrholm, 2008)	14
Figure 2.2 Reaction and mixing procedure	15
Figure 2.3 Different flow regimes during spray injection process (Jenny, Roekaerts, & Beishuizen, 2012)	20
Figure 3.1 Convergence check for one-step mechanism using gas phase temperature.....	31
Figure 3.2 Convergence check for one-step mechanism using ethanol mass fraction.....	32
Figure 3.3 Convergence check for one-step mechanism using pressure in the flow.....	32
Figure 4.1 DSHC Burner mesh configuration and boundary conditions	35
Figure 4.2 Spray angle configuration for a Cone nozzle injector (Forums).....	37
Figure 4.3 Radial profiles of mean droplet axial velocity for elevations of 8mm to 15 mm at 4 bar injection pressure in the injection model.....	39
Figure 4.4 Radial profiles of mean droplet axial velocity for elevations of 20mm to 40 mm at 4 bar injection pressure in the injection model.....	39
Figure 4.5 Radial profiles of mean droplet radial velocity for elevations of 8mm to 15 mm at 4 bar injection pressure in the injection model.....	40
Figure 4.6 Radial profiles of mean droplet radial velocity for elevations of 20mm to 40 mm at 4 bar injection pressure in the injection model.....	40
Figure 4.7 Sauter Mean Diameter(d_{32}) of the droplets at 4 bar injection pressure in the injection model	41
Figure 4.8 Radial profiles of mean droplet axial velocity for elevations of 8mm to 15 mm at 6 bar injection pressure in the injection model.....	42
Figure 4.9 Radial profiles of mean droplet axial velocity for elevations of 20mm to 40 mm at 6 bar injection pressure in the injection model.....	42

Figure 4.10 Radial profiles of mean droplet radial velocity for elevations of 8mm to 15 mm at 6 bar injection pressure in the injection model.....	43
Figure 4.11 Radial profiles of mean droplet radial velocity for elevations of 20mm to 40mm at 6 bar injection pressure in the injection model.....	43
Figure 4.12 Sauter Mean Diameter(d_{32}) of the droplets at 6 bar injection pressure in the injection model	44
Figure 4.13 Radial profiles of mean droplet axial velocity for elevations of 8mm to 15 mm at 10 bar injection pressure in the injection model.....	45
Figure 4.14 Radial profiles of mean droplet axial velocity for elevations of 20mm to 40mm at 10 bar injection pressure in the injection model.....	45
Figure 4.15 Radial profiles of mean droplet radial velocity for elevations of 8mm to 15mm at 10 bar injection pressure in the injection model.....	46
Figure 4.16 Radial profiles of mean droplet radial velocity for elevations of 20mm to 40mm at 10 bar injection pressure in the injection model.....	46
Figure 4.17 Sauter Mean Diameter(d_{32}) of the droplets at 10 bar injection pressure in the injection model	47
Figure 4.18 Gas phase temperature comparison for the evaporation models.....	49
Figure 4.19 Gas phase temperature comparison for the evaporation models.....	49
Figure 4.20 Radial profiles of mean droplet axial velocity for Spalding model at elevations of 30-40mm with 6 bar injection pressure in the injection model	50
Figure 4.21 Radial profiles of mean droplet radial velocity for Spalding model at elevations of 30-40mm with 6 bar injection pressure in the injection model.....	51
Figure 4.22 SMD for the Spalding model with 6 bar injection pressure in the injection model	51
Figure 4.23 Gas phase temperature profile comparison between the turbulence models for different elevations	52
Figure 4.24 Gas phase velocity profile comparison between the turbulence models for different elevations	53
Figure 4.25 Gas phase temperature profile for H_{II} flame at elevation of 50mm and 60mm ...	54
Figure 4.26 Gas phase Temperature profile for the H_I flame at different elevations	56
Figure 4.27 Gas phase velocity profile for the H_I flame at different elevations.....	56
Figure 4.28 Radial profiles of mean droplet axial velocity for elevations of 8mm to 15mm for H_I flame with 6.5 bar injection pressure in the injection model.....	57

Figure 4.29 Radial profiles of mean droplet axial velocity for elevations of 20mm to 35mm for H _I flame with 6.5 bar injection pressure in the injection model	58
Figure 4.30 Radial profiles of mean droplet radial velocity for elevations of 8mm to 15mm for H _I flame with 6.5 bar injection pressure in the injection model	58
Figure 4.31 Radial profiles of mean droplet radial velocity for elevations of 20mm to 35mm for H _I flame with 6.5 bar injection pressure in the injection model	59
Figure 4.32 Droplet SMD for H _I flame with 6.5 bar injection pressure in the injection model	59
Figure 4.33 Gas phase Temperature profile for the H _{III} flame at different elevations	60
Figure 4.34 Gas phase velocity profile for the H _{III} flame at different elevations.....	61
Figure 4.35 Radial profiles of mean droplet axial velocity for elevations of 8mm to 15mm for H _{III} flame with 6.5 bar injection pressure in the injection model	62
Figure 4.36 Radial profiles of mean droplet axial velocity for elevations of 20mm to 35mm for H _{III} flame with 6.5 bar injection pressure in the injection model	62
Figure 4.37 Radial profiles of mean droplet radial velocity for elevations of 8mm to 15mm for H _{III} flame with 6.5 bar injection pressure in the injection model	63
Figure 4.38 Radial profiles of mean droplet radial velocity for elevations of 20mm to 35mm for H _{III} flame with 6.5 bar injection pressure in the injection model	63
Figure 4.39 Droplet SMD for H _{III} flame with 6.5 bar injection pressure in the injection model	64
Figure 4.40 Gas phase Temperature profile comparison between H _I , H _{II} and H _{III} flames.....	65
Figure A.1 Gas phase temperature convergence plot for detailed mechanism	76
Figure A.2 Ethanol mass fraction convergence plot for detailed mechanism.....	76
Figure A.3 Gas phase Temperature profile comparison for the reaction mechanisms at different elevations	77
Figure A.4 Gas phase velocity profile comparison for the reaction mechanisms at different elevations.....	78
Figure A.5 Radial profiles of mean droplet axial velocity for elevations of 8mm to 15 mm at 10 bar injection pressure in the injection model with Spalding model	79
Figure A.6 Radial profiles of mean droplet axial velocity for elevations of 20mm to 40mm at 10 bar injection pressure in the injection model with Spalding model	80
Figure A.7 Radial profiles of mean droplet radial velocity for elevations of 8mm to 15 mm at 10 bar injection pressure in the injection model with Spalding model	80

Figure A.8 Radial profiles of mean droplet radial velocity for elevations of 20mm to 40mm at 10 bar injection pressure in the injection model with Spalding model 81

Figure A.9 SMD for the Spalding model with 10 bar injection pressure in the injection model 81

List of Tables

Table 4.1 Experimental boundary conditions for the spray and coflow.....	36
--	----

Chapter 1

Introduction

1.1 Biofuels

We all know that world's total energy consumption is increasing due to population growth and technological innovations. According to International Energy Agency, about 81% of the total world energy consumed comes from fossil fuels (Agency, 2010). The fossil fuel combustion creates pollutants in the form of NO_x and SO_x emissions which are detrimental to environment. Apart from NO_x and SO_x , the other major pollutant is in the form of carbon dioxide. Carbon dioxide is a greenhouse gas emission which affects environment in the form of global warming. The release of CO_2 from burning fossil fuels could be limited by using various carbon dioxide capture techniques like carbon dioxide capture and sequestration (CCS). These emissions are controlled in the industry by flue gas treatment to minimize the impact on environment but it poses economic constraints. The reserves of fossil fuels are diminishing and in the near future, we may run out of them too. Hence, nowadays, there is much more focus on sustainable energy production like biofuels to have a shift from the conventional fuels. These biofuels come from biomass which is nothing but plant based materials like lignocellulose. The most commonly used biofuels are bioethanol and biodiesel. The fuel focused in this thesis is ethanol and hence will be briefly explained.

1.1.1 Ethanol

Bioethanol is usually produced by the fermentation of sugar/starch containing materials like sugarcane, beet, sugar molasses, etc. Figure 1.1, which is extracted from a review report of the organization of European oil refineries, predicts the future bioethanol options which can be achieved to have a shift from the conventional to alternative fuels. The different fuel options for the future are given in the vertical axis and the horizontal axis gives the grams of carbon dioxide equivalent released by burning of various fuel options.

Carbon dioxide equivalent is a measure of the global warming potential of the different greenhouse emissions like methane and nitrous oxide as compared to the CO_2 emission. Since bioethanol is manufactured from biomass, the amount of greenhouse gases (GHG) emitted by burning the fuel is significantly lower than those of fossil fuels (Figure 1.1). The ethanol is usually used as vehicle fuels either in the form of pure alcohol or blended with gasoline. As we can see from Figure 1.1 which projects the future biofuel options, the amount of Carbon dioxide equivalent produced by combustion of ethanol manufactured from biomass like wood and sugarcane ($36\text{gCO}_2\text{eq}$) is less compared to combustion of conventional gasoline ($120\text{gCO}_2\text{eq}$). The most novel approach would be to use ethanol as fuel in industrial burners instead of using fossil oil or natural gas for firing.

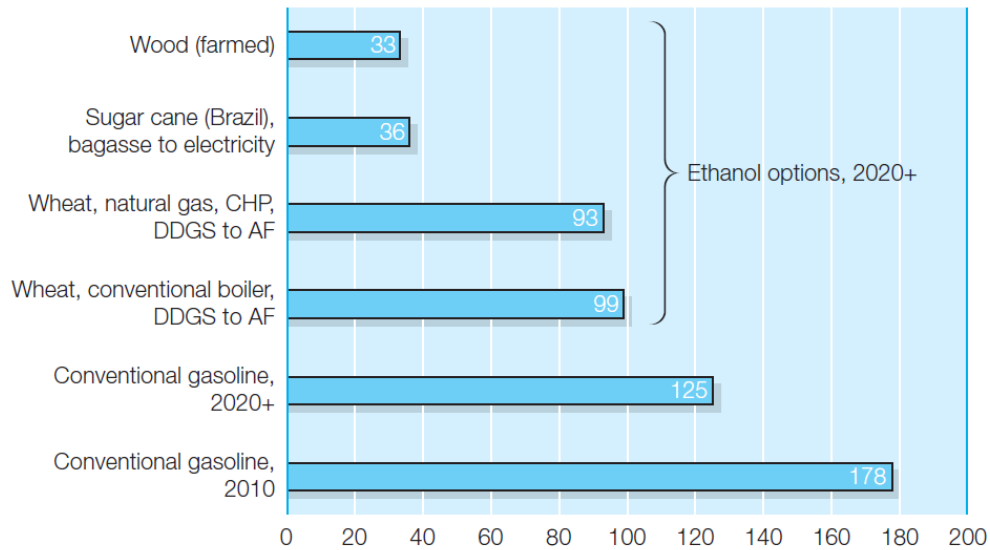


Figure 1.1 Green House emissions for ethanol as transportation fuel- gCO₂eq/km (Nelson, 2014)

The physical properties of bioethanol used for this study are (Haynes, 2015-2016)

Boiling point of ethanol = 351.65K

Self-Ignition temperature of ethanol = 638.15K

Heat of combustion = 1336.8kJ/mol

1.2 Flameless Combustion

In conventional combustion process, fuel and oxidizer mix together and burn releasing heat and radiation (exothermic reaction). A lot of research is going on in the field of combustion to optimize the combustion systems to reduce the amount of NO_x released during burning the fuel and to increase the thermal efficiency (Katsuki & Hasegawa, 1998). One of those methods is by using flameless combustion. Flameless combustion, also referred to as Moderate and Intense Low-oxygen Dilution (MILD) combustion, is a method in which air is preheated above auto-ignition temperature of the fuel as well as diluted by the hot exhaust gases thereby creating a uniform temperature distribution over the combustion chamber. Also, the maximum flame temperature (adiabatic flame temperature) achieved is lower than in the conventional flame mode, thereby reducing the NO_x emissions. Using the preheated air increases the thermal efficiency of the combustion system (Wüning & Wüning, 1997). In a flameless combustion, there is no visible flame front due to the flame luminous emission being much lesser than the conventional flame (Cavalierea & Joannon, 2004). Figure 1.2 shows the basic difference between a conventional flame and flameless combustion.

According to A. Cavaliere and M. De Joannon “A combustion process is named MILD when the inlet temperature of the reactant mixture is higher than mixture self-ignition temperature whereas maximum allowable temperature increase with respect to inlet temperature during

combustion is lower than mixture self-ignition temperature (in Kelvin)” (Cavalierea & Joannon, 2004)

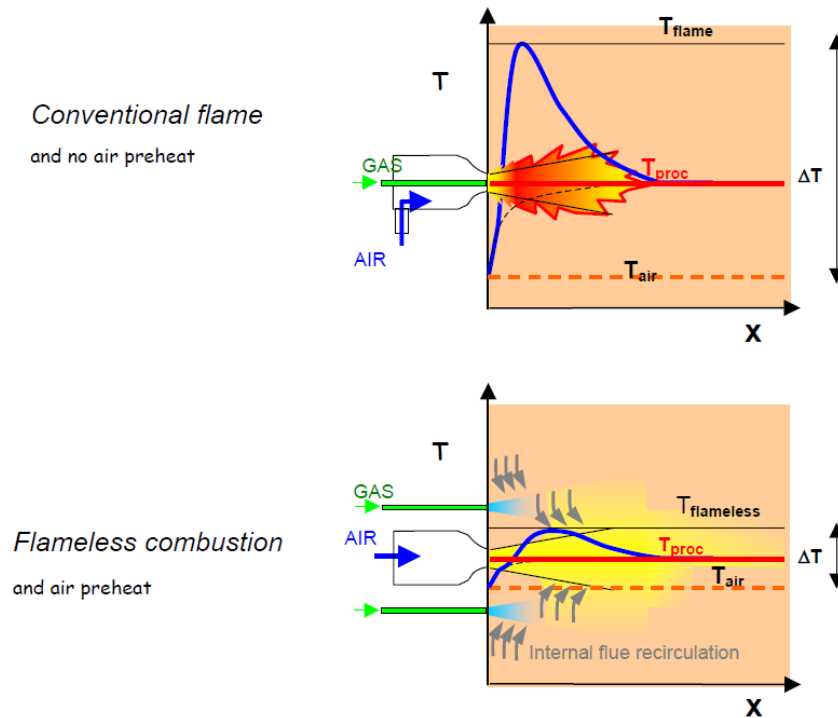


Figure 1.2 Conventional (top) and Flameless (bottom) mode for gas burner (Milani & Wüning, 2002)

1.3 Turbulent spray combustion

In turbulent spray combustion, liquid fuel is injected into the gaseous environment in the form of droplets. These droplets break into smaller ones by the process of atomization thereby increasing the surface area of the droplets for effective combustion. Various studies have been done in the field of turbulent spray combustion using different computational approaches especially LES and RANS (see Section 1.4). Since spray is a two phase flow with liquid in the form of droplets as discrete/dispersed phase and gas as continuous phase, two approaches are used to describe the two phase flow aspects (Rochaya, 2007) – Eulerian-Eulerian approach and Eulerian-Lagrangian approach. Eulerian-Eulerian approach uses Eulerian formulation for both the continuous phase and discrete phase while Eulerian-Lagrangian approach uses Eulerian formulation for the continuous phase and Lagrangian formulation for the discrete phase (where individual droplets are tracked). The most commonly used approach is the Eulerian-Lagrangian one and this is used in the current thesis study.

A number of research papers on turbulent jet flames of dilute sprays for ethanol and acetone have been published. They include both experimental results and numerical validation for those experiments using both RANS and LES. Experimental work was conducted by Masri et al. (Masri & Gounder, 2010) using piloted jet spray of ethanol or acetone. The conclusion of

their experiments was that with increasing jet velocity, temperature fields show a varying behavior due to blow-off being achieved.

Numerical studies by different research groups were conducted based on these experimental results. In the study of Chigrui et al. (Chigrui, Masri, Sadiki, & Janicka, 2013), ethanol spray combustion was modeled using LES approach with Flamelet Generated Manifold (FGM) combustion model and fuel injected in polydisperse mode. The conclusion of the study was that heat loss due to evaporation should be implemented in the FGM model. A comparative numerical study based on four research groups was made by Heye et al. (Heye, Kourmatzis, Raman, & Masri, 2014). The conclusions of the comparative study were that the flamelet model gave accurate gas phase temperature predictions and the study recommended that the sensitivity of the different evaporation models has to be analyzed. Also the authors of this study preferred RANS over LES even though RANS couldn't represent flame speed in the simulations because RANS was computationally cheaper than LES.

In a further study on jet spray flames by Filho et al. (Filho, Fukumasu, & Krieger, 2013), RANS simulation of ethanol spray was done with combustion modeled by mixture fraction-joint PDF method. The conclusion of the research was that the model was unable to predict accurately gas phase temperature and droplet velocities downstream of the nozzle. This discrepancy is attributed to the combustion model not considering temperature reduction by evaporation on the species reaction rates.

In the study by Ma et al. (Ma, Zhu, Correia Rodrigues, Tummers, Roekaerts, & van der Meer, 2013), detailed numerical simulation of ethanol spray combustion for the Delft Spray-in-Hot-Coflow (DSHC) burner was carried out using ANSYS Fluent (RANS simulations). In that study, the combustion model employed was Steady Laminar Flamelet model with Marinov mechanism for the ethanol oxidation. The conclusion of this study was that the Flamelet model was not able to correctly predict the flame lift-off because extinguished flamelets were not included in the model. The accelerated evaporation of droplets caused by the high temperature of the coflow creates a high strain region near the nozzle intensifying the prediction problem further (Ma, Zhu, Correia Rodrigues, Tummers, Roekaerts, & van der Meer, 2013).

In a further study by Ma et al. (Ma, Naud, & Roekaerts, 2015), Lagrangian-Lagrangian approach was employed in which joint probability density function (PDF) of the gas phase and the discrete phase properties were solved by Monte Carlo method. The turbulent-chemistry interaction was modeled by Flamelet Generated Manifold (FGM) model. The conclusion of the study was that the gas phase temperature was over-predicted near the axial region as the two-dimensional adiabatic FGM table used was not able to account for the enthalpy loss created by the droplet evaporation.

1.4 Computational approaches

Turbulent spray combustion is a complex process involving multiphase namely the gaseous phase and liquid phase (discrete phase) and the interaction between these two phases. Also

since ethanol is a liquid fuel and injected as a spray in the experiment, the physical phenomenon associated with sprays like liquid sheet breakup, atomization, evaporation, etc. have to be given significant attention too. In multiphase (two phase) combustion, there is an influence of continuous phase and dispersed phase turbulence on each other by means of momentum exchange through the droplet boundaries (Jenny, Roekaerts, & Beishuizen, 2012). There is also an interaction between the turbulence and chemistry (reaction rates of the chemical species) which makes it even more complicated.

The numerical simulation of such a complex process is the main objective of this thesis study and there are different computational approaches to solving the turbulent combustion in general. The different approaches are (Poinso & Veynante, 2011)

1. Reynolds Averaged Navier Stokes simulations (RANS)
2. Large Eddy Simulations (LES)
3. Direct Numerical Simulations (DNS)

In RANS simulations, only mean values of the quantities are calculated based on density weighted averaging. The advantage of using RANS simulation is that, a coarse numerical grid can be used and the computational time is not high as compared to the other two approaches. The disadvantage is that there are closure problems associated with the Reynolds averaged conservation equations and they require turbulence models like Reynolds stress model or k- ϵ model to close the unclosed terms. RANS simulation is the main focus of this study and it will be explained in detail in Chapter 2.

In LES, the turbulent large scale motions are solved directly but the turbulent small scale motions are modeled by subgrid closure models (filtered equations) and in DNS, all the conservation equations are directly solved without any need of models and all the turbulent scales are fully resolved (very high computational costs).

1.5 Experimental setup

The experimental work done by Correia Rodrigues (Correia Rodrigues H. , Tummers, Roekaerts, & van Veen, 2015) are the basis of validation for this thesis work. Various experiments were done by Correia Rodrigues in the Delft Spray-in-Hot-Coflow (DSHC) burner and the experimental data is used for the validation of numerical simulation results using OpenFOAM.

1.5.1 Burner design configuration

The schematic of the DSHC burner used for the study of turbulent spray combustion is given in Figure 1.3. The burner consists of a pressure-swirl hollow cone atomizer which is used to inject a spray of fine fuel droplets. The commercial atomizer used in the experimental study is Delavan WDA 0.5GPH. The outer diameter of the orifice used in the atomizer is of 0.210mm with an angle of 60° for the spray. This orifice is mounted on a 2mm inner diameter pipe made of stainless steel through which ethanol (C₂H₅OH) is fed into the atomizer. The burner has two configurations – hot-dilute coflow and air coflow depending on the type of input

conditions used in the secondary burner. Hot-dilute coflow condition is used to operate the burner in flameless mode and air coflow for the conventional mode.

From Figure 1.3, we can see that the burner has a secondary burner operating in Dutch Natural Gas (DNG) to provide hot-diluted coflow gases. The reason for having a secondary burner instead of recirculating burnt hot gases back into the burner is that there is more control over the dilution and temperature of the hot coflow than by direct recirculation. This is assisted by the two perforated plates above the secondary burner which also contribute to the enthalpy loss of coflow by radiation. The cylinder above the secondary burner has a length of 270mm and inner diameter of 160mm. The air inflow is supplied through four inlets at the bottom of the burner and the perforated plates and honeycomb structure below the secondary burner are used to give the air flow, a homogenous and isotropic turbulence before it reaches the secondary burner (Correia Rodrigues H. , Tummers, Roekaerts, & van Veen, 2015). The composition of DNG used in the secondary burner is Methane-81.3%, Nitrogen-14.4%, Ethane-3.7% and trace species-0.6% by volume.

The air after entering the bottom of the burner through the inlets, reaches the secondary burner where DNG is injected. The air reacts with the natural gas and combustion products are produced which move up through the top of the burner and reach the spray region. Thus hot-diluted coflow is produced by the secondary burner which then reacts with the injected fuel droplets through the atomizer to operate the burner in flameless mode. If the DNG is not injected into the secondary burner, DSHC burner operates in conventional mode.

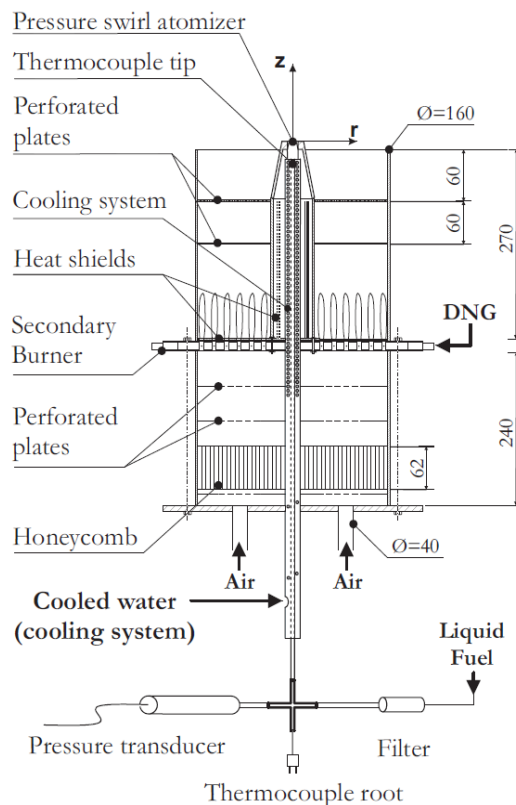


Figure 1.3 DSHC Burner Schematic (Correia Rodrigues H. , Tummers, Roekaerts, & van Veen, 2015)

1.5.2 Measurement techniques

There are five different measurement techniques used in the DSHC experimental study: Laser Doppler Anemometry (LDA), Phase Doppler Anemometry (PDA), Coherent Anti-Stokes Raman Spectroscopy (CARS), High speed visualization and Flue gas analyzer.

LDA is used to measure axial and radial gas phase velocity components where no droplets are present. The LDA uses two beams of 10W Continuum Argon-ion laser obtained by splitting the single laser beam so that the two beams have same phase difference and frequency. Aluminum oxide (Al_2O_3) particles of size $1\mu\text{m}$ diameter are added into the air so that the laser beams near the orifice exit get reflected by the Al_2O_3 particles and is captured by photo detectors. The reflected light has variation in frequency which allows measuring a component of particle velocity from the Doppler shift frequency (Durst, Melling, & Whitelaw, 1981).

PDA is used to measure axial and radial droplet velocity components and their size distributions in the spray region. The setup of PDA is similar to that of the LDA but the receiver / photo detector is placed at a certain scattering angle (ϕ) (Correia Rodrigues H. , Tummers, Roekaerts, & van Veen, 2015) from the direction of the laser beam. When the split laser beam hits the droplet in the liquid spray region, the light gets scattered by the droplet particles and is captured by the photo detectors kept at the scattering angle. The droplet velocity is calculated from the Doppler shift frequency.

CARS system is used to measure gas phase temperature in the coflow exit and the spray region. CARS spectroscopy uses three laser beams-a pump beam, probe beam and one Stokes beam (Warnatz & Maas, 2006) to produce an anti-Stokes signal. When the frequency difference between the pump beam and Stokes beam reaches the natural frequency of the oscillator, the induced electrons change the optical property of the medium. So when the probe beam passes through this altered medium, its frequency is affected by the pump and Stokes beam frequency thereby producing the anti-Stokes emission. (Warnatz & Maas, 2006).

In case of high speed visualization, liquid jet breakup is visualized by means of a light source and a high speed motion capture camera. It gives a real time visualization of fuel sheet breakup, atomization, evaporation, etc. Flue gas analyzer, Testo 355 is used to measure the oxygen volume fraction in the gas phase.

1.5.3 Experimental data

The results from the experiments conducted by Correia Rodrigues on the DSHC burner are used to validate the numerical simulations. As mentioned before, the experimental cases include hot-diluted coflow and air coflow. In this numerical study, the hot-diluted coflow case, H_{II} performed on the burner is studied and finally, extended to H_{I} and H_{III} flames. These three flames use secondary burner as explained in the experimental setup before and have different coflow properties.

The boundary conditions for the coflow and for the fuel injected through the pressure-swirl atomizer of the DSHC burner for all the three cases will be explained in Chapter 4. These experimental parameters are used as starting boundary conditions for the modeled mesh as well as in the spray properties of the sprayFoam solver (explained in detail in Chapter 3).

These boundary conditions are used in the solver to set various other parameters like gas phase temperature, radial and axial velocity components and droplet axial, radial velocity components, droplet size distribution, etc.

1.6 Research Objective

As mentioned above in the introduction, turbulent spray combustion is a complex phenomenon involving two phases and modeling this is a challenging task. In this research thesis, the objective is to perform RANS simulations of dilute turbulent spray combustion for ethanol using sprayFoam module of open source CFD package OpenFOAM and validate the simulation results with the help of experimental data. In this aspect, sprayFoam solver will be optimized for H_{II} case by varying parameters like injection pressure of the fuel and models like turbulence model and evaporation model to obtain the optimized settings for the solver to validate the experimental results. The models will be analyzed to study the influence of the turbulence, evaporation, mass flow rate of the fuel on the temperature profiles and velocity components of both the gas phase and discrete phase.

The combustion model that will be used to model the interaction between the turbulence and chemistry is Partially Stirred Reactor (PaSR) model. The chemical reaction mechanism of ethanol that will be considered for the simulation is global reaction mechanism (K. Westbrook & L. Dryer, 1981) and detailed reaction mechanism (38 species and 228 reactions) by Roehl and Peters (Röhl & Peters, 2009) and the effect of the reaction mechanisms on the temperature profiles will be studied. Finally all these optimized solver settings will be extended to H_I and H_{III} flames based on different coflow conditions and a comparison between these flames will be made.

1.7 Outline

The discussions made in this chapter give an overall view of the theory behind spray combustion, various researches undergone in that field, etc. A brief overview of the numerical approaches used for the simulation of spray combustion and a description of experimental setup, which is the basis of validation for this study is also presented. Chapter 2 describes the various equations necessary to model the two phase flow and the interaction between them in turbulent spray combustion. Chapter 3 deals with the Computational Fluid Dynamics (CFD) software used for the study and general working of the software. The solver is optimized for turbulent spray combustion by studying the effects of various models on combustion behavior for H_I , H_{II} and H_{III} flames by validation with reference experimental data. These results and discussions are explained in Chapter 4. The conclusions based on the numerical study and recommendations for further studies are listed in Chapter 5

Chapter 2

Computational Model for Spray Combustion

As mentioned in Chapter 1, turbulent dilute spray combustion is a complex process involving the gas phase and the liquid phase and the interaction between these two phases. The gas phase is modeled using Eulerian approach and the liquid phase is modeled using Lagrangian approach. Since there is two-way coupling between the two phases, there are additional source terms in the Eulerian gas phase conservation equations to account for the phase interaction (Filho, Fukumasu, & Krieger, 2013). In this chapter, the different conservation equations for the gas phase, turbulence models to close the mean terms in the conservation equations, interaction between the turbulence and chemistry, Lagrangian droplet constitutive equations are given.

2.1 Gas Phase equations

In this thesis study, the numerical simulations are based on RANS (Reynolds Averaged Navier Stokes) equations. The usual conservation equations are density (Favre) averaged to obtain the mean quantities. The advantages of using RANS simulations are explained in Chapter 1. The basic equations required to describe the flow are mass, momentum and energy conservation equations. Since combustion involves chemical reactions, there are additional conservation equations for the chemical species also (Filho, Fukumasu, & Krieger, 2013).

$$\frac{\partial(\bar{\rho})}{\partial t} + \frac{\partial(\bar{\rho}\tilde{u}_i)}{\partial x_i} = \bar{S}_{p,c} \quad (1)$$

$$\frac{\partial(\bar{\rho}\tilde{u}_j)}{\partial t} + \frac{\partial(\bar{\rho}\tilde{u}_i\tilde{u}_j)}{\partial x_i} = \left[-\frac{\partial\bar{p}}{\partial x_j} + \frac{\partial\bar{\tau}_{ij}}{\partial x_i} + \bar{\rho}g_j \right] - \frac{\partial(\bar{\rho}\widetilde{u_i''u_j''})}{\partial x_j} + \bar{S}_{p,u} \quad (2)$$

$$\frac{\partial(\bar{\rho}\tilde{\varphi}_k)}{\partial t} + \frac{\partial(\bar{\rho}\tilde{u}_i\tilde{\varphi}_k)}{\partial x_i} = \left[-\frac{\partial J_i}{\partial x_i} + \bar{\rho}\tilde{S}_k \right] - \frac{\partial(\bar{\rho}\widetilde{\varphi_k''u_j''})}{\partial x_j} + \bar{S}_{p,\varphi} \quad (3)$$

$$\frac{\partial(\bar{\rho}\tilde{h})}{\partial t} + \frac{\partial(\bar{\rho}\tilde{u}_i\tilde{h})}{\partial x_i} = \frac{\mu_t}{\sigma_t} \frac{\partial\tilde{h}}{\partial x_j} + \bar{S}_{p,h} \quad (4)$$

The equations (1), (2), (3), (4) represent the continuity, momentum, species and energy conservation equations. The terms ρ , p , h , φ , u , σ_t , τ , μ_t are the density, pressure, specific enthalpy, species mass fraction, velocity, turbulent Prandtl number, stress tensor and turbulent viscosity respectively. The subscripts 'i' and 'j' represent the components of the velocity vector and 'k' represent the species. The superscript '~' represents the Favre averaging and '-' represent the time averaging (Warnatz & Maas, 2006). The term $\bar{\rho}\tilde{S}_k$ in

equation (3) gives the mean chemical source term which is the species production and consumption by the chemical reaction.

The term $\bar{S}_{p,c}$, $\bar{S}_{p,u}$, $\bar{S}_{p,\phi}$, $\bar{S}_{p,h}$ in the above equations (1)-(4) represent the source terms introduced in the continuity, momentum, species and energy conservation equations respectively due to the two-way coupling which takes into account of the evaporation of the discrete phase.

The terms $\bar{\rho}\widetilde{u_i''u_j''}$, $\bar{\rho}\widetilde{\phi_k''u_j''}$, $\bar{\rho}\bar{S}_k$ in the conservation equations are the Reynolds stress tensor, turbulent scalar flux and mean source term respectively. These terms are the unknown values in the equations and need to be modeled. In order to solve the closure problem for the Reynolds stress tensor, the terms k and ε are calculated by two-equation model ' k - ε model'. The k - ε models employed in this numerical simulation study are the Standard k - ε model and the Realizable k - ε model.

Apart from these transport equations, also a thermodynamic equation of state is needed and a caloric equation of state relating enthalpy to temperature. For atmospheric pressure spray flame, the multicomponent ideal gas equations of state are used to describe the gas phase and, in caloric equation of state, we use values of specific heat from the thermodynamic database of Chemkin-II used in OpenFOAM.

2.2 Turbulence Models

The turbulence models are used to close the unknown Reynolds stress tensor in the density averaged Navier stokes equations in RANS simulations. Since there are two unknowns, k and ε , we need two equations to solve these terms. Hence the two-equation model ' k - ε model' is used in sprayFoam solver to calculate these values. This section describes the equations used to solve the unknown terms. The Reynolds stress tensor $\bar{\rho}\widetilde{u_i''u_j''}$ is given by Boussinesq relationship (5) (H.K.Versteeg & W.Malalasekera, 2007),

$$\bar{\rho}\widetilde{u_i''u_j''} = -\frac{2}{3}\bar{\rho}k\delta_{ij} - \frac{2}{3}\mu_t\frac{\partial\tilde{U}_k}{\partial x_k}\delta_{ij} + \mu_t\left(\frac{\partial\tilde{U}_i}{\partial x_j} + \frac{\partial\tilde{U}_j}{\partial x_i}\right) \quad (5)$$

where μ_t is the turbulent dynamic viscosity given by (6)

$$\mu_t = C_\mu\frac{k^2}{\varepsilon} \quad (6)$$

In equation (6), C_μ is a model constant, k is the turbulent kinetic energy, ε is the turbulent kinetic energy dissipation rate. The standard k - ε model is the most common model used in spray combustion studies and other model like realizable k - ε model were developed to improve the performance of certain flows like planar jets, rotational flows, etc.

2.2.1 Standard k - ε model

The Standard k - ε model is the most commonly used turbulence model in combustion studies. The equations for the model are (B.E.Launder & D.B.Spalding, 1972) (Standard k-epsilon model, 2005)

$$\frac{\partial(\bar{\rho}k)}{\partial t} + \frac{\partial(\bar{\rho}\tilde{u}_i k)}{\partial x_i} = \frac{\partial}{\partial x_j} \left[\left(\mu + \frac{\mu_t}{\sigma_k} \right) \frac{\partial k}{\partial x_j} \right] + P_k + P_b + S_k - \rho\varepsilon - Y_m \quad (7)$$

$$\frac{\partial(\bar{\rho}\varepsilon)}{\partial t} + \frac{\partial(\bar{\rho}\tilde{u}_i \varepsilon)}{\partial x_i} = \frac{\partial}{\partial x_j} \left[\left(\mu + \frac{\mu_t}{\sigma_\varepsilon} \right) \frac{\partial \varepsilon}{\partial x_j} \right] + C_{1\varepsilon} \frac{\varepsilon}{k} (P_k + P_b C_{3\varepsilon}) + S_\varepsilon - C_{2\varepsilon} \rho \frac{\varepsilon^2}{k} \quad (8)$$

where P_k, P_b are the turbulent kinetic energy productions due to mean velocity gradients and buoyance effects respectively given by,

$$P_k = -\bar{\rho} \widetilde{u_i' u_j'} \frac{\partial \tilde{u}_i}{\partial x_j}$$

$P_b = 2\mu_t S_{ij} S_{ij}$ and S_{ij} is the mean strain rate tensor given by

$$S_{ij} = \frac{1}{2} \left(\frac{\partial \tilde{u}_j}{\partial x_i} + \frac{\partial \tilde{u}_i}{\partial x_j} \right)$$

S_k, S_ε are possible extra source terms and Y_m is the compressible dilatation effect on the energy dissipation rate. $C_{1\varepsilon}, C_{2\varepsilon}, C_{3\varepsilon}$ in equation (8) are model constants determined empirically. σ_k & σ_ε are the turbulent Prandtl numbers.

The model constants used for this study are (Standard k-epsilon model, 2005) $C_{1\varepsilon} = 1.44, C_{2\varepsilon} = 1.92, C_{3\varepsilon} = -0.33, C_\mu = 0.09, \sigma_k = 1, \sigma_\varepsilon = 1.3$

2.2.2 Realizable k - ε model

Realizable k - ε model is a modified form of the Standard k - ε model which uses the same equation (7) for the turbulent kinetic energy term but uses different improved dissipation rate transport equation. Realizable k - ε model also uses variable C_μ value instead of constant value as used in the Standard k - ε model. This model is called realizable model since the normal stresses ($\widetilde{u_i'^2}$) don't tend to become negative when using variable C_μ value.

The improved transport equation for the turbulent energy dissipation rate ε is given by, (Realizable k-epsilon model, 2005)

$$\frac{\partial(\bar{\rho}\varepsilon)}{\partial t} + \frac{\partial(\bar{\rho}\tilde{u}_i \varepsilon)}{\partial x_i} = \frac{\partial}{\partial x_j} \left[\left(\mu + \frac{\mu_t}{\sigma_\varepsilon} \right) \frac{\partial \varepsilon}{\partial x_j} \right] + \bar{\rho} C_1 S \varepsilon + C_{1\varepsilon} \frac{\varepsilon}{k} (P_b C_{3\varepsilon}) + S_\varepsilon - \bar{\rho} C_2 \frac{\varepsilon^2}{k + \sqrt{(v\varepsilon)}} \quad (9)$$

where, $C_1 = \max \left[0.43, \frac{\eta}{\eta+5} \right]$

$$\eta = S \frac{k}{\varepsilon}$$

$$S = \sqrt{S_{ij} S_{ij}}$$

The terms $P_k, P_b, S_k, S_\varepsilon, \sigma_k$ & σ_ε are the same as in the Standard k - ε model. The main difference in this model is the use of variable C_μ value and turbulent kinetic energy production term is replaced by the term containing S in the epsilon equation

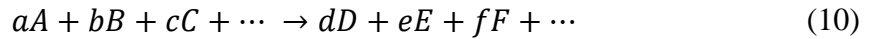
The model constants used for this study are, (Realizable k-epsilon model, 2005)

$$C_{1\varepsilon} = 1.44, C_2 = 1.9, C_{3\varepsilon} = -0.33, \sigma_k = 1.0, \sigma_\varepsilon = 1.2$$

2.3 Chemical Kinetics

Since spray combustion is accompanied by chemical reactions, the time scales of chemical reactions determine the structure of the flame. Hence chemical kinetics plays an important role in the modeling of spray combustion. The ethanol fuel after undergoing atomization and evaporation, react with oxidizer. During this combustion process, chemical reactions take place producing combustion products. The ethanol fuel combustion involves many species and many reactions. The chemical kinetics for each of these reactions has to be accounted for when modeling the turbulent spray combustion. The chemical reaction rates have to be solved for each of these reactions and it is accounted for in the chemical source term $\bar{\rho} \tilde{S}_k$ in equation (3)

Any chemical reaction is defined by a reaction equation,



In the equation (10), A, B and C are the reactants and D, E and F are the products. The stoichiometric coefficients of the reactants are given by a, b and c and those of the products are given by d, e , and f .

For a simple reaction like in (10), the rate of the reaction is found from the Rate Law,

$$\text{Rate of Reaction, } R = k[A]^m[B]^n[C]^o \quad (11)$$

$[A]$ represent the concentration of the reactant A and k represents the rate coefficient for that chemical reaction. ‘ m ’, ‘ n ’ and ‘ o ’ represent the exponents found empirically for the reaction. Since the rate constant k is a function of concentration and temperature, it is given by Arrhenius equation,

$$k = AT^n \exp \frac{-E_a}{RT} \quad (12)$$

where A is the pre-exponential factor, n is the temperature exponent, E_a is the activation energy for the chemical reaction, R is the gas constant. The gas constant is calculated empirically.

The rate of reaction for all the chemical reactions in which a species 'k' participates, together gives the source term used in equation (3). As mentioned before, the fuel considered is ethanol and in the literature, there are several chemical reaction mechanisms available for the combustion of ethanol including intermediary chemical species. There are many reduced chemical reaction mechanisms available since detailed reaction mechanisms require a lot of computational resources. There is a well-known detailed chemical reaction mechanism for ethanol oxidation formulated by Marinov which consists of 57 species and 383 reactions (M.Marinov, 1998) , but it was not considered for the simulations in this study since we have to take into the account of computational cost in the framework of the PaSR combustion model (see next section). The reaction mechanism analyzed in this numerical study is a one-step global reaction mechanism formulated by Dryer (K.Westbrook & L.Dryer, 1981) and detailed reaction mechanism (38 species and 228 reactions) by Roehl and Peters (Röhl & Peters, 2009) and a study of these reaction mechanisms are carried out.

2.4 Combustion Model

The mean chemical source term $\bar{\rho}\tilde{S}_k$ in conservation equation (3) is unknown and it requires a closure model to solve the term. The combustion model generally uses the turbulent time scale and chemical time scale to account for the reaction rate since the mixing rate determines the chemical kinetics in case of fast chemistry. The reaction rates are a function of local temperature and the variation of the reaction rate is given by Arrhenius rate law equation. Various combustion models are available to close the source terms associated with enthalpy and species mass fraction. In this study, the interaction between the turbulence and chemistry is modeled by means of a Partially Stirred Reactor Model (PaSR).

Partially Stirred Reactor Model

This PaSR model was formulated by Chalmers University of Technology (Golovitchev & Nordin, 2001). The PaSR model assumes that the flame structures are much smaller than the computational cell and that the entire cell is divided into a reacting zone and a non-reacting zone (Karrholm, 2008). In the non-reacting zone, only inert mixing occurs. PaSR model assumes that the reaction zone can be considered to be a perfectly stirred reactor. In the perfectly stirred reactor region, the chemical time scale is larger than the turbulent time scale.

According to this model, the following assumptions are made. The reacting zone is considered to be a perfectly stirred reactor (PSR) and the reactants in the zone are perfectly mixed with each other thereby neglecting any fluctuations (homogeneous mixing). Figure 2.1 explains how the reaction takes place inside the computational cell in a PaSR model.

At the start of the time 't₀', the concentration entering the cell is 'c₀' and it is the averaged initial concentration of the cell and this 'c₀' is a known quantity calculated from previous iterations.

Now if we consider the entire cell as a PSR, complete mixing of chemical species occurs and concentration of the cell changes from initial 'c₀' to reaction concentration 'c' (Reaction I in Figure 2.2). But only a portion of the cell is a PSR and the average concentration can only change from 'c₀' to average exit concentration 'c₁' in a time τ . The concentration 'c₁' is to be determined.

The time averaged reaction rate for the PaSR cell is given by,

$$\left(\frac{\partial c_k}{\partial t}\right)_{PaSR} = \frac{c_{1,k} - c_{0,k}}{\tau} \quad (13)$$

where, c_k is the average concentration of species 'k'.

The average reaction rate for the PSR cell is given by,

$$\left(\frac{\partial c_k}{\partial t}\right)_{PSR} = \frac{c_k - c_{0,k}}{\tau} \quad (14)$$

We can see that reaction rate of PSR is higher than that of PaSR.

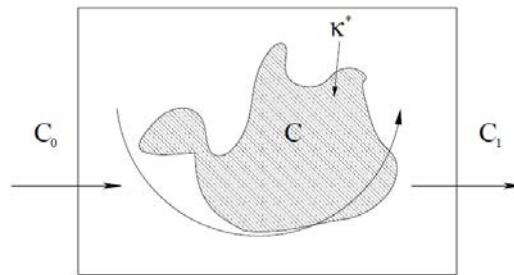


Figure 2.1 Partially Stirred Reactor Model Reaction Scheme (Karrholm, 2008)

Maintaining the same mean reaction rate, the PaSR cell takes an extra time τ' to reach this PSR concentration 'c' (Reaction II in Figure 2.2). The averaged reaction concentration 'c' can be found by,

$$c = c_0 + \left(\frac{\partial c_k}{\partial t}\right)_{PaSR} (\tau + \tau') \quad (15)$$

where τ' is the extra time taken by the PaSR cell to reach concentration 'c'.

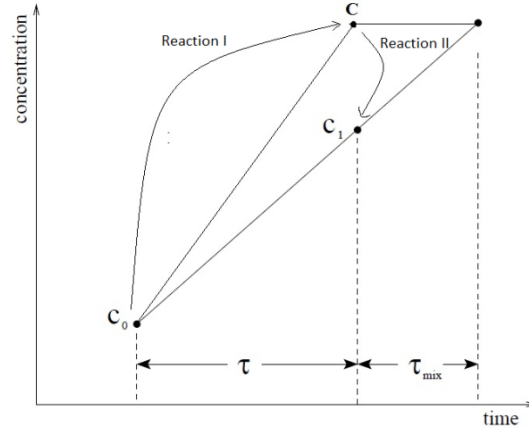


Figure 2.2 Reaction and mixing procedure

Substituting the value of equation (13) in (15), we can obtain for every species,

$$c_1 = \kappa^* c + (1 - \kappa^*)c_0 \quad (16)$$

$$\kappa^* = \frac{\tau}{(\tau + \tau')} \quad (17)$$

where κ^* is the volume fraction of PSR in the cell. An extra time of τ' is taken by a PaSR cell to reach the same averaged concentration 'c' as that of a PSR cell. This extra time is related to the mixing process for the mixing of species by turbulence in the reacting and non-reacting zone. Hence τ' can be called τ_{mix} and

$$\kappa^* = \frac{\tau}{(\tau + \tau_{mix})} \quad (18)$$

If the mixing of species is fast, $\tau_{mix} = 0$ and $\kappa^* = 1$. Hence the final concentration reached is 'c' from equation (16) and the cell behaves like a PSR. If the mixing of species is slow, $\tau_{mix} = \infty$ and $\kappa^* = 0$. Then there is no reaction in the cell as 'c₁'='c₀'

The mixing time scale τ_{mix} is obtained from the k - ϵ model,

$$\tau_{mix} = C_{mix} \frac{k}{\epsilon} \quad (19)$$

C_{mix} is a model constant determined empirically and its value is 0.03 (Golovitchev & Nordin, 2001)

The reaction rate at concentration 'c' for the PaSR for every species is given by,

$$\dot{f}(c)_{PaSR} = \frac{c_1 - c_0}{\tau} \quad (20)$$

$$\dot{f}(c)_{PaSR} = \frac{\kappa^* c + (1 - \kappa^*) c_0 - c_0}{\tau} = \kappa^* \left(\frac{c - c_0}{\tau} \right) \quad (21)$$

$$\dot{f}(c)_{PaSR} = \kappa^* \left(\frac{\partial c_k}{\partial t} \right)_{PSR} = \kappa^* \dot{f}(c)_{PSR} \quad (22)$$

$\dot{f}(c)_{PSR}$ is the reaction rate for the PSR cell evaluated at concentration 'c'. The reaction rate for the PSR cell at concentration 'c' is determined by Nordin as (Golovitchev & Nordin, 2001)

$$\dot{f}(c)_{PSR} = \kappa \dot{f}(c_1)_{PSR} \quad (23)$$

and κ is given by,

$$\kappa = \frac{\tau_c}{\tau_c + \tau_{mix}} \quad (24)$$

where, τ_c is the chemical time scale given by,

$$\frac{1}{\tau_c} = - \frac{\partial \dot{f}_{PaSR}}{\partial c_k}$$

Now based on the findings by Nordin (Golovitchev & Nordin, 2001), reaction rate for the PaSR cell at concentration 'c' can be found from equation (25)

$$\dot{f}(c)_{PaSR} = \kappa^* \kappa \dot{f}(c_1)_{PSR} \quad (25)$$

In the OpenFOAM's implementation of PaSR model, κ^* is taken as 1. Therefore,

$$\dot{f}(c)_{PaSR} = \kappa \dot{f}(c_1)_{PSR} \quad (26)$$

$\dot{f}(c_1)_{PSR}$ is calculated by reaction rate of chemical species equation for concentration 'c₁' using rate law equations (11) and (12) described in Section 2.3 The chemical change according to the reaction rate is solved numerically using a time-step depending on stability criteria.

2.5 Spray/Discrete Phase modeling

In spray combustion, the droplets are dispersed in continuous gas phase and it is described by means of Lagrangian method. The solver used in OpenFOAM considers a number of droplets as 'parcels' since tracking a large number of particles can increase the computational cost. A spray parcel can be a single droplet or a group of identical droplets having the same properties of representative droplets in a computational domain. These spray parcels represent

spray distribution function which is nothing but the probability of spray being composed in a particular way (Stiesch, 2013).

There are different phenomena that occur within the liquid phase in the spray combustion. These include atomization, dispersion, evaporation, micro-mixing and combustion (Jenny, Roekaerts, & Beishuizen, 2012). When the fuel is injected from the fuel injector into the gaseous phase, instabilities occur at the liquid-gas phase interface due to Kelvin Helmholtz instabilities which results in the formation of liquid sheet ligaments. This is the primary atomization. The interaction between the liquid phase and the gaseous phase creates turbulence and aerodynamic forces which act on the liquid droplets thereby disintegrating them into even smaller droplets, which is the secondary breakup.

The evaporation of liquid fuel from the droplet surface takes place when there is a concentration gradient or a temperature gradient between the hot gaseous atmosphere and ambient liquid droplet. The turbulent velocity fluctuations near the gas and the liquid phase creates turbulence which helps in increasing the mixing of the fuel vapor from droplet and the surrounding gas thereby enhancing the local evaporation rate. Once the combustion has started, the high temperature of the gaseous atmosphere and turbulence helps to sustain the combustion and chemical reaction.

The different models used in numerical modeling of the spray will be discussed in this subsection.

2.5.1 Droplet Motion

The motion of the Lagrangian droplet is calculated by means of its basic equation of motion,

$$\sum F = m_p \frac{du_{p,i}}{dt} \quad (27)$$

where m_p is the mass of the droplet particle and $u_{p,i}$ is the velocity of the droplet in direction 'i'. The different relevant forces are the drag force, F_D and the gravitational force, F_g .

$$\sum \vec{F} = \vec{F}_D + \vec{F}_g + \vec{F}_x \quad (28)$$

$$\vec{F}_D = m_p \frac{18\mu}{\rho_p d_p^2} \frac{C_D Re}{24} (\vec{u} - \vec{u}_p) \quad (29)$$

where, ρ_p is the density of the liquid, d_p is the diameter of the particle, u is the gas phase velocity, Re is the relative Reynolds number and C_D is the drag coefficient.

$$Re = \frac{\rho d_p |\vec{u}_p - \vec{u}|}{\mu} \quad (30)$$

where, ρ is the density of the gas and μ is the dynamic viscosity of the gas.

and the Drag coefficient for a spherical droplet is given by,

$$C_D = \begin{cases} \frac{24}{Re_p} (1 + 0.15Re_p^{0.687}), & \text{if } Re_p \leq 1000 \\ 0.44, & \text{if } Re > 1000 \end{cases} \quad (31)$$

The gravitational and buoyancy force is given by,

$$\vec{F}_g = m_p \vec{g} \left(\frac{\rho_p - \rho}{\rho_p} \right) \quad (32)$$

F_x is the force due to added mass and pressure gradient which are negligible in spray flames.

$$\vec{F}_x = \frac{m_p \pi d_p^3 \rho_p}{12} \frac{d(\vec{u} - \vec{u}_p)}{dt} + \frac{1}{6} \pi d_p^3 \vec{\nabla} P \quad (33)$$

where $\vec{\nabla} P$ is the pressure gradient.

Turbulent Dispersion Model

Turbulent dispersion of particles here is modeled by a Stochastic dispersion model using Discrete Random walk method. In this method, each particle injected into the domain is tracked by the model. The droplet particles get dispersed after injection due to turbulence in the flow field. The droplets take different trajectories due to the dispersion and droplet trajectories are important during evaporation process since the position of the droplets affect the temperature and chemical composition of the droplet and the surrounding gas (Merci, Roekaerts, & Sadiki, 2011). In Lagrangian droplet motion tracking, the instantaneous velocity of the fluid (gas phase) in equation (29) is unknown and stochastic tracking method is used to calculate this instantaneous fluid velocity, thereby tracking the trajectory of the droplets.

The instantaneous gas phase velocity is found as a sum of the fluctuation and mean velocity field.

$$u_i = \tilde{u}_i + u'_i(t) \quad (34)$$

The velocity fluctuation u'_i is found by means of Root Mean Square (RMS) of the velocity fluctuation and a Gaussian probability distribution assumed isotropic in the three directions.

The model used in sprayFoam named Discrete Random walk model (eddy lifetime model), simulates the interaction of the droplets with the turbulent eddies of the gas phase (Rochaya, 2007)

$$u' = \zeta \sqrt{\frac{2k}{3}} \quad (35)$$

where, ζ is a normally distributed random number and k is the turbulent kinetic energy. For each of the velocity component, a random number has to be sampled. The amount of fluctuation is determined by the amount of turbulence in the flow field as described by equation (35). For the k - ε model, isotropy is assumed for the RMS velocity fluctuations and the RMS velocity fluctuation can be found from the turbulent kinetic energy.

$$\sqrt{\overline{u'^2}} = \sqrt{\overline{v'^2}} = \sqrt{\overline{w'^2}} = \sqrt{\frac{2k}{3}} \quad (36)$$

The lifetime of the turbulent eddy for the k - ε model is found by means of

$$\tau_e = 0.3 \frac{k}{\varepsilon} \quad (37)$$

After a lifetime of the eddy, a new value of u' is sampled.

2.5.2 Injection Model

The injector used in the experimental study of the spray combustion is a cone nozzle injector. In the numerical study, injector model which can simulate the working of the real cone nozzle injector should be selected. As mentioned earlier, the liquid fuel is injected by the injector into the gaseous atmosphere and primary atomization and secondary breakup occurs leading to the formation of droplets as explained in the start of the discrete phase model. The process of atomization can be divided into primary atomization and secondary atomization.

There are three different regimes identified with the spray structure. They are dense, dilute and very dilute regime (Jenny, Roekaerts, & Beishuizen, 2012). The atomization process takes place in the dense regime in which the dispersed phase volume fraction is above 10^{-3} . In this regime, liquid sheet breakup and droplet collision occurs. In the dilute regime, dispersed phase volume fraction is around 10^{-6} and 10^{-3} . The interaction between the droplet phase and the gaseous phase is of higher importance in the region. In the very dilute regime, dispersed phase volume fraction is less than 10^{-6} and the two phase interaction is less significant.

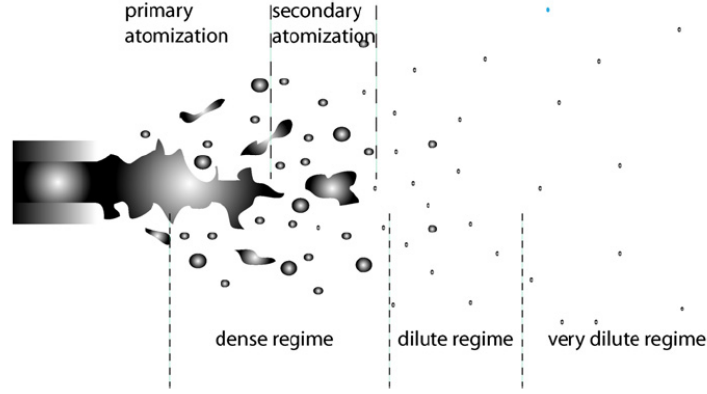


Figure 2.3 Different flow regimes during spray injection process (Jenny, Roekaerts, & Beishuizen, 2012)

In a fuel injection process, first film formation occurs, and then sheet breakup and atomization occurs. The injector model used in the numerical simulations is the default Cone Nozzle injector available in OpenFOAM. The flow type used for the study is the pressure driven velocity in which the initial velocity of the injected droplets are calculated from the injection pressure specified for the injector.

The magnitude of the injection velocity is calculated from,

$$U = \sqrt{\frac{2(P_{inj} - P_{amb})}{\rho_p}} \quad (38)$$

where, U is the velocity of the injected fuel, P_{inj} is the injector pressure, P_{amb} is the ambient pressure and ρ_p is the density of the injected fuel.

The direction of the injection depends on the spray angle (cone angle) and the dispersion angle. The injector model uses Rosin-Rammler size distribution to specify the range of droplet diameters. The droplet size distributions are made based on the minimum and maximum diameter of the droplets and are divided into a number of intervals with each interval specified by a mean diameter. This can be used to calculate the mass fraction of the droplet in a particular size interval.

$$Y_d = \exp\left(-\left(\frac{d}{\bar{d}}\right)^n\right) \quad (39)$$

where ‘ n ’ is the spread parameter of the droplets and Y_d is the mass fraction of the droplet in a particular size interval and \bar{d} is the mean diameter of the droplets which has to be specified in the model.

The model constants used in the simulations are $d_{min} = 1 \times 10^{-6}$ m, $d_{max} = 8 \times 10^{-5}$ m, $\bar{d} = 0.00015$ m, $n = 3$ and dispersion angle = 15°

Atomization model

For the hot-coflow case, the experiments done by Hugo (Correia Rodrigues H. , Tummers, Roekaerts, & van Veen, 2015) show that when the fuel is injected from the injector orifice, the liquid starts breaking immediately in small fragments due to evaporation of the droplets and the further breakup takes place by the secondary breakup. Hence for the hot-coflow case in the numerical study, no primary atomization is considered.

Breakup Model

The liquid breakup model is modeled by means of the Reitz and Diwakar model in sprayFoam. The breakup of the liquid ligaments is defined by means of the Weber number,

$$We = \frac{\rho_g |u_p - u_g|^2 d_p}{\sigma} \quad (40)$$

where ρ_g is the density of the gas, u_p is the droplet velocity, u_g is the gas velocity, d_p is the diameter of the droplet and σ is the surface tension.

The droplet radius after undergoing breakup is calculated by means of

$$\frac{dr_p}{dt} = \frac{-(r_p - r_{stable})}{t_{br}} \quad (41)$$

where, r_p is the radius of the droplet before breakup, r_{stable} is the stable radius of the droplet after breakup and t_{br} is the breakup time.

In a Reitz and Diwakar model, there are two breakup regimes depending on the Weber number. They are bag breakup and stripping breakup.

Bag breakup occurs when Weber number is greater than critical Weber number of 6.

$$t_{br} = C_1 \sqrt{\frac{\rho_p r_p^3}{2\sigma}} \quad (42)$$

$$r_{stable} = \frac{6\sigma}{\rho_g |u_p - u_g|^2} \quad (43)$$

where, ρ_g is the density of the gas, ρ_p is the density of the droplet and $C_1 = 0.785$

Stripping breakup occurs when Weber number is between 80 and 350.

$$t_{br} = C_2 \frac{r_p}{|u_p - u_g|^2} \sqrt{\frac{\rho_p}{\rho_g}} \quad (44)$$

$$r_{stable} = \frac{\sigma^2}{2\rho_g^2 |u_p - u_g|^3 \nu} \quad (45)$$

where, ν is the kinematic viscosity of the gas and $C_2 = 10$

2.5.3 Evaporation model

The droplet evaporation is an important phenomenon in the modeling of spray combustion since heat, mass and momentum transfer takes place between the droplet interface and the gaseous phase. In a single droplet, the droplet surface starts heating up due to heat transfer from the hot gaseous surroundings. As a result, heat transfer to the inner core of the droplet by means of conduction from the droplet surface until equilibrium is achieved. The gaseous fuel formed during evaporation diffuses into the gaseous environment.

The evaporation models considered in this study are Gradient diffusion model and Spalding evaporation model. These evaporation models are based on the infinite liquid- conductivity model in which the droplet surface temperature is equal to the inside temperature of the droplet and it is a function of time.

Gradient diffusion controlled model

According to this model, the evaporation takes place due to gradient diffusion as result of vapor concentration gradient between the droplet surface and the surrounding gas. The molar flux of the vapor is given by,

$$N_i = k_c (C_{i,s} - C_{i,\infty}) \quad (46)$$

where, N_i is the molar flux of the vapor, k_c is the mass transfer coefficient, $C_{i,s}$ is the concentration of the vapor at droplet surface and $C_{i,\infty}$ is the concentration of the vapor in the bulk gas.

$$C_{i,s} = \frac{p_{sat}(T_p)}{RT_p} \quad (47)$$

where, p_{sat} is the saturation vapor pressure, R is the universal gas constant and T_p is the temperature of the droplet.

$$C_{i,\infty} = X_i \frac{p_c}{RT_\infty} \quad (48)$$

where, p_c is the carrier gas phase pressure, R is the universal gas constant, X_i is the local bulk molar fraction of species 'i' and T_∞ is the local temperature of the gas phase.

$$k_c = \frac{Sh \times D_{i,m}}{d_p} \quad (49)$$

where, Sh is the Sherwood number, $D_{i,m}$ is the diffusion coefficient of the vapor in the bulk and d_p is the diameter of the droplet particle.

The Sherwood number is given by the Ranz-Marshall correlation for mass transfer.

$$Sh = 2 + 0.6\sqrt{Re}(Sc)^{1/3} \quad (50)$$

where the Schmidt number, Sc is given by,

$$Sc = \frac{\nu}{D_{i,m}} \quad (51)$$

where ν is the kinematic viscosity.

The time evolution of the mass of the droplet is given by (rate of evaporation),

$$\frac{dm_p}{dt} = -N_i 4\pi r_p^2 M_{w,i} \quad (52)$$

where, m_p is the mass of the droplet, $M_{w,i}$ is the molecular weight of the species 'i'.

Spalding evaporation model

This evaporation model was formulated by Spalding (Spalding, 1953). The rate of evaporation for the model is given by,

$$\frac{dm_p}{dt} = -k_c 4\pi r_p^2 \rho_\infty \ln(1 + B_m) \quad (53)$$

where, ρ_∞ is the density of the bulk gas, r_p is the radius of the particle, B_m is the Spalding Mass number given by,

$$B_m = \frac{(X_{i,s} - X_{i,\infty})}{(1 - X_{i,s})} \quad (54)$$

where, $X_{i,s}$ is the vapor mass fraction at the droplet surface and $X_{i,\infty}$ is the vapor mass fraction of the bulk gas.

The main difference between the two evaporation models is how the Spalding mass number is treated and the inclusion of Stefan flow (S.Sazhin, 2006) in the derivation of Spalding evaporation rate. In the limit of small B_m , $\ln(1 + B_m) \approx B_m$ and the Spalding model reduces to the gradient diffusion model. Also, gradient diffusion model was originally developed for mass diffusion through porous wall (Miller, Harstad, & Bellan, 1998) and not for two-phase flows.

The vapor mass fraction at the droplet surface is deduced by means of Raoult's law,

$$X_{i,s} = \frac{p_{sat}}{p_c} \quad (55)$$

where, p_{sat} is the saturation vapor pressure and p_c is the carrier gas phase pressure.

The properties of the gas phase film is evaluated by means of the '1/3' rule.

$$T_f = T_p + \frac{1}{3}(T_\infty - T_p) \quad (56)$$

$$X_f = X_p + \frac{1}{3}(X_\infty - X_p) \quad (57)$$

where, T_f is the film-average temperature, T_∞ is the temperature of the bulk gas and T_p is the temperature of the droplet particle. X_f is the film-average mass fraction. The T_f and X_f from the '1/3' rule is used to calculate the thermal conductivity and specific heat capacity in equation (60).

The droplet temperature for both the models is calculated using heat balance equation which uses sensible heat change in the droplet due to convection and latent heat transfer between the droplet and the gaseous phase (radiation is negligible as shown by previous study by Seyed (Jamali, 2014)),

$$m_p c_p \frac{dT_p}{dt} = h A_p (T_\infty - T_p) f_{heat} - \frac{dm_p}{dt} h_{fg} \quad (58)$$

where, c_p is the specific heat of the liquid, h is the convective heat transfer coefficient obtained from the Ranz-Marshall correlation for the Nusselt number given by equation (59), h_{fg} is the latent heat of vaporization.

$$Nu = \frac{h d_p}{k_\infty} = (2 + 0.6\sqrt{Re}(Pr)^{1/3}) \quad (59)$$

where, k_∞ is the thermal conductivity of the bulk gas phase and the correction factor f_{heat} on the heat transfer is given by,

$$f_{heat} = \left[\frac{\frac{-c_{p,v}\dot{m}_p}{\pi l_c k_\infty Nu}}{\left(e^{\frac{-c_{p,v}\dot{m}_p}{\pi l_c k_\infty Nu}} - 1 \right)} \right] \quad (60)$$

where $c_{p,v}$ is the specific heat capacity of the bulk gas, \dot{m}_p is the rate of evaporation, Nu is the Nusselt number given by equation (59).

Chapter 3

OpenFOAM

The Master thesis work is done with the aid of OpenFOAM code which is an open source CFD software package. Chapter 2 explained the various models and equations involved in solving turbulent spray combustion. In this chapter, we explain the capabilities of the CFD software used to simulate the spray combustion. OpenFOAM stands for Open Field Operation and Manipulation which is based on object-oriented programming written in C++ language (OpenCFD). The main advantage of using OpenFOAM is that users are able to modify the code for their custom applications. Also the software's ability to run the code in parallel enables the use of multiple processors on the computer system. It effectively improves the processing speed of the CFD package. OpenFOAM has an in-built solver for solving combustion problems in sprayFoam. The version of OpenFOAM used for the numerical study is OpenFOAM-2.3.x.

3.1 sprayFoam

Turbulent spray combustion is a complex process and it is solved by means of sprayFoam in OpenFOAM. sprayFoam is a transient solver for compressible, turbulent flow with spray parcels (OpenCFD). Since the experiments conducted on DSHC burner is based on spray injection, sprayFoam can be used to solve the spray combustion process. sprayFoam solver uses Eulerian-Lagrangian approach and the interaction between the continuous phase and discrete phase is given by two-way coupling. In a two-way coupling, gaseous phase influences the droplet phase by means of drag and turbulence and the droplet phase influence the gaseous phase by means of source terms of mass, momentum and energy equations. The trajectory of the droplets is calculated by means of Discrete Random Walk (DRW) model (Rochaya, 2007).

sprayFoam is based on Cloud (collection of Lagrangian particles) class basicSprayCloud. The sprayFoam solver has three main directories 'basic, lagrangian and spray' in src/lagrangian folder. These directories contain different type of particles which are used in the submodels. The different submodels used in sprayFoam which are of importance are

1. Atomization model
2. Breakup model
3. Dispersion model
4. Phase change model

These submodels are inherited from template class 'Cloud Type'. These models are explained in model equations of Chapter 2. A customized sprayFoam solver is created for the thesis work according to tutorials by Per Carlsson (Carlsson, 2009). The main structure of sprayFoam solver directory consists of 0, system, constant, chemkin folders.

The '0' folder consists of the initial and boundary conditions for the droplet and the gaseous phase. The 'constant' folder consists of various properties of the spray and different models used for the dilute spray combustion. The properties and models for the spray cloud are specified in the sprayCloudProperties file. In the sprayCloudProperties file, the injector properties, fuel properties, submodel coefficients are specified which are used as input conditions for the spray (refer Appendix A.3).

The 'chemkin' folder consists of chemical input file in the Chemkin-II format for the fuel used in the simulation. The input file can be of global reaction mechanism (K.Westbrook & L.Dryer, 1981), detailed reaction mechanism (M.Marinov, 1998) or reduced reaction mechanism for the ethanol (Röhl & Peters, 2009). These include chemical reactions with different constants for the Arrhenius rate law equation. This rate law is explained in detail in Section 2.3.

The 'chemkin' folder also contains thermodynamic data file which contains the polynomial coefficients for the molecules used in the reactions (GRI-Mech Version 3.0 Thermodynamics released 7/30/99). These polynomial coefficients (NASA) in the data file are used to calculate specific heat c_p , enthalpy H and entropy S (Carlsson, 2009).

The 'system' folder consists of time control functions in the controlDict file which is used to control the timesteps, write interval, etc. This folder also contains the finite volume matrix (FVM) and finite volume calculus (FVC) discretization schemes used to solve the various parameters in the conservation equations of the two phase flow. The FVM is an implicit method and FVC is an explicit method. It also contains a dictionary file to decompose the case so that the case can be run in parallel computing to save computational time.

The different numerical and discretization schemes used in sprayFoam are (Greenshields, 2015)

1. Interpolation scheme
2. Gradient scheme
3. Divergence scheme
4. Laplacian scheme
5. Surface Normal Gradient scheme
6. Time scheme
7. Flux scheme

3.1.1 Numerical Schemes

Interpolation scheme

OpenFOAM uses interpolationSchemes sub-dictionary to interpolate values from the center of the cell to center of the face. sprayFoam uses first-order linear interpolation to interpolate the values between cell center and face center.

Gradient scheme

The gradSchemes sub-dictionary used in OpenFOAM is used to solve the gradient derivative terms like ∇u . The scheme used in sprayFoam to solve gradient terms in the conservation equation is Gaussian second-order integration with interpolation done linearly. The numerical scheme uses FVC method for discretization scheme.

Divergence scheme

The divSchemes sub-dictionary used in OpenFOAM is used to solve the divergent/convective terms like $\nabla \cdot (\rho u_i u_j)$. The different divergent terms used in turbulent combustion conservation equations solved by sprayFoam are

Divergent terms $\nabla \cdot (\rho U x)$ – where x can be velocity (U), pressure (p), turbulent kinetic energy (k), eddy dissipation rate (ϵ), mass fraction (Y) is solved by means of Gaussian second-order integration with upwind differencing for the convective terms.

Divergent terms $\nabla \cdot (\rho U y)$ – where y can be total kinetic energy (K), viscosity (μ) with deviatoric second order stress tensor terms and $\nabla \cdot (U)$ terms are solved by means of Gaussian second-order integration with linear interpolation method.

Laplacian scheme

The laplacianSchemes sub-dictionary used in OpenFOAM is used to solve the laplacian terms in conservation equations like ∇^2 term. sprayFoam uses Gaussian second-order integration with linear interpolation method and surface normal gradient scheme to solve the terms in the equation (Greenshields, 2015).

Surface Normal Gradient Scheme

The snGradSchemes sub-dictionary used in OpenFOAM is used to solve the gradient terms in which the normal components (normal to the face of the grid) of the values in the center of the cell are calculated. sprayFoam uses default orthogonal scheme which calculates these normal values.

Time Scheme

The ddtSchemes sub-dictionary used in OpenFOAM is used to solve the $\frac{\partial}{\partial t}$ terms in the conservation equations. sprayFoam uses first-order Euler implicit method (backward Euler method) to calculate the time derivative term. Euler method is the most widely used first order method in OpenFOAM to solve the ordinary differential equations.

Flux scheme

The fluxRequired sub-dictionary used in OpenFOAM is used to solve the flux obtained during solving of the pressure terms in the conservation equations.

3.2 Solutions convergence check for H_{II} flame simulation

The convergence of solutions is an important part when doing numerical simulations. The solutions are found in a simulation by means of iteration and the check for convergence of solutions must be done. For steady state simulations, convergence of solution can be checked by means of residual plots. Residual is the absolute error in the solution after the iterative procedure by the solver. Residual plots give an overview of whether the solution has converged based on the value of residuals and the tolerance used for the variables in solver. For unsteady simulations, the solutions are transient in nature and residual plot is not an indicator of solutions convergence. The turbulent spray combustion simulated in this thesis study is of unsteady in nature and hence, in order to check for the solution convergence, the simulation solution values are plotted as a function of simulation time. From these plots, we will be able to see if the values initially change as a function of time and in time reaches steady state (solution convergence for unsteady simulations).

For an unsteady simulation, time-step size is an important parameter. The set time-step for the simulation determines whether the solver is able to capture all the transient behavior of the value of interest. The next important parameter is the Courant Number. Courant number is calculated based on the cell size, velocity of the flow in cell and time-step size used. In sprayFoam solver, we use adjustable time-step and a maximum Courant number is set. Due to this, the solver calculates the time-step based on iterative solution of Courant number. The value of Courant number is set between 0 and 1 for stability of results. The values used for the simulation are,

Timestep size = 2.5×10^{-06} (Modifiable timestep where the solver modifies the timesteps based on Courant number calculations)

Max Courant number = 0.5

The solver is based on PIMPLE algorithm, which is a merged algorithm of Semi-Implicit method for Pressure Linked Equations (SIMPLE) and Pressure Implicit with Splitting of Operator (PISO). PIMPLE algorithm includes relaxation factors to take advantage of the SIMPLE algorithm's feature. The relaxation factor is used to stabilize the simulation so that new updated values in iterations do not exceed the limit set. PIMPLE algorithm solves for the momentum equation once and calculates the pressure two times (based on pressure corrector set) in a time-step. Then the algorithm applies the relaxation factor for the pressure field. Based on the pressure field calculated, velocity field is updated and the momentum equation is solved again. This pressure-momentum iterative process goes on until the solution is converged. This pressure correction is done once in a time-step in PISO algorithm (If the pressure corrector is set more than once, then the solver operates in PIMPLE mode).

The solution convergence for the unsteady simulation of H_{II} flame is checked by means of convergence plots given in Figure 3.1, Figure 3.2 and Figure 3.3. The plots have desired quantity on Y-axis varying as a function of time (X-axis). These desired quantities are plotted

by means of average of the quantity at each time-step and tracking the quantity during the entire simulation time.

When we look at Figure 3.1, which gives the convergence plot for the gas phase temperature, we can observe that during the initial start of the simulation, at all elevations, the gas phase temperature reach a peak temperature lower than the peak flame temperature. This initial rise of gas phase temperature is due to the use of initial condition set for the inside of the computational domain. The initial internal field set for the domain is the hot coflow temperature. So as the fuel is injected into the computational domain, combustion starts immediately which results in sudden rise in temperature which happens up to a simulation time of 0.02s. Also we can find that, at higher elevations, it takes much longer simulation time to reach the peak temperature as the injected fuel hasn't reached those elevations. After the initial increase, the solution starts converging and we can see that from the steady state reached after 0.035s.

Similar behavior is found in Figure 3.2 which gives the convergence plot for the ethanol mass fraction. During initial time-steps, there is sudden increase of the mass fraction due to initial condition specified for the internal field. The solution converges for the same simulation time of 0.035s. The same trend is followed in the pressure convergence plot (Figure 3.3) where, atmospheric pressure of 1 bar is reached after the simulation has attained steady state. The initial pressure fluctuation is due to sudden temperature increase by combustion. These three plots show the convergence of the solutions for the H_{II} flame.

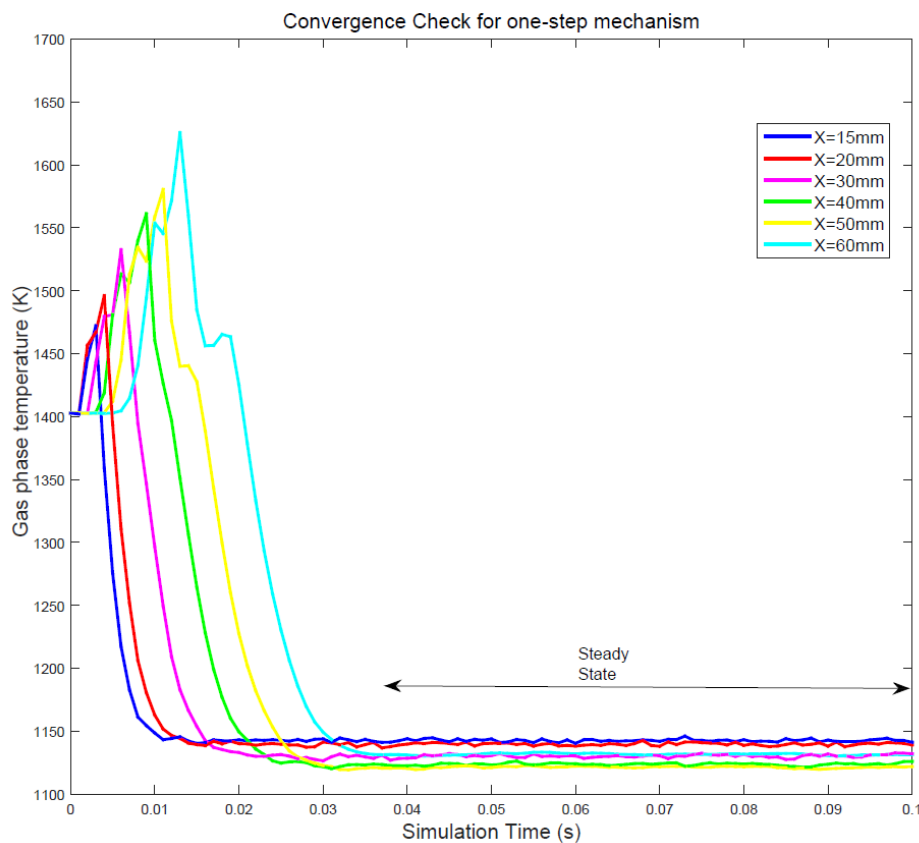


Figure 3.1 Convergence check for one-step mechanism using gas phase temperature

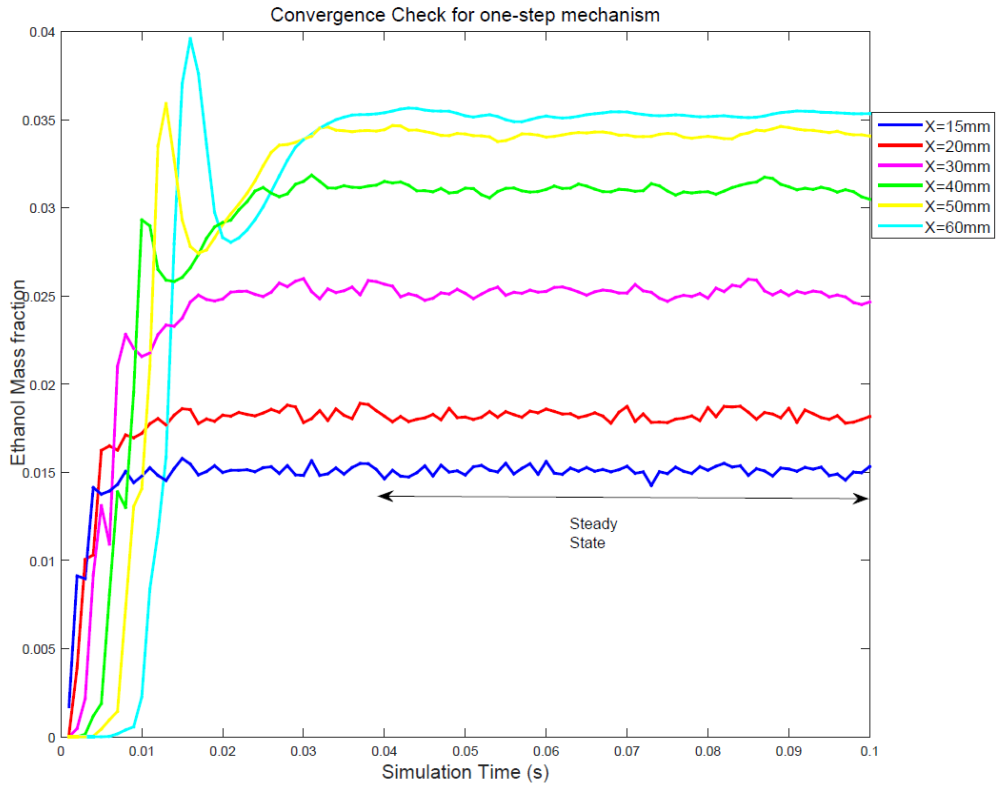


Figure 3.2 Convergence check for one-step mechanism using ethanol mass fraction

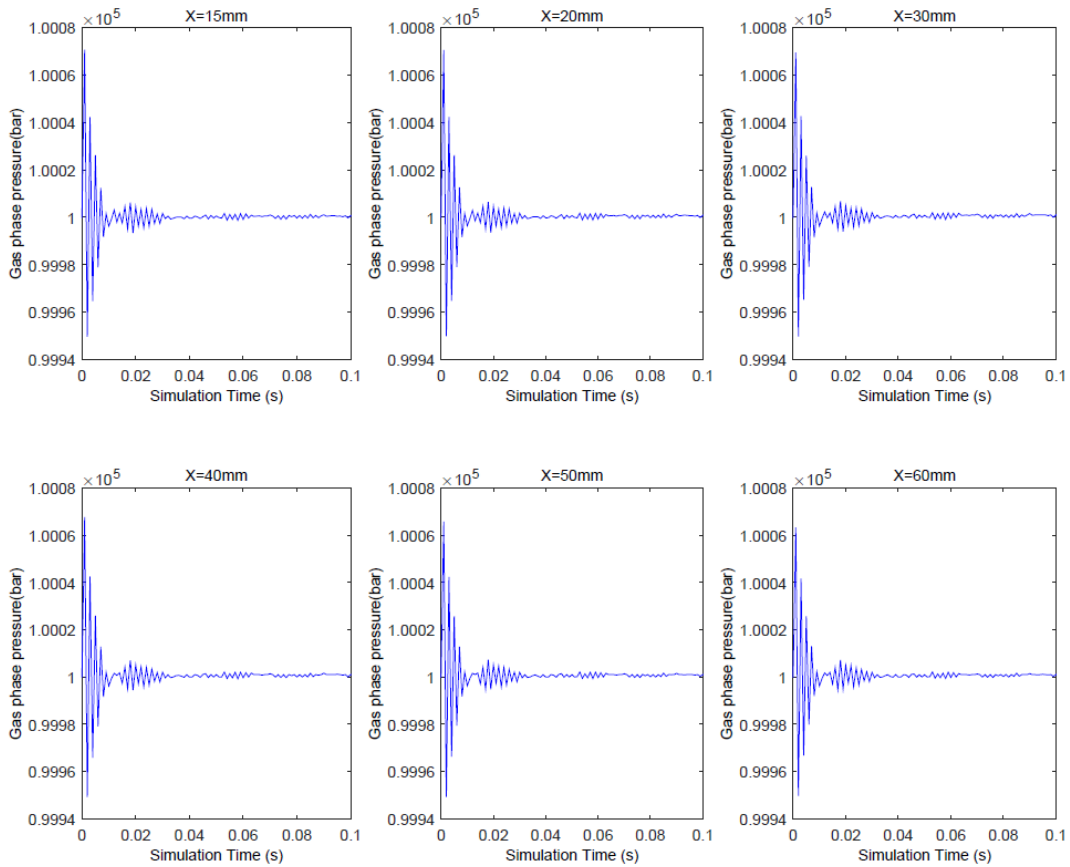


Figure 3.3 Convergence check for one-step mechanism using pressure in the flow

3.3 Postprocessing

The three-dimensional mesh for the study case (turbulent ethanol spray combustion) is meshed with the help of Ansys ICEM CFD and the mesh is converted into OpenFOAM format using fluent3DMeshToFoam conversion tool in OpenFOAM. The mesh quality is checked by means of checkMesh utility in OpenFOAM.

The post-processing of OpenFOAM results are visualized by visualization application ParaView. ParaView can be used to visualize both Eulerian and Lagrangian data. OpenFOAM uses foamtoVTK utility to convert Lagrangian results from sprayFoam into Visualizable Toolkit format which can then be viewed in ParaView.

The various plots like gas phase temperature, velocity components, droplet velocity components and Sauter Mean Diameter (SMD) of the droplets are obtained by means of sampling utility in OpenFOAM which serves as an input for Matlab and the plots are created by Matlab. In order to sample these data, sample dictionary file is created which contains different axial location section coordinates to be compared with experimental data. The data is sampled for all the time steps and then it is time averaged in Matlab using import function and plots are generated to compare it with the experimental data.

Chapter 4

Results and Discussion

In this chapter, the numerical simulations of turbulent spray combustion are carried out using sprayFoam solver for the hot-diluted coflow case and the numerical results are compared with the experimental data available for validation. In this chapter, the various parameters and models used to optimize the sprayFoam solver for the spray combustion are explained in detail and model comparison for spray flames with different coflow conditions represented as H_I, H_{II} and H_{III} cases in the DSHC dataset is done and is documented here.

Mesh configuration

A three dimensional axis-symmetric mesh was modeled using ICEM CFD with dimensions based on the experimental setup (Figure 4.1). The length of the mesh domain in the axial direction 'x' is 250 mm and it has a diameter of 200 mm. The injection point is present at the axis of the domain at coordinates (0, 0) so that the injector injects the ethanol in a conical configuration into the gaseous surroundings. The hot-dilute coflow from the secondary burner of DSHC burner and the ambient air surrounding the hot coflow is represented by boundary condition 'velocity inlet' since these are the two inlets of the domain. The injector wall is specified as wall boundary conditions (no-slip boundary condition) with wall functions specified. The outer surface of the burner is specified as 'symmetry' boundary condition as the normal velocity components are zero and all the other gradients are zero. The top of the burner is given outflow boundary condition (fully developed flow at the outflow) where exit pressure conditions are specified.

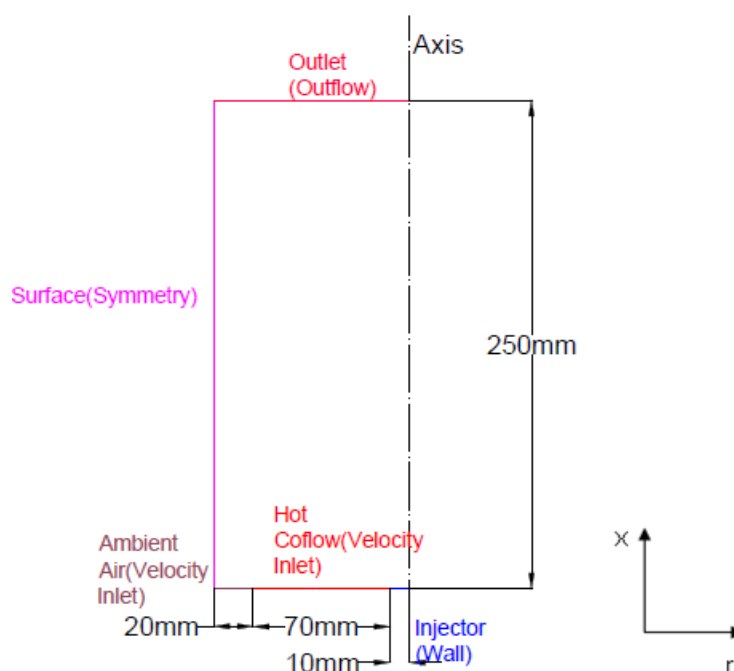


Figure 4.1 DSHC Burner mesh configuration and boundary conditions

The boundary conditions for the k and ε are calculated based on the following correlations (H.K.Versteeg & W.Malalasekera, 2007).

$$k = \frac{1}{2} \left(\overline{u'^2} + \overline{v'^2} + \overline{w'^2} \right) \quad (61)$$

where k is the turbulent kinetic energy. In equation (64), velocity terms ‘ u ’ and ‘ v ’ are calculated from experimental data and ‘ w ’ term is assumed equal to ‘ v ’ term.

$$\varepsilon = C_{\mu}^{3/4} \frac{k^{3/2}}{0.07l_c} \quad (62)$$

where, $C_{\mu} = 0.09$, l_c is the characteristic length of the flow. Here, it is the diameter of the coflow = 0.07m

The numerical simulations are first carried for the hot-diluted coflow case named ‘H_{II}’. The sprayFoam solver is optimized for the case H_{II} and then it is extended to cases H_I and H_{III} flames. The boundary conditions specified for the three cases are,

Table 4.1 Experimental boundary conditions for the spray and coflow

Case	Representative Temperature of the coflow (K)	Representative Coflow bulk velocity (m/s)	Oxygen volume fraction of the coflow (%)	Temperature of the injected fuel-ethanol (K)	Mass flow rate of the injected fuel (kg/s)	Injection pressure of the fuel (bar)
H _I	1600	3.5	6.8	300	3.8 X 10 ⁻⁴	12
H _{II}	1400	2.5	8.7	300	4.05 X 10 ⁻⁴	11.5
H _{III}	1300	1.9	9.5	300	4.11 X 10 ⁻⁴	11.7

The injector initial conditions specified for the injector model are

Nozzle orifice diameter = 2.1×10^{-4} m

Dispersion angle of the spray = $\text{Theta Outer} - \text{Theta Inner} = (45^\circ - 30^\circ) = 15^\circ$

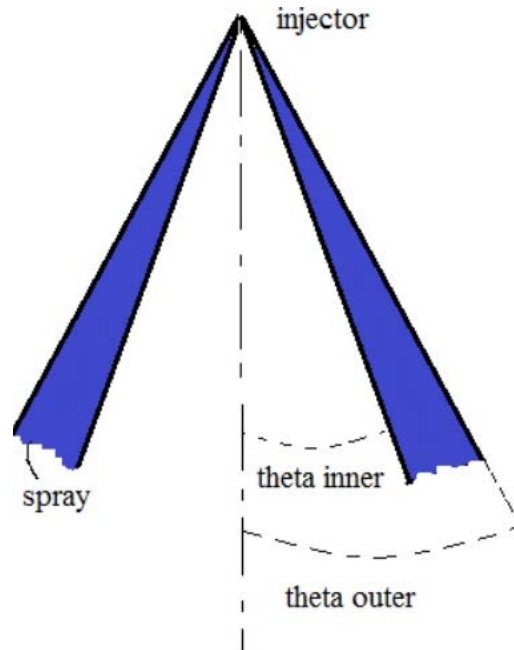


Figure 4.2 Spray angle configuration for a Cone nozzle injector (Forums)

The temperature of the hot-diluted coflow used for the simulation is a representative temperature based on the temperature profile measured by Hugo (Correia Rodrigues H. , Tummers, Roekaerts, & van Veen, 2015). The axial velocity of the coflow for the simulation is also a representative one. The input boundary conditions for the turbulent kinetic energy and eddy dissipation rate are calculated based on the $k-\varepsilon$ model formulations. The nozzle orifice diameter set for simulation is based on the experimental setup value and the dispersion angle of the spray is set based on the results of simulations by Jamali (Jamali, 2014) and trial and error method.

In the coming sections, we first describe the injector pressure optimization for the sprayFoam solver by studying the axial and radial velocity profiles and Sauter Mean Diameter (SMD) of the droplet. Then the model comparison for the spray combustion like turbulence model, atomization model and chemical kinetics (refer Appendix A.1) model is studied. Finally this study is extended to the spray flames of H_I and H_{III} case with the optimized model configuration.

4.1 Injector pressure optimization

The pressure at which the ethanol is injected into the gaseous atmosphere plays an important role in the distribution of droplets thereby affecting the evaporation rate of droplets. Since the velocity and size distribution of the droplet is calculated based on the injector pressure of the fuel, injector pressure optimization study is carried out in these numerical simulations.

The various parameters analyzed to arrive at the optimized injector pressure are axial, radial droplet velocity profiles and Sauter Mean Diameter (SMD) of the droplets.

The radial profiles of the mean droplet axial and radial velocity are analyzed from an elevation of 8mm to 40mm (at different axial locations). The droplet velocities calculated for a range of droplet diameter size groups of 10 μ m to 60 μ m. The Sauter Mean Diameter (SMD) is calculated for a range of elevations mentioned above. “The Sauter Mean Diameter (d_{32}) is diameter of a droplet particle which has the same volume to surface area ratio of the entire representative fuel spray” (Rochaya, 2007)

$$SMD, d[3,2] = \frac{\sum_i n_i d_{p,i}^3}{\sum_i n_i d_{p,i}^2} \quad (63)$$

where, n_i is the number of droplets in the corresponding representative i^{th} parcel and $d_{p,i}$ is diameter of the droplet in that representative i^{th} parcel.

Based on these parameters, various injection pressures of 4 bar, 6 bar and 10 bar are analyzed to arrive at the optimized one. These pressures are selected based on a trial and error method conducted. The pressure optimization study is undertaken with evaporation modeled by gradient diffusion model, turbulence modeled by standard $k-\varepsilon$ model and combustion modeled by PaSR model. The reaction mechanism for ethanol oxidation used is the global one-step mechanism formulated by Dryer (K. Westbrook & L. Dryer, 1981).

Injector pressure of 4 bar

Numerical simulations are conducted for the H_{II} flame case using an injection pressure of 4 bar. The mean droplet axial, radial velocity profile for various droplet size classes and SMD are plotted at various elevations (range of axial locations) against the radial distance from the center of the injector. The red lines in the plot denote the simulation results and black circles denote the experimental data measured. A comparison of these two data is done for the droplet velocity and diameter profiles.

From Figure 4.3 and Figure 4.4 which give the mean droplet axial velocity at different axial locations, we can see that only the smaller size droplets (10-20 μ m diameter) agree with the experimental data up to an elevation of 30mm and there are no droplets from the elevation of 40mm. This shows that the droplets have not reached the higher elevations due to insufficient injection pressure thereby reducing the mass flow rate and the velocity of the droplets for all the droplet size ranges. Also we can infer that there are no large droplets of size 50-60 μ m at all axial locations. This is due to Rosin-Rammler size distribution not predicting accurately at lower injection pressure. Thus, simulation mean axial velocity under-prediction shows that the injection pressure is not sufficient enough to create droplet velocity of required profiles. The same trend follows for the radial velocity profiles in Figure 4.5 and Figure 4.6. The SMD profiles of the droplets at 4 bar injection pressure are shown in Figure 4.7. The diameter profiles show that the droplet diameters are under-predicted at all elevations and the spread of the droplets over the radial position is also not captured well at this lower injection pressure.

Also there are no droplets from the elevation of 40mm downstream as shown in the droplet velocity profiles.

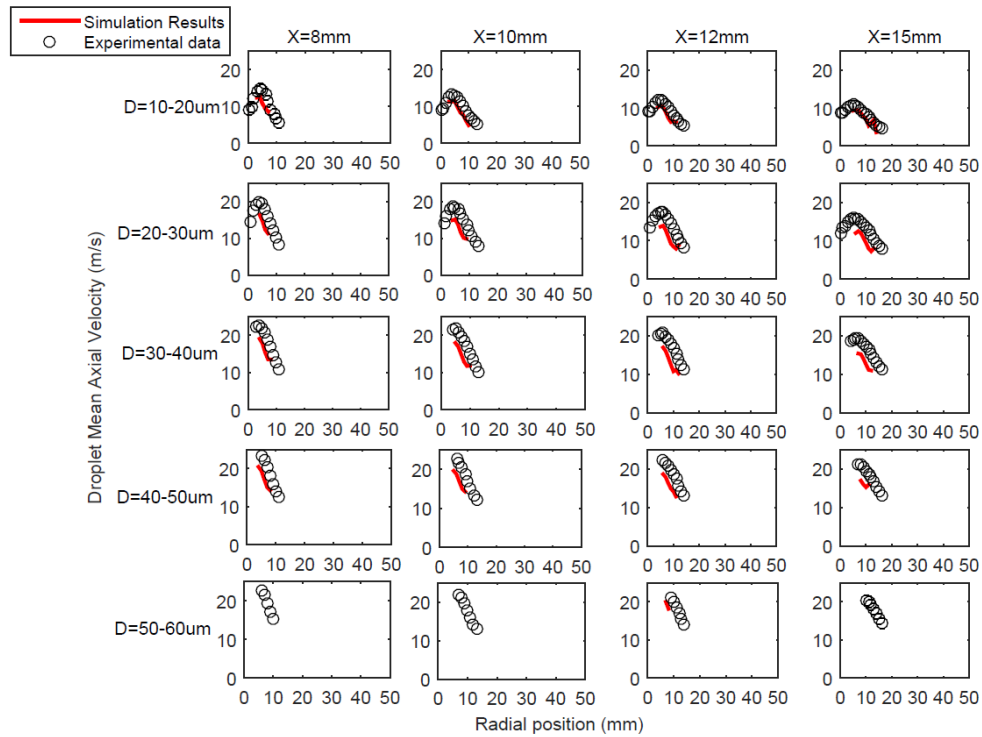


Figure 4.3 Radial profiles of mean droplet axial velocity for elevations of 8mm to 15 mm at 4 bar injection pressure in the injection model

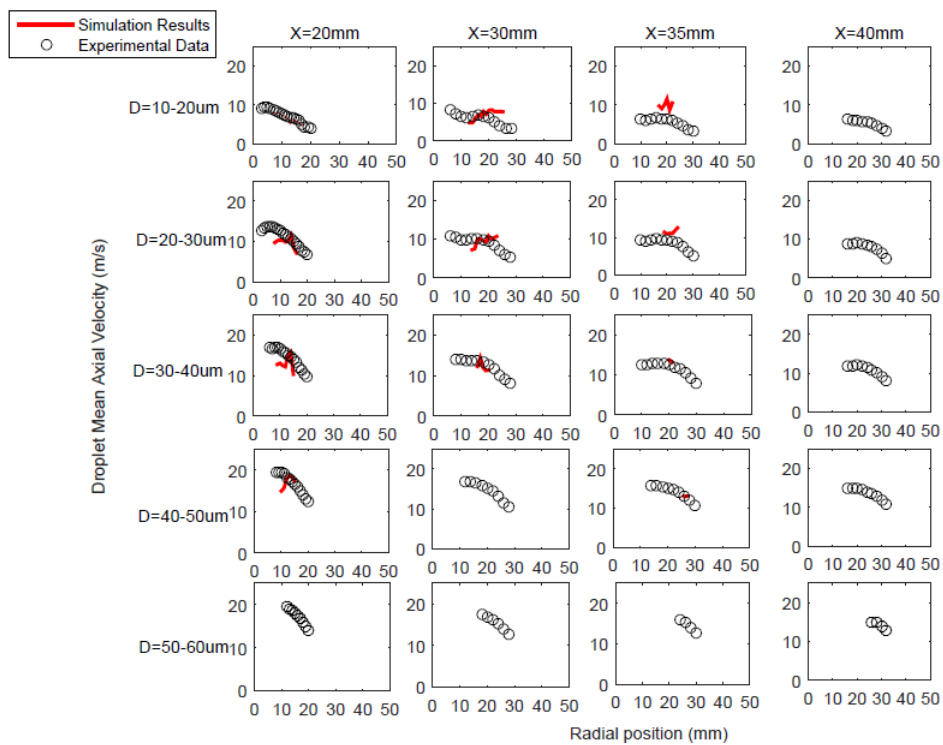


Figure 4.4 Radial profiles of mean droplet axial velocity for elevations of 20mm to 40 mm at 4 bar injection pressure in the injection model

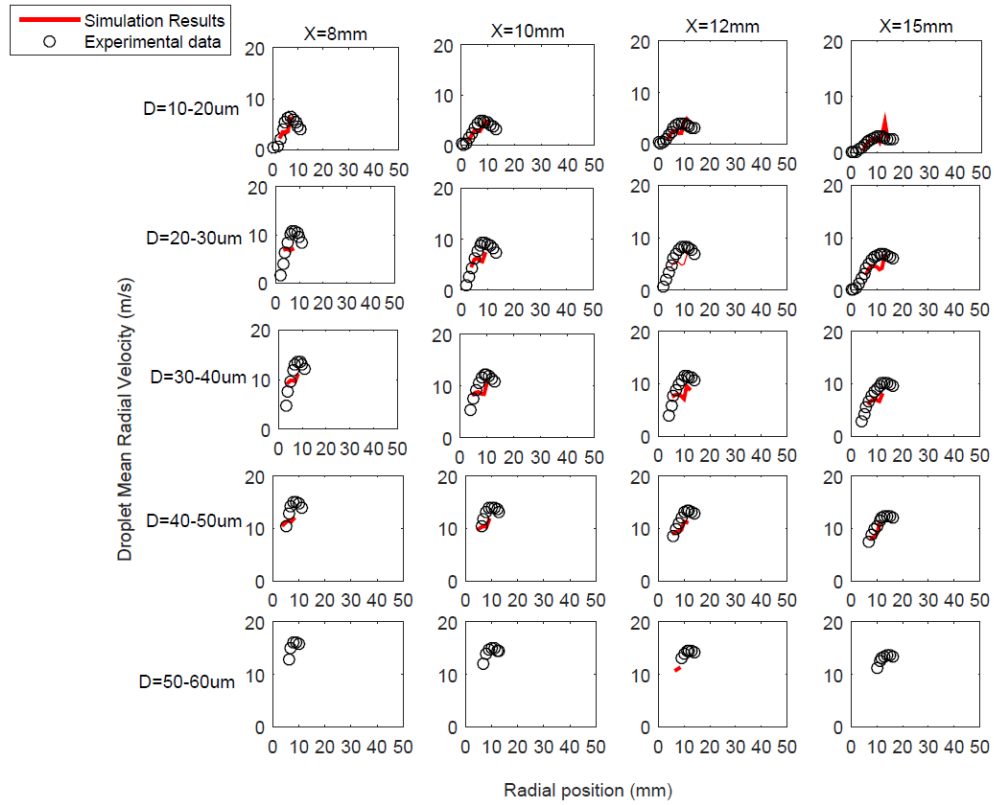


Figure 4.5 Radial profiles of mean droplet radial velocity for elevations of 8mm to 15 mm at 4 bar injection pressure in the injection model

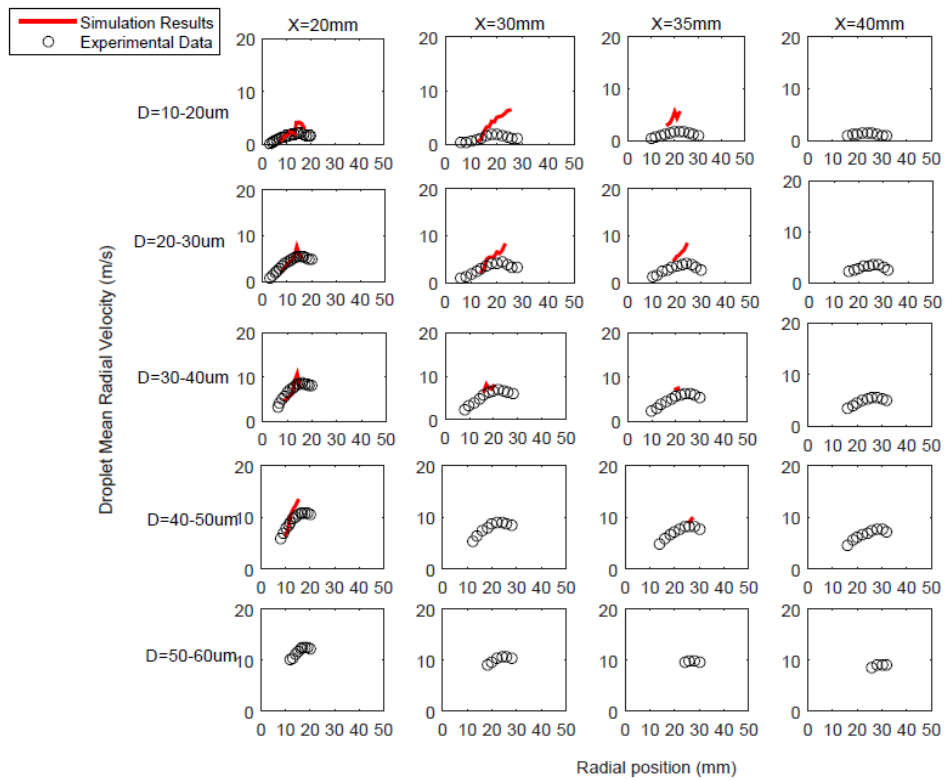


Figure 4.6 Radial profiles of mean droplet radial velocity for elevations of 20mm to 40 mm at 4 bar injection pressure in the injection model

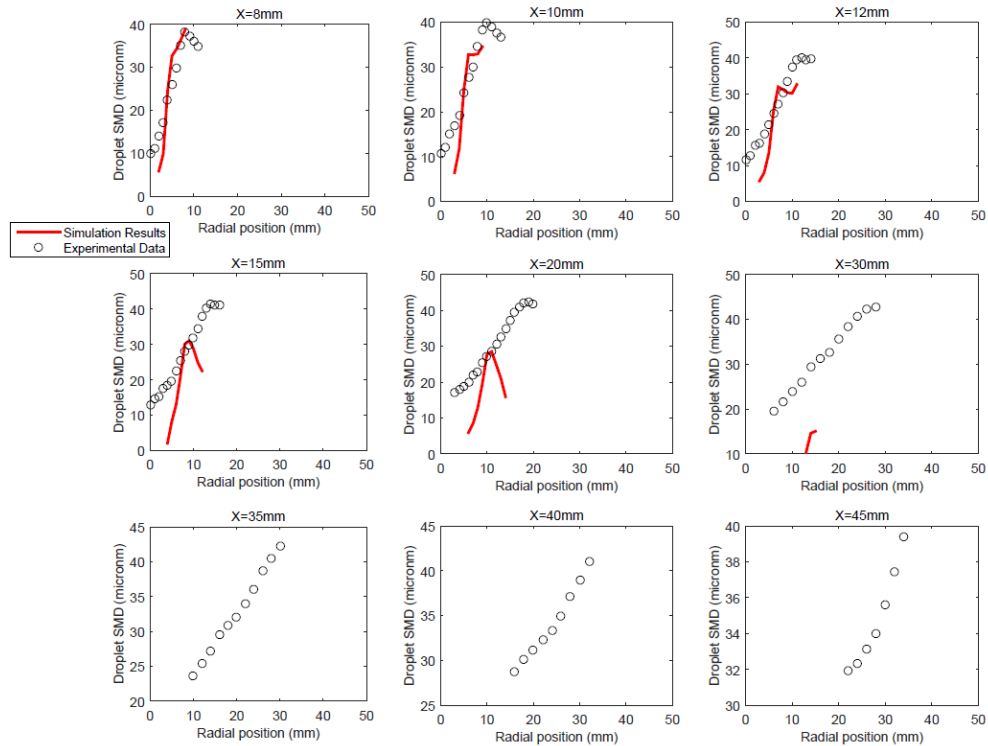


Figure 4.7 Sauter Mean Diameter(d_{32}) of the droplets at 4 bar injection pressure in the injection model

Due to the under-prediction of the droplet profiles, the injection pressure has to be increased further to investigate the effect of it on the droplet velocity profiles.

Injector pressure of 6 bar

The injector pressure of 6 bar is considered for this case for the H_{II} flame and as before, the droplet profiles are plotted and compared with the experimental results. From Figure 4.8 and Figure 4.9, we can observe that the droplet axial velocity profiles up to an elevation of 20mm are predicted well by the simulations for all droplet size ranges. Also, the spread of the droplets along the radial distance is predicted well by the model. The larger droplets have higher velocity than the smaller size droplets which is predicted well by the model as well.

But from the elevation of 30mm, the axial velocity profiles are under-predicted when compared to experimental results for all the droplet size ranges. This shows that even though the selected injection pressure predicts the droplet axial velocity well up to a certain elevation, at higher elevations, the axial velocity profiles don't match with the experimental results. The under-predicted droplet velocities at higher elevations is because of droplet velocities being reduced as a result of drag effects acting on the spherical droplet and inertia acting on the droplet. The under-prediction is also due to inaccurate initial spray conditions set for the simulations which affect the droplet velocity at higher axial locations.

A similar prediction trend follows for the droplet radial velocity profiles in Figure 4.10 and Figure 4.11. The SMD profiles of the droplet are shown in Figure 4.12. The droplet diameters are predicted well for all the elevation by the model except in the near axis region where the

diameter is under-predicted. This is due to under-prediction of the droplet size by the Rosin-Rammler size distribution.

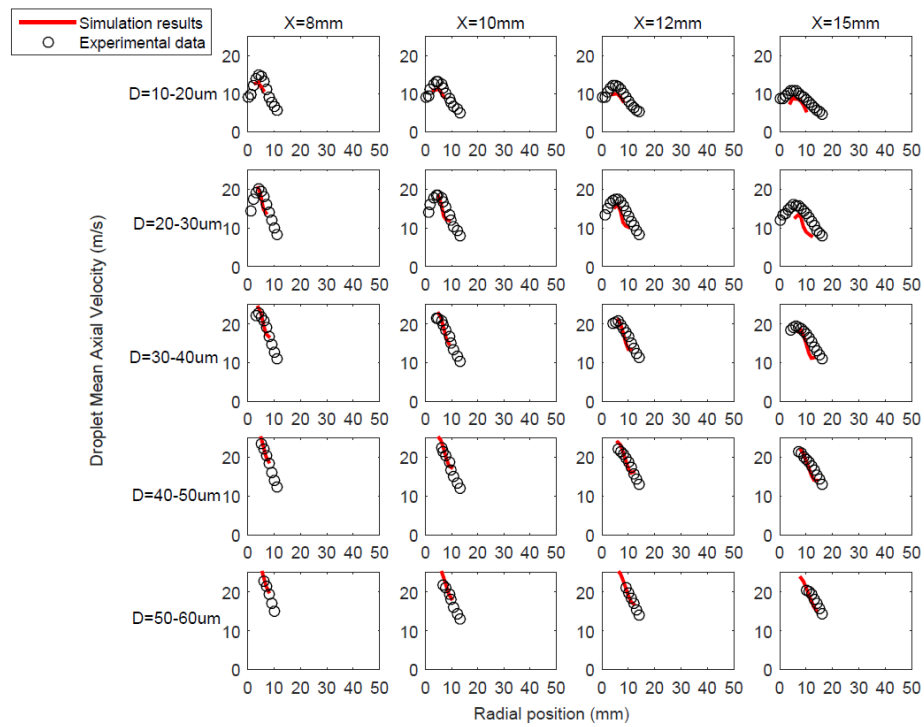


Figure 4.8 Radial profiles of mean droplet axial velocity for elevations of 8mm to 15 mm at 6 bar injection pressure in the injection model

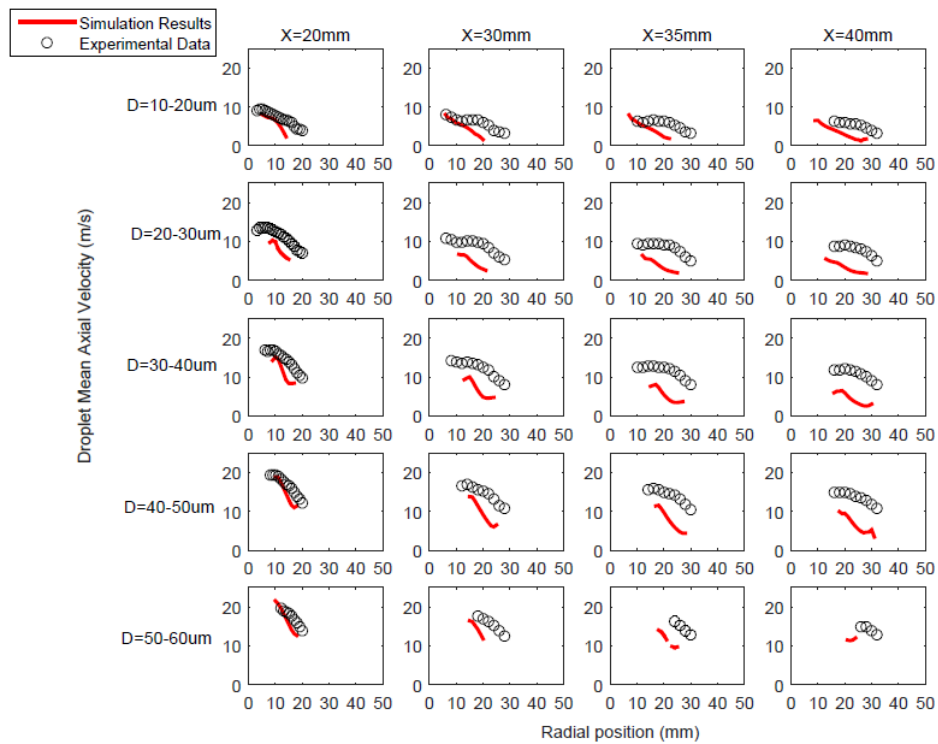


Figure 4.9 Radial profiles of mean droplet axial velocity for elevations of 20mm to 40 mm at 6 bar injection pressure in the injection model

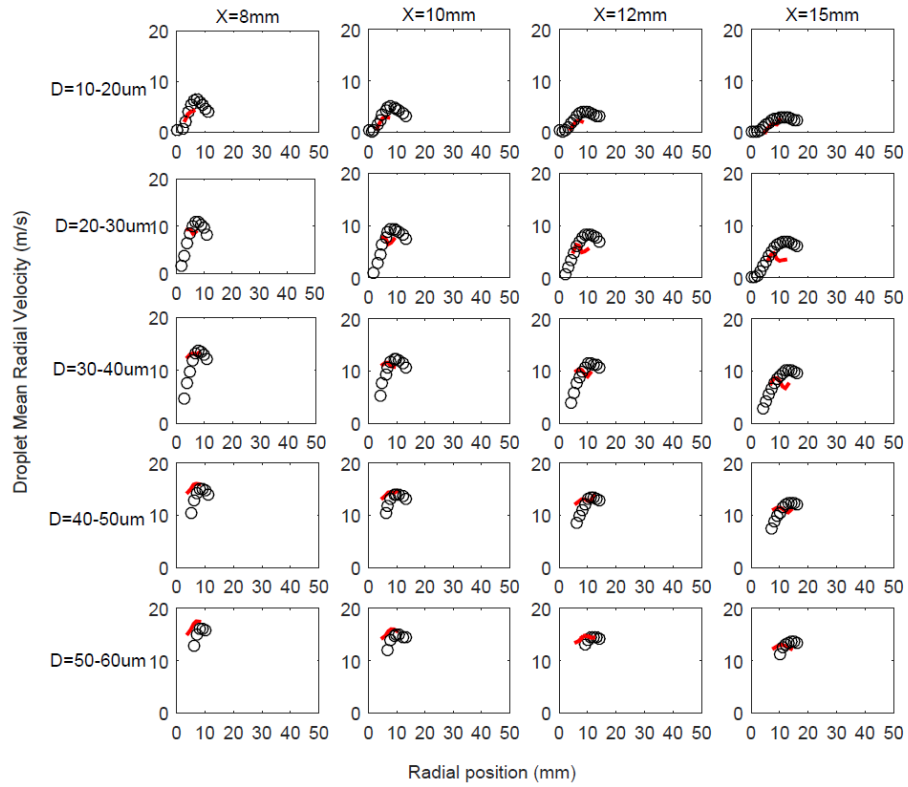


Figure 4.10 Radial profiles of mean droplet radial velocity for elevations of 8mm to 15 mm at 6 bar injection pressure in the injection model

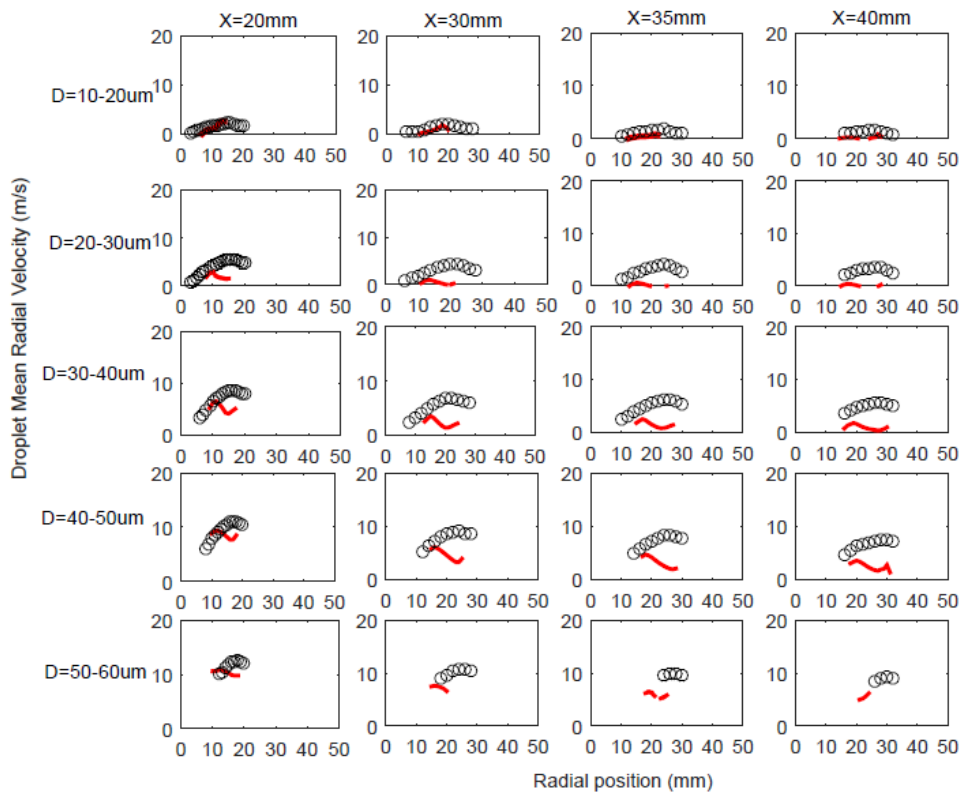


Figure 4.11 Radial profiles of mean droplet radial velocity for elevations of 20mm to 40mm at 6 bar injection pressure in the injection model

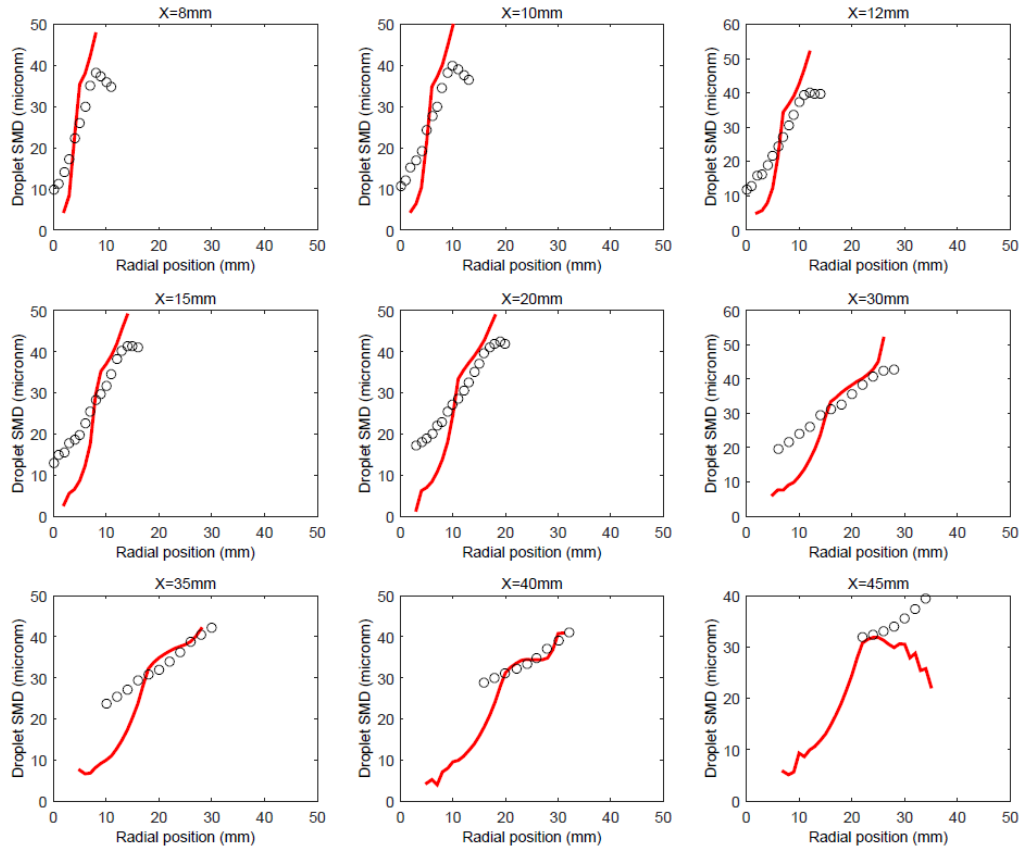


Figure 4.12 Sauter Mean Diameter(d_{32}) of the droplets at 6 bar injection pressure in the injection model

The injection pressure of 6 bar used gave satisfactory droplet velocity profiles and the droplet diameters are predicted well within the limits of the experimental data. This pressure is used for the further model comparison studies carried out for the H_{II} case. Now in order to confirm the optimized injection pressure, one more case with increased pressure of 10 bar is selected and the droplet velocity profiles are compared.

Injector pressure of 10 bar

The injector pressure of 10 bar is used to optimize the model further to check the effects on the droplet velocity profiles. From the Figure 4.13 and Figure 4.14, we can see that the droplet axial velocity profiles are over-predicted for elevations up to 30mm for all the range of droplet size distribution. The axial velocity of the droplet is under-predicted for elevations from 35mm due to reasons stated in the case of 6 bar injection pressure. The radial axial velocity profiles follow the same trend as the axial velocity profiles as shown in Figure 4.15 and Figure 4.16. The SMD for the 10 bar injection pressure is shown in Figure 4.17 and we can see that the droplet diameters are predicted well as in the case of 6 bar injection pressure. The under-prediction of droplet diameter near the axis region is similar to the reasoning in the case of 6 bar injection pressure.

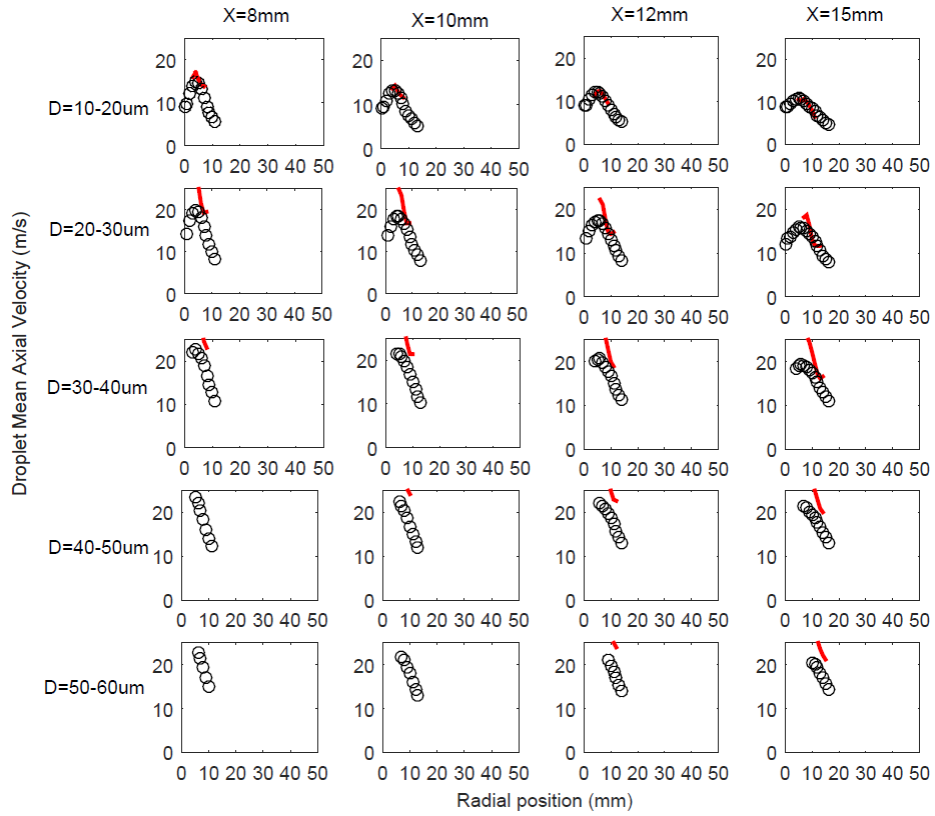


Figure 4.13 Radial profiles of mean droplet axial velocity for elevations of 8mm to 15 mm at 10 bar injection pressure in the injection model

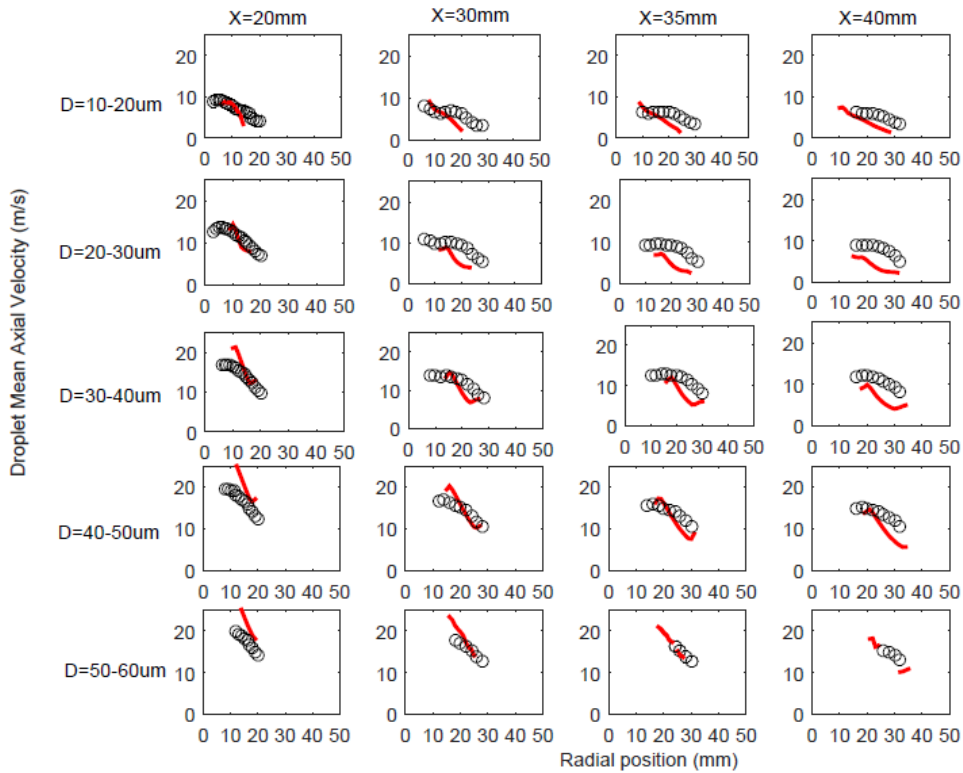


Figure 4.14 Radial profiles of mean droplet axial velocity for elevations of 20mm to 40mm at 10 bar injection pressure in the injection model

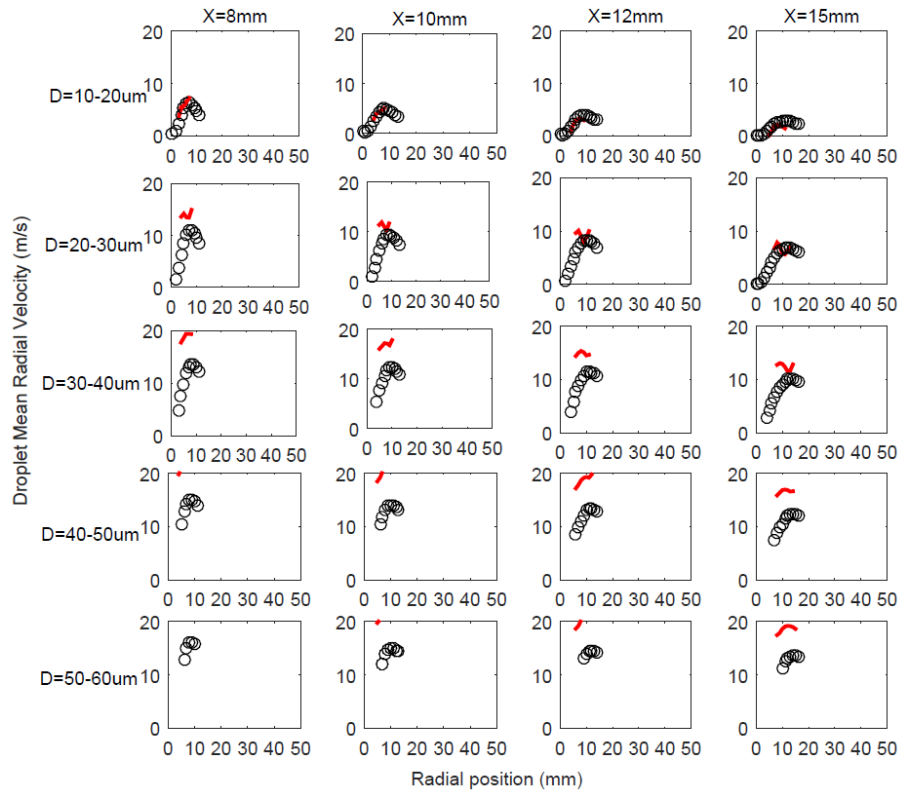


Figure 4.15 Radial profiles of mean droplet radial velocity for elevations of 8mm to 15mm at 10 bar injection pressure in the injection model

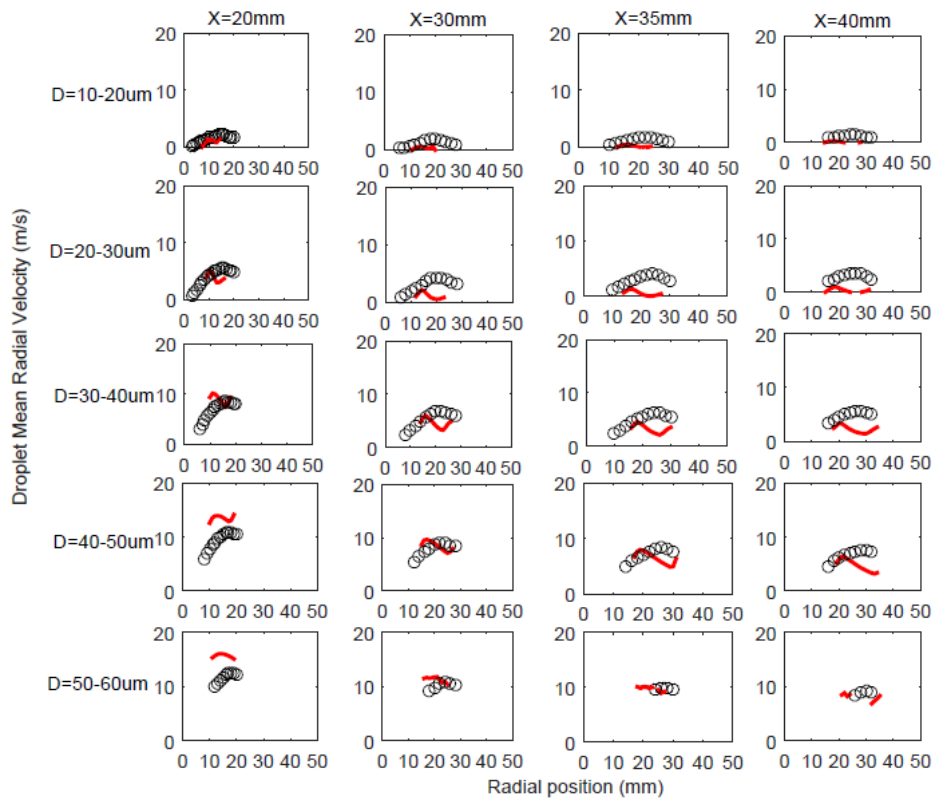


Figure 4.16 Radial profiles of mean droplet radial velocity for elevations of 20mm to 40mm at 10 bar injection pressure in the injection model

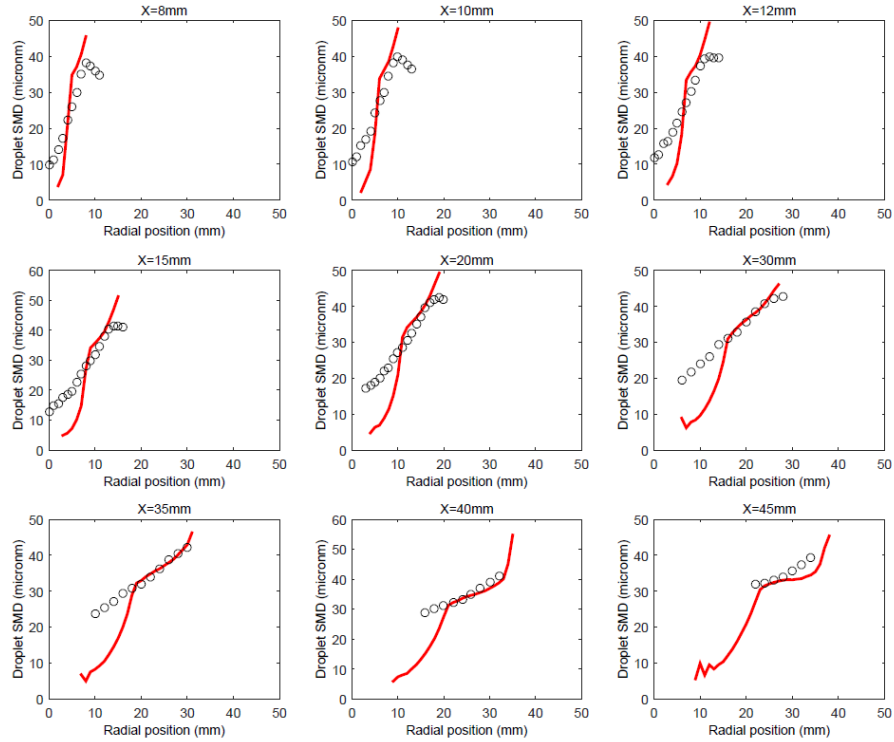


Figure 4.17 Sauter Mean Diameter(d_{32}) of the droplets at 10 bar injection pressure in the injection model

From the injection pressure analysis done for the H_{II} case of the spray combustion, it can be concluded that of the three considered cases, pressure of six bar is the most optimal one. We can see that the injection pressure used for the injector model in simulation is different from that of the injector pressure used for the experiments (refer Table 4.1). This is attributed due to experiments selecting injection pressure of fuel based on atomizer design and coefficient of discharge used for the nozzle. (The pressure optimization for H_{II} flame is also studied with evaporation modeled by Spalding model for injection pressures of 4 bar, 6 bar and 10 bar. The droplet profiles obtained for this case is similar to the profiles obtained for the gradient diffusion model with no droplets at higher axial locations. The droplet profiles are given in Appendix A.2 for reference.)

4.2 Model Comparisons

In this section, the different models for turbulence and evaporation are studied with the optimized injection pressure of 6 bar and the results are explained here. From the results, we can identify the best performing model for the turbulent spray combustion in OpenFOAM. The models compared have been explained in detail in the model equations in Chapter 2 (Section 2.5.3 and Section 2.2). A comparative study of one-step mechanism and detailed mechanism has also been made and preliminary conclusions are made in the Appendix A.1

4.2.1 Evaporation model

In this subsection, the evaporation models analyzed are the gradient diffusion model and the Spalding evaporation model explained in Chapter 2. In this section, standard $k-\varepsilon$ model is

used with one-step chemistry of ethanol oxidation. The effect of the evaporation of the droplets on the gas phase temperature and gas phase velocities are analyzed here. As mentioned in Chapter 2, in a single droplet, the droplet surface starts heating up because of temperature difference between the droplet surface and surrounding gas. Once the droplet surface gets heated up, heat now transfers to the inner core of the droplet by means of conduction from the droplet surface until equilibrium is achieved. Once the temperature of the droplet reaches the boiling point of fuel, the droplet starts evaporating. This evaporation effect described by two models is studied with the optimized injection pressure and model predictions are compared.

From Figure 4.18, we can infer that the gas phase temperature profile for the gradient diffusion model is under-predicted. The main drawback of the gradient diffusion model is that it does not consider the Stefan flow which is the convective flow of the fuel vapor and gas from the droplet surface (S.Sazhin, 2006). This causes inaccurate droplet evaporation rate prediction by the model. Also, the gradient diffusion model is originally derived for mass diffusion through porous wall (Miller, Harstad, & Bellan, 1998). Hence usage of this gradient diffusion model for droplet evaporation involving phase change results in inaccurate temperature prediction. On the other hand, Spalding evaporation model predicts the gas phase temperature better than the diffusion model due to consideration of the Stefan flow in its evaporation rate equation. Hence, better evaporation rate prediction by the Spalding model gives accurate gas phase temperature profile for the simulation.

When we look at the gas phase velocity field in Figure 4.19, we can see that the gas phase axial and radial velocity for both the evaporation models are predicted well within the region where experimental data are available. The peak gas phase axial velocity near the injector axis for both the model occurs due to the acceleration of gas phase by momentum transfer from the small droplets near the injector region which affects the gas phase velocity in that region. The peak gas phase axial velocity is also due to higher gas phase temperature prediction in the model which leads to expansion of gas phase near the injector region.

The initial rise and drop in the radial profile of the gas phase axial velocity near the injector axis is not predicted well for lower elevations for both the models. The initial rise of gas phase axial velocity is attributed to large number of atomized droplets near the injector transferring the momentum to accelerate the gas phase. This phenomenon is not captured well by the model and it can be attributed to inaccurate initial spray conditions used in the simulation.

Now, the droplet velocity profiles are analyzed to check if the models are able to capture the droplet distribution at higher axial locations to have a complete insight of the working of the evaporation models. When the droplet axial velocity profile at elevations of 30mm to 40mm is analyzed in Figure 4.20, we can observe that for the Spalding model, there are very few droplets of size 10 μ m to 40 μ m at elevations of 30mm to 40mm and there are no large droplets in any of the elevations. When we compare Figure 4.9 which gives droplet axial velocity for gradient diffusion model and Figure 4.20, we can see that the droplets have evaporated more quickly in Spalding model than in gradient model. The same trend follows

for the radial velocity profiles for the Spalding model and gradient model in Figure 4.21 and Figure 4.11 respectively.

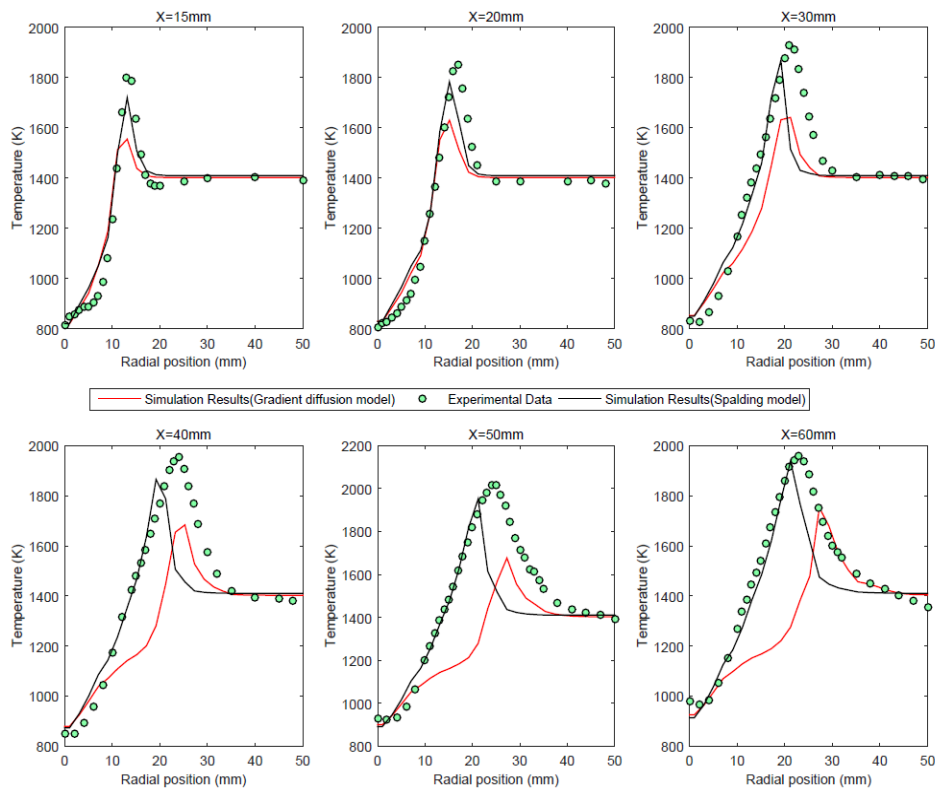


Figure 4.18 Gas phase temperature comparison for the evaporation models

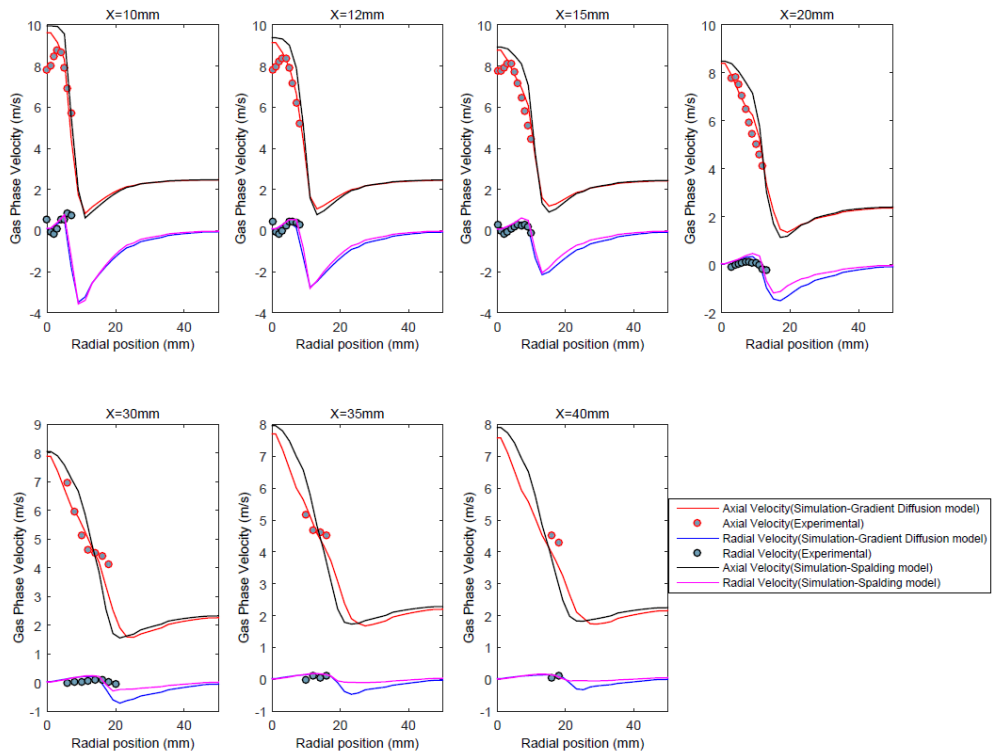


Figure 4.19 Gas phase temperature comparison for the evaporation models

The SMD analysis for Spalding model from Figure 4.22 shows that droplets are not present at higher axial locations due to much higher evaporation rate than the gradient model in Figure 4.12

The too high evaporation rate obtained by using Spalding model could be avoided in the future by using better spray boundary conditions. From the above analysis of the various field plots we can say that even though the gas phase temperature prediction for the Spalding model is better than the gradient model, the higher evaporation rate makes it difficult to analyze the droplet properties at higher axial locations. Hence for this simulation study, taking into the account of the evaporation rate, gradient diffusion evaporation model is used as the optimized one for the study of H_I , H_{II} and H_{III} flames.

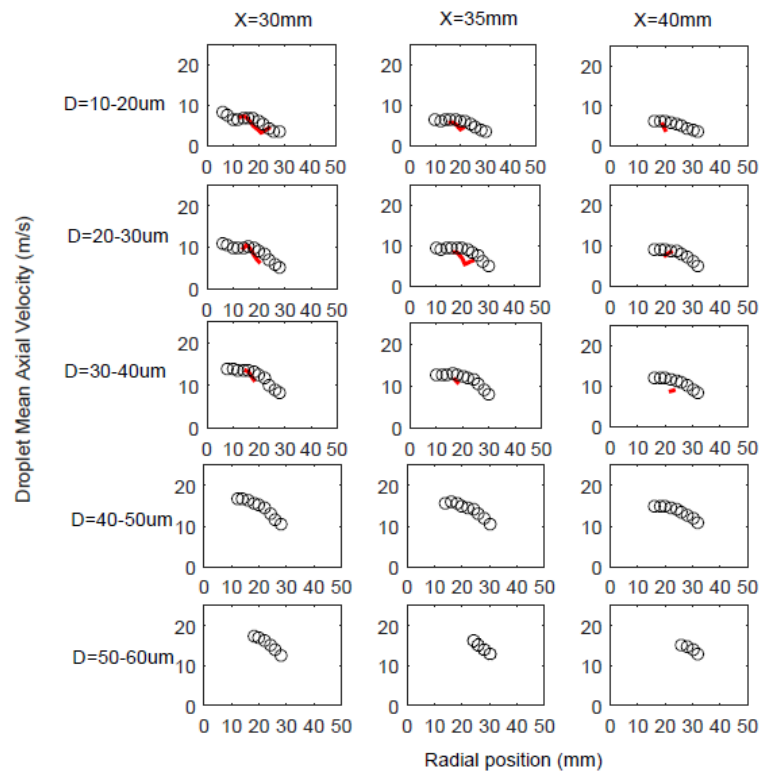


Figure 4.20 Radial profiles of mean droplet axial velocity for Spalding model at elevations of 30-40mm with 6 bar injection pressure in the injection model

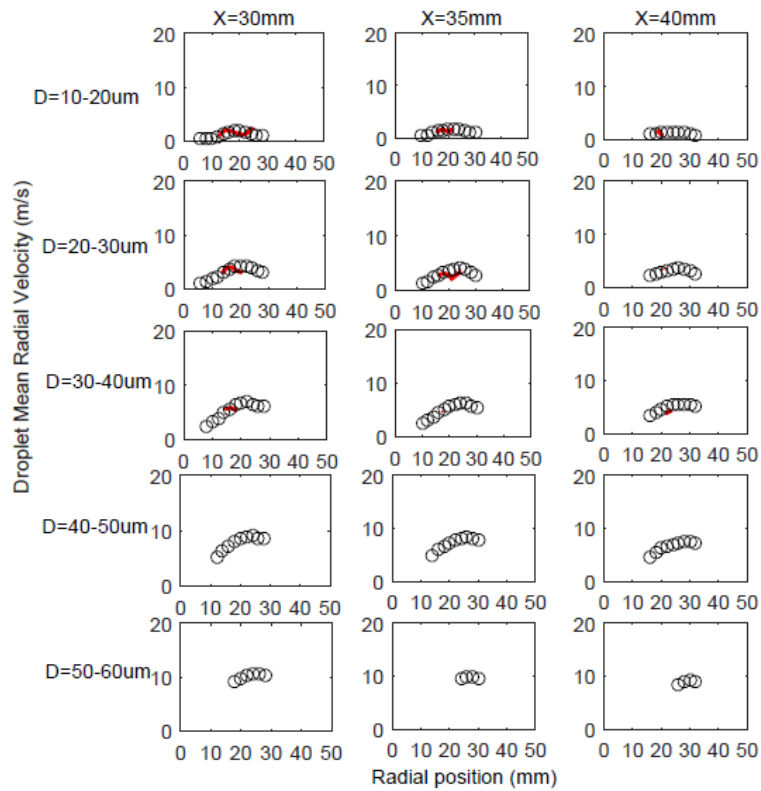


Figure 4.21 Radial profiles of mean droplet radial velocity for Spalding model at elevations of 30-40mm with 6 bar injection pressure in the injection model

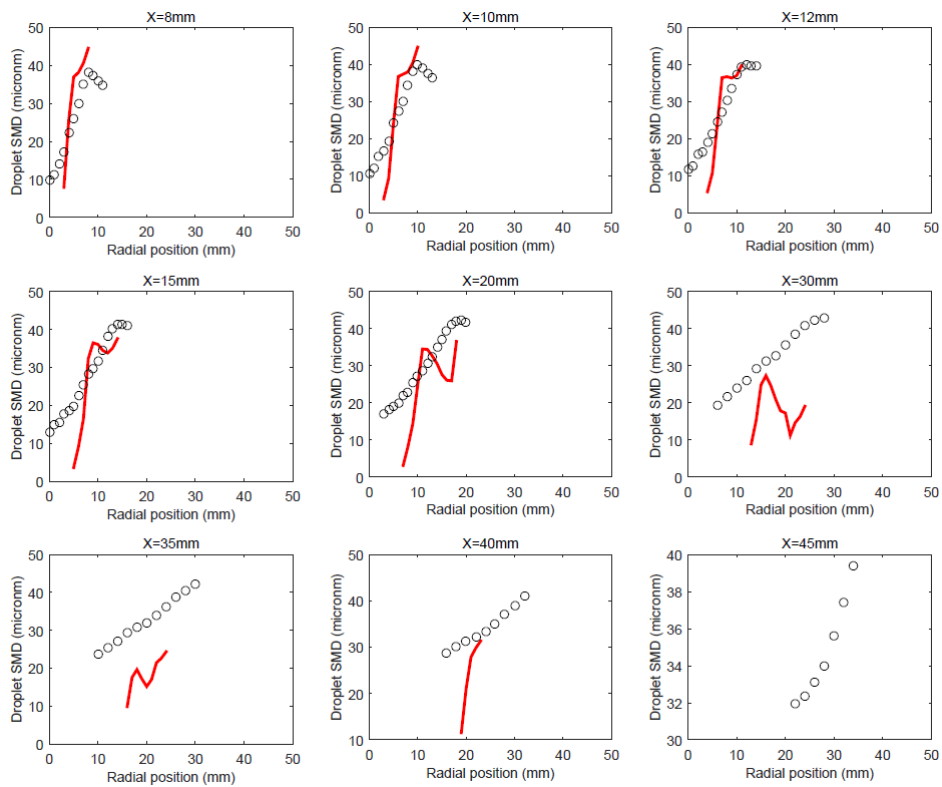


Figure 4.22 SMD for the Spalding model with 6 bar injection pressure in the injection model

4.2.2 Turbulence model

As mentioned in Chapter 2, the turbulence models are used to close the unknown Reynolds stress tensor in the density averaged Navier stokes equations in RANS simulations. The models compared are the standard $k-\varepsilon$ model and realizable $k-\varepsilon$ model. In this section, gradient diffusion evaporation model is used with one-step chemistry of ethanol oxidation. The different parameters analyzed for the turbulence model comparison studies are the gas phase temperature profiles and the gas phase velocity profiles.

The gas phase temperature profile for different elevations is show in Figure 4.23. From the figure, we can infer that the gas phase temperature profiles for the realizable $k-\varepsilon$ model are lower than the standard $k-\varepsilon$ model. This under-prediction is due to the combustion model (PaSR) used since in the combustion model, the mean source term is calculated based on the mixing time which in the combustion model is taken proportional to turbulence frequency, ε/k . The scalar dissipation term gives a measure of the chemical reaction rate based on the mixing of reactants. Hence it has a profound effect on the gas phase temperature profile. The gas phase velocity profiles are given in Figure 4.24. From the figure, we can see that the gas phase velocity profiles are not much affected by the type of turbulence model employed since even though the k and ε predicted by these two models differ, the mean velocity calculated by both the models is very similar.

From the comparison study, it is concluded that for the PaSR combustion model, standard $k-\varepsilon$ model gives more accurate results than the realizable $k-\varepsilon$ model.

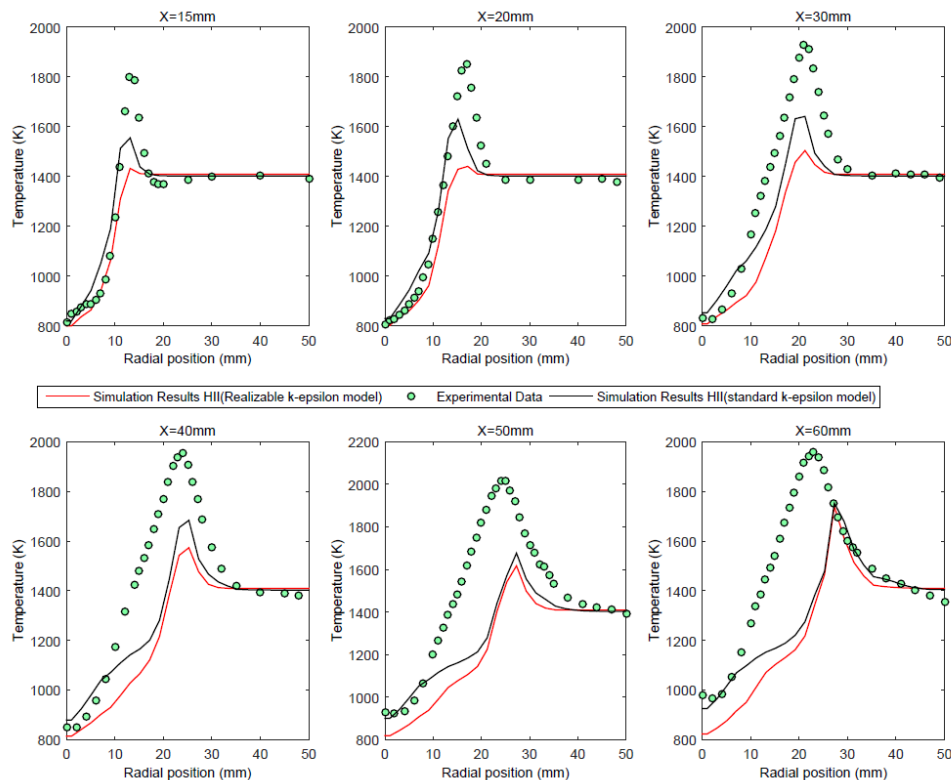


Figure 4.23 Gas phase temperature profile comparison between the turbulence models for different elevations

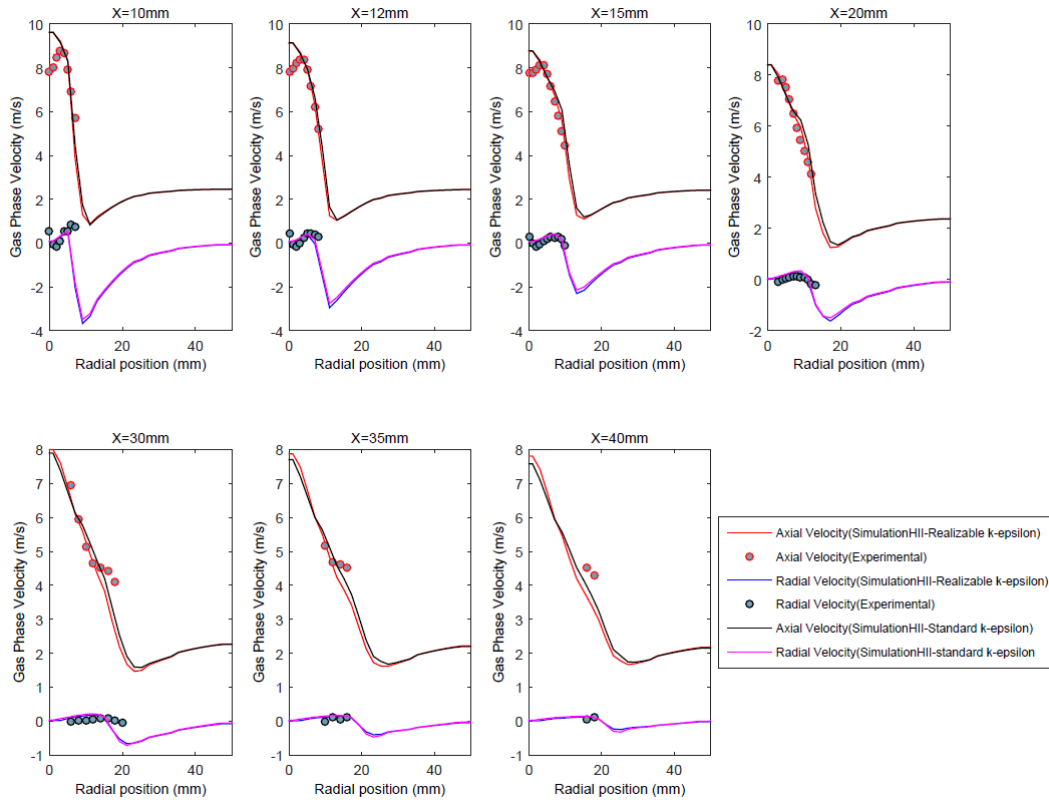


Figure 4.24 Gas phase velocity profile comparison between the turbulence models for different elevations

4.3 MILD combustion phenomenon in H_{II} flame

In order to check whether the definition of MILD combustion is satisfied by the DSHC flame experiments and simulations for the H_{II} case, gas phase temperature profile for the H_{II} flame is analyzed. The case is simulated with 6 bar injection pressure with evaporation and turbulence modeled by gradient diffusion and standard $k-\epsilon$ model respectively. One-step global mechanism is used for ethanol oxidation.

From Figure 4.25, the peak temperature for the experiments occurs at radial distance of 24mm and elevation of 50mm. The temperature found at this point is 2017K. From the simulations, we can find that the peak temperature happens at a radial distance of 27mm and elevation of 60mm. The temperature at this point is 1752K. Now by the definition of MILD combustion given in Chapter 1, “A combustion process is named MILD when the inlet temperature of the reactant mixture is higher than mixture self-ignition temperature whereas maximum allowable temperature increase with respect to inlet temperature during combustion is lower than mixture self-ignition temperature (in Kelvin)” (Cavalierea & Joannon, 2004), we can find whether H_{II} flame satisfies the definition of MILD combustion.

Self-ignition temperature of ethanol = 638.15K (Engineering Toolbox - Fuels and Chemicals - Autoignition Temperatures)

Inlet temperature of the coflow = 1400K (representative temperature)

Peak gas phase temperature in experiment = 2017K

Temperature increase with respect to inlet temperature = $2017 - 1400 = 617\text{K} < 638.15\text{K}$

From the above calculations, we can observe that the definition of MILD combustion in H_{II} flame is satisfied by the experiments. Now for the simulations,

Peak gas phase temperature in simulation = 1752K

Temperature increase with respect to inlet temperature = $1752 - 1400 = 352\text{K} < 638.15\text{K}$

We can observe that there is peak temperature under-prediction by the numerical model as it is attributed due to PaSR combustion model and global reaction mechanism's limitations. Therefore also according to the numerical model, the H_{II} flame satisfies the criterion for MILD combustion.

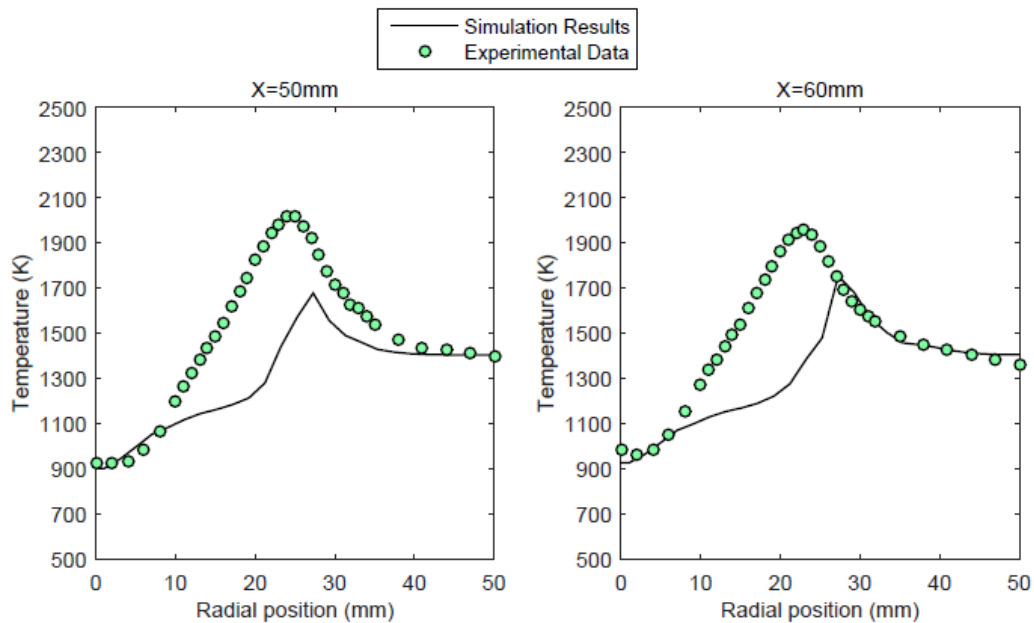


Figure 4.25 Gas phase temperature profile for H_{II} flame at elevation of 50mm and 60mm

4.4 Effect of coflow conditions on ethanol spray flames

In this section, results for flames H_I, H_{II}, and H_{III}, having different coflow conditions used for the simulations are explained in detail here. The study of H_I and H_{III} flames is carried out with evaporation modeled by gradient diffusion model, turbulence modeled by standard $k-\varepsilon$ model and combustion modeled by PaSR model. The reaction mechanism for ethanol oxidation used is the global one-step mechanism formulated by Dryer (K. Westbrook & L. Dryer, 1981).

4.4.1 H_I flame

Based on the models selected from the study described above, the numerical simulation of the H_I flame is carried out by using the boundary conditions of the case from Table 4.1. The injection pressure optimization of injector model for the H_I flame is carried out similar to the case of H_{II} based on trial and error method. It is done with a pressure of 6 bar, 6.5 bar and 8 bar to arrive at the pressure of 6.5 bar as optimized one and it is used for the simulation of H_I case. In this case study of effect of the coflow on the ethanol spray flames, various parameters like gas phase temperature, velocity profiles, droplet velocity and diameter are examined to arrive at possible conclusions for the case. Spray properties like injector diameter and dispersion angle are kept the same as in H_{II} case.

Gas phase temperature and velocity field

First, the gas phase temperature profile and gas phase velocity profiles are examined for the H_I flame. Figure 4.26 gives the gas phase temperature profiles at various elevations. From the figure, at lower elevations of 15mm and 20mm, near the injector axis, we can see that the temperature is over-predicted. This can be attributed due to low evaporation rate of the droplets near the injector region. In both these elevations, the gas phase temperature is predicted quite well with the experimental data. At elevations of 30, 40 and 50mm we can see that the near axis temperature profile is predicted well but the peak temperature region is under-predicted. This under-prediction can be caused by the shortcomings of the reaction mechanism (global) and evaporation model employed in the study.

The gas phase velocity profiles are plotted in Figure 4.27. From the figure, we can see that the axial and radial velocity profiles are well predicted up to an elevation of 20mm. At higher axial location of 30 and 35mm, both the velocity profiles are under-predicted. In experiments, droplet axial velocity for droplets of size less than 6 μ m is used to approximate gas phase axial velocity. In the simulation results, when we analyze the mean droplet axial velocity at the elevation of 30mm and 35mm in Figure 4.27, we can observe that the droplet velocity is almost equivalent to the gas phase axial velocity at these elevations. Thus, low droplet velocities at these elevations cause the gas phase velocity under-prediction.

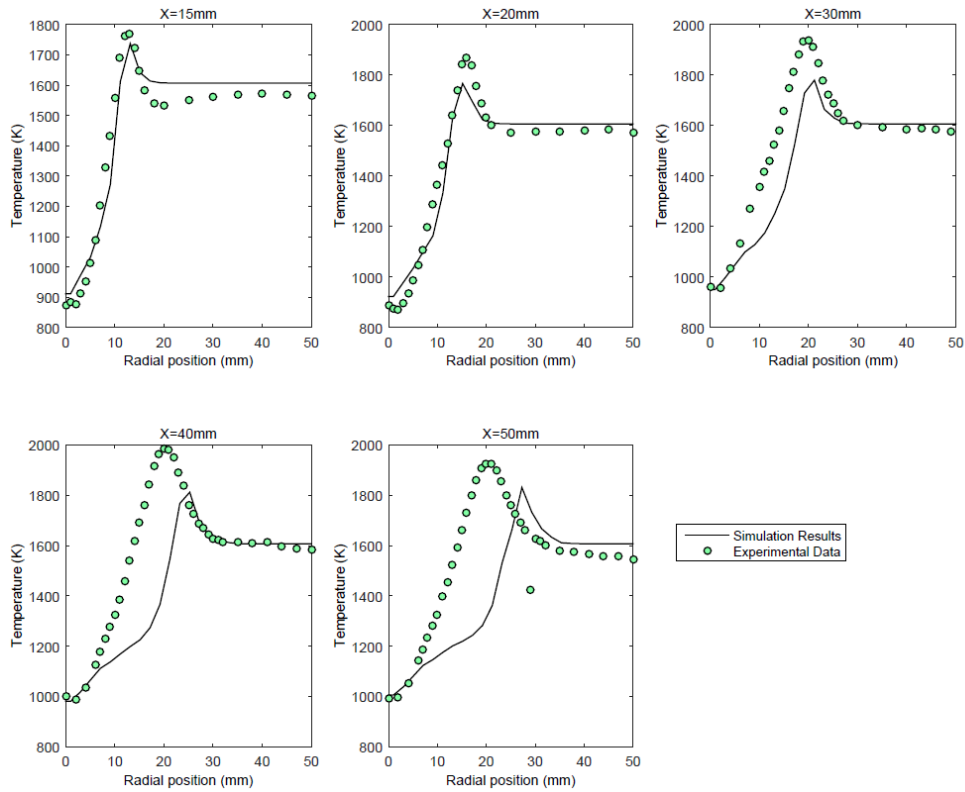


Figure 4.26 Gas phase Temperature profile for the H_1 flame at different elevations

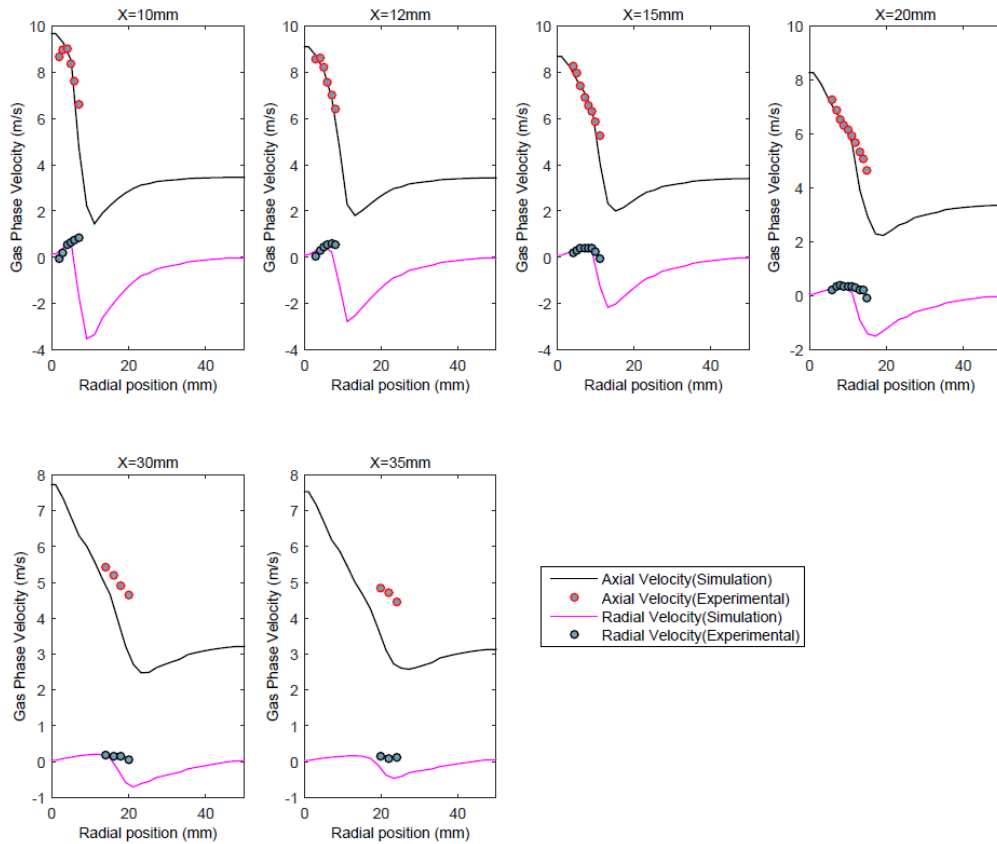


Figure 4.27 Gas phase velocity profile for the H_1 flame at different elevations

Droplet velocity field and diameter

Looking at the droplet axial velocity plots from Figure 4.28 and Figure 4.29, we can observe that at lower elevation of 8mm to 15mm, the droplet axial velocity matches well with the experimental data. But at higher axial locations of 20mm to 30mm, the axial velocity is under-predicted for the H_I flame. This under-prediction can be explained by the same reasoning of drag force acting on the spherical droplets and inaccurate spray initial conditions. The radial velocity plots are given in Figure 4.30 and Figure 4.31. The droplet radial velocity plots have similar level of agreement as the axial velocity profiles. Figure 4.32 gives the Sauter Mean Diameter of the droplet for the H_I flame. At the inner boundary of the experimental conical spray, the predicted SMD has correct magnitude but in general, the SMD is over-predicted. This could be due to the gradient diffusion model used, in which the evaporation rate is under-predicted.

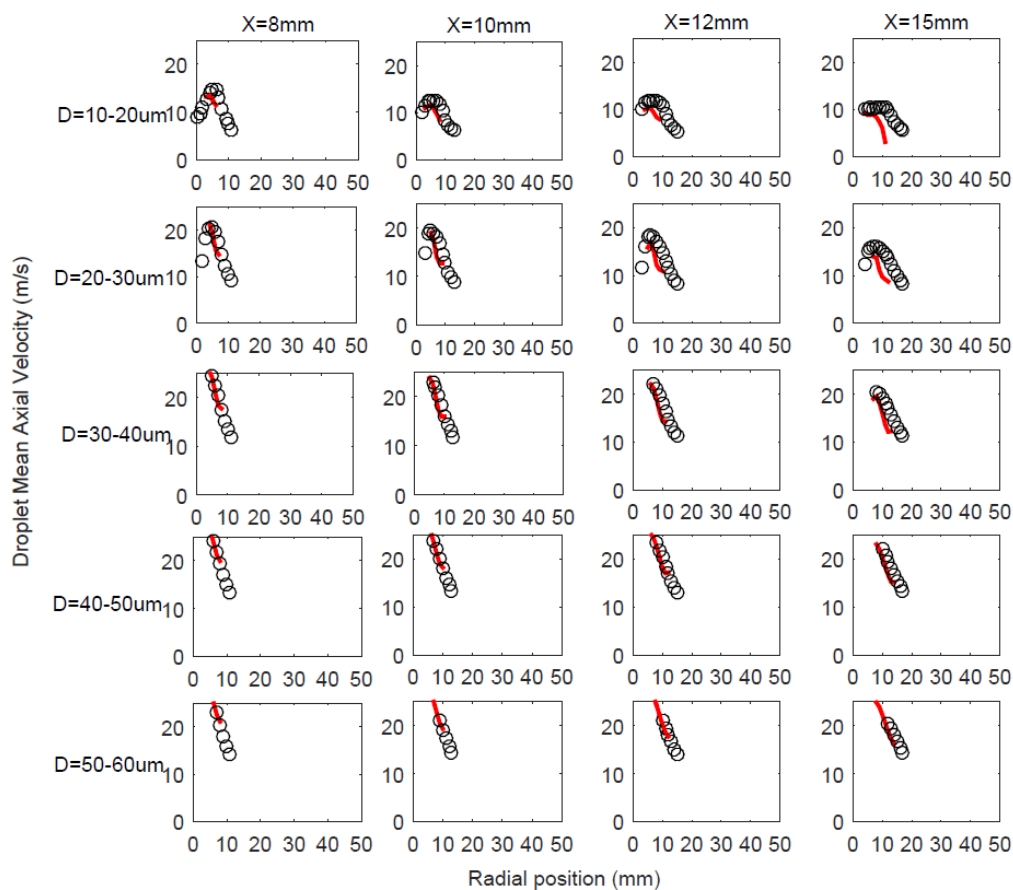


Figure 4.28 Radial profiles of mean droplet axial velocity for elevations of 8mm to 15mm for H_I flame with 6.5 bar injection pressure in the injection model

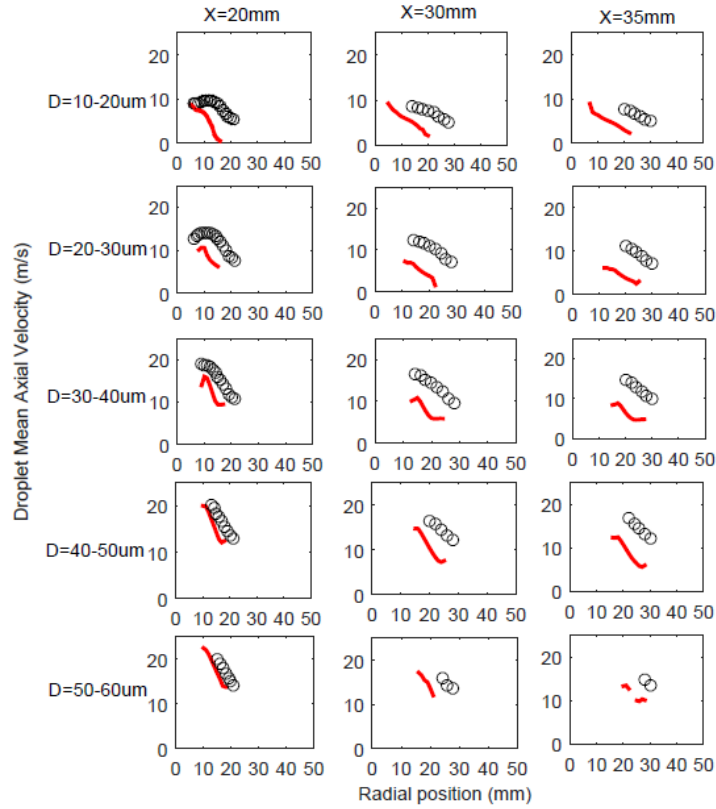


Figure 4.29 Radial profiles of mean droplet axial velocity for elevations of 20mm to 35mm for H_1 flame with 6.5 bar injection pressure in the injection model

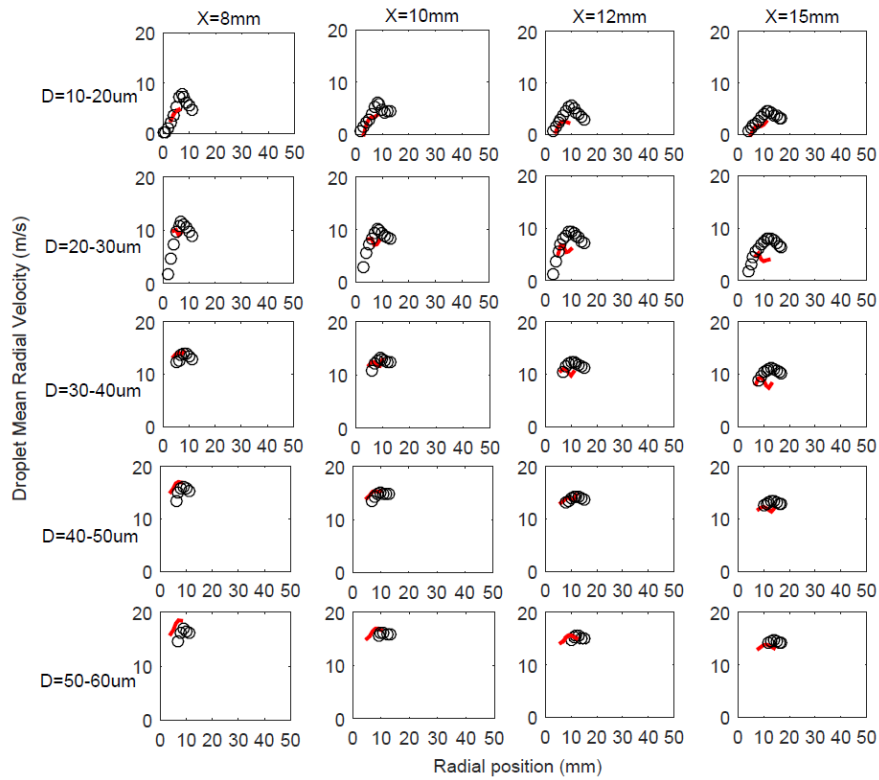


Figure 4.30 Radial profiles of mean droplet radial velocity for elevations of 8mm to 15mm for H_1 flame with 6.5 bar injection pressure in the injection model

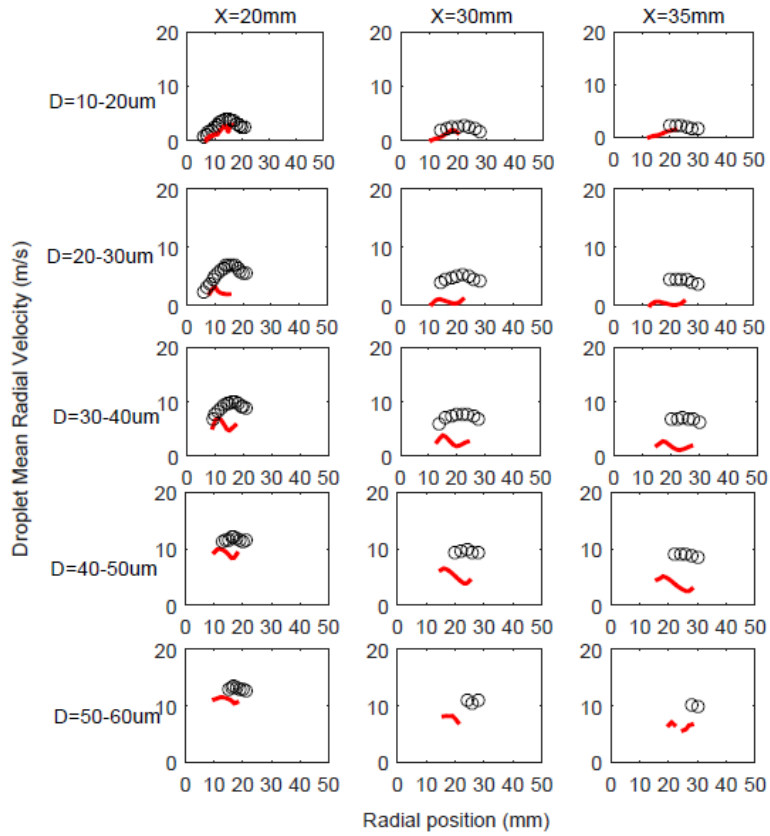


Figure 4.31 Radial profiles of mean droplet radial velocity for elevations of 20mm to 35mm for H_1 flame with 6.5 bar injection pressure in the injection model

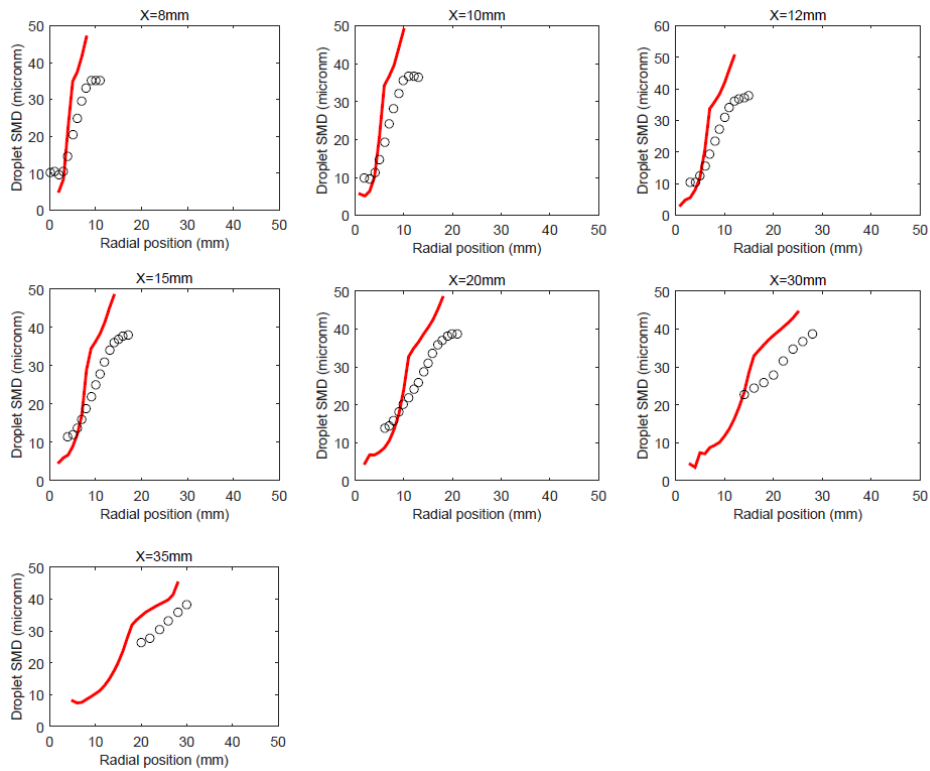


Figure 4.32 Droplet SMD for H_1 flame with 6.5 bar injection pressure in the injection model

4.4.2 H_{III} flame

The H_{III} flame is simulated using the initial conditions specified in Table 4.1. The case is specified based on the dilution and temperature of the coflow. The same optimization method for injection pressure is carried out. Injector pressure optimization for the injector model is done with a pressure of 6 bar, 6.5 bar and 8 bar to arrive at the pressure of 6.5 bar as optimized one and it is used for the simulation of H_{III} flame. The flame characteristic is studied by analyzing the plots for gas phase temperature, velocity and droplet velocity and diameter fields.

Gas phase temperature and velocity field

The gas phase temperature plots are presented in Figure 4.33. From the plot we can see that near the injector axis, the gas phase temperature is little bit under-predicted. This is due to low evaporation rate of injected droplets in the near nozzle region. This low evaporation rate is also created by the lower temperature of the coflow (1305K) used for the case. The peak gas phase temperature predictions have the same trend as in the case of H_I and H_{II} flames and is under-predicted. The under-prediction is again attributed due to the shortcomings of the reaction mechanism (global) and evaporation model employed in the case. Figure 4.33 gives the gas phase velocity plots. From the plots, we can observe that the model is able to predict both the axial and radial velocity in agreement with the experimental data in the radial range where droplets are found experimentally. But the axial velocity at the centerline is over-predicted.

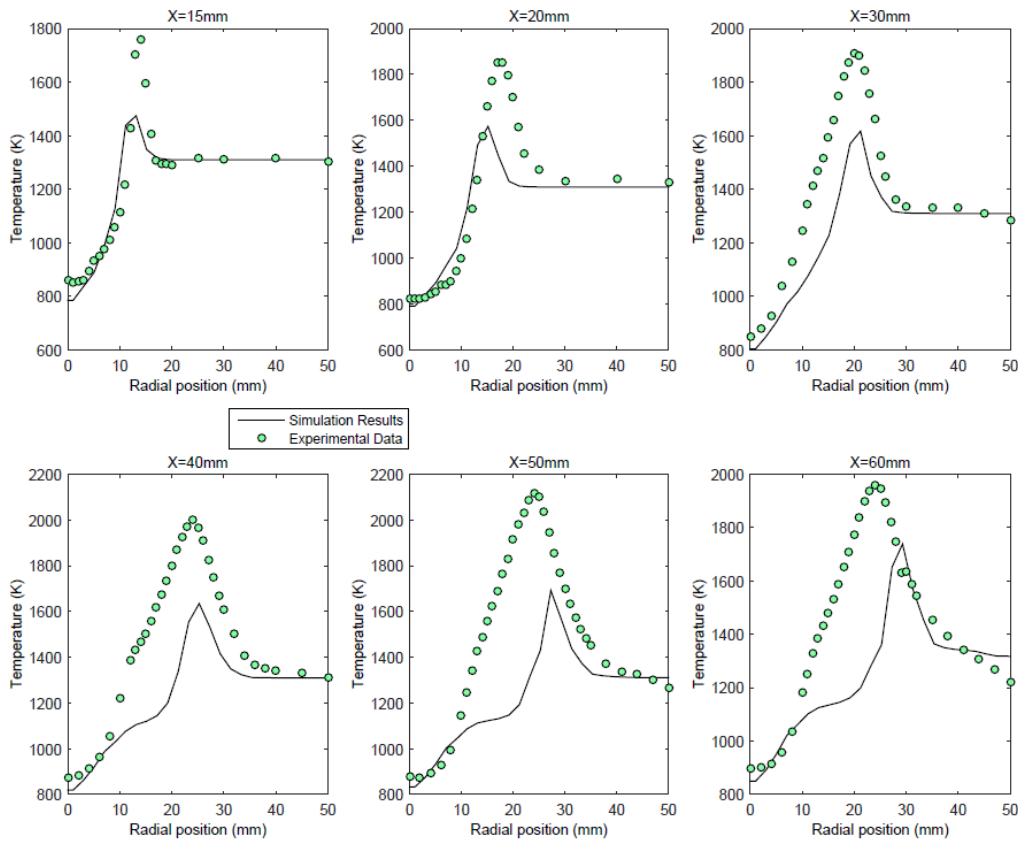


Figure 4.33 Gas phase Temperature profile for the H_{III} flame at different elevations

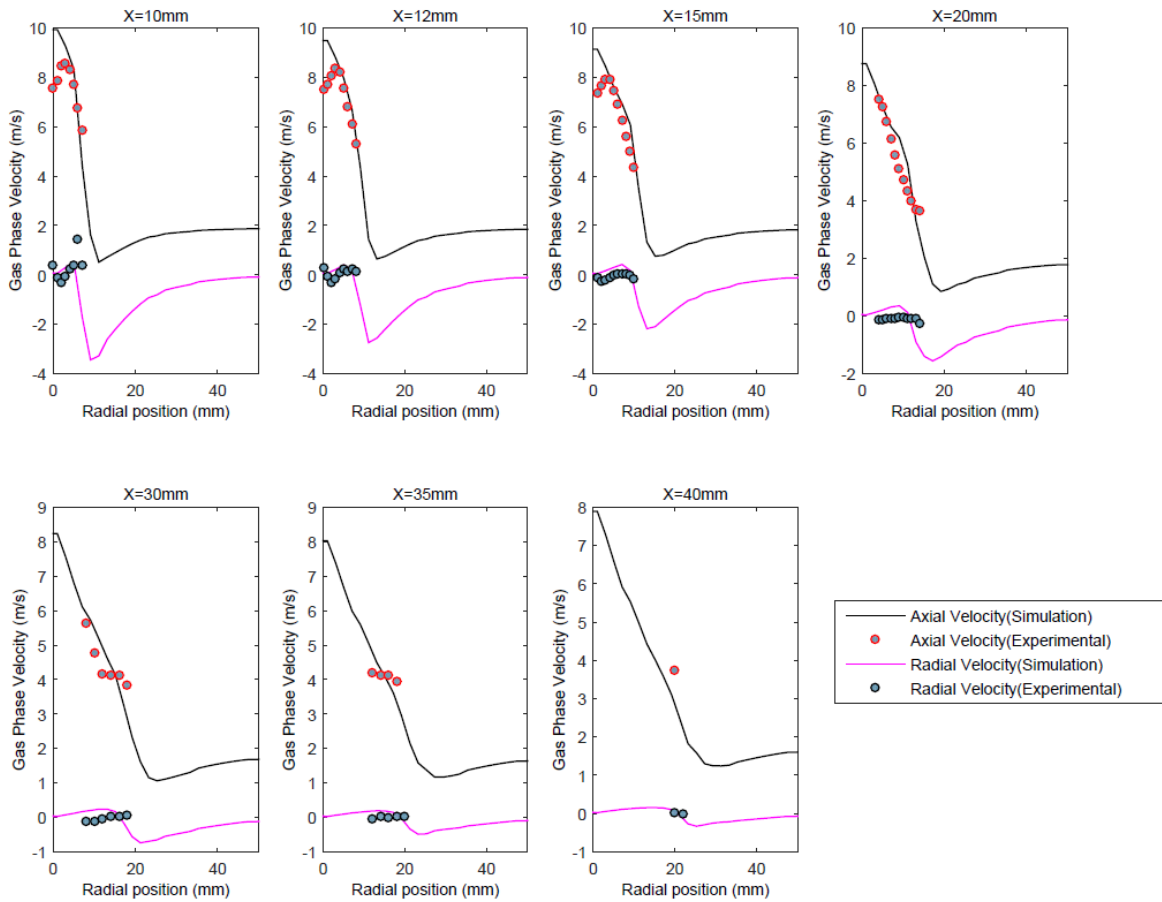


Figure 4.34 Gas phase velocity profile for the H_{III} flame at different elevations

Droplet velocity field and diameter

The droplet axial velocity plots are given in Figure 4.35 and Figure 4.36 for different elevations. The simulation results match well with the experimental data for lower elevations and for higher elevations, the under-prediction of the droplet velocity happens as in the case of both H_I and H_{II} . This under-prediction can be explained by the same reasoning of drag force acting on the spherical droplets and inaccurate spray initial conditions. The mean droplet radial velocity (Figure 4.37 and Figure 4.38) compares well with the experimental data at lower elevations but at higher elevations, the droplet radial velocity is under-predicted similar to droplet axial velocity. For both the droplet axial and radial velocity plots, at higher elevations, the larger droplets of size $50\mu\text{m}$ to $60\mu\text{m}$ have not reached the far radial region. This is due to the initial spray conditions used for the simulations which are not able to capture the spread of the droplets. The Sauter Mean Diameter plots from Figure 4.39 show that the droplet diameter prediction is somewhat better for the H_{III} case. From this analysis, the used models and the parameters are able to simulate the H_{III} flame.

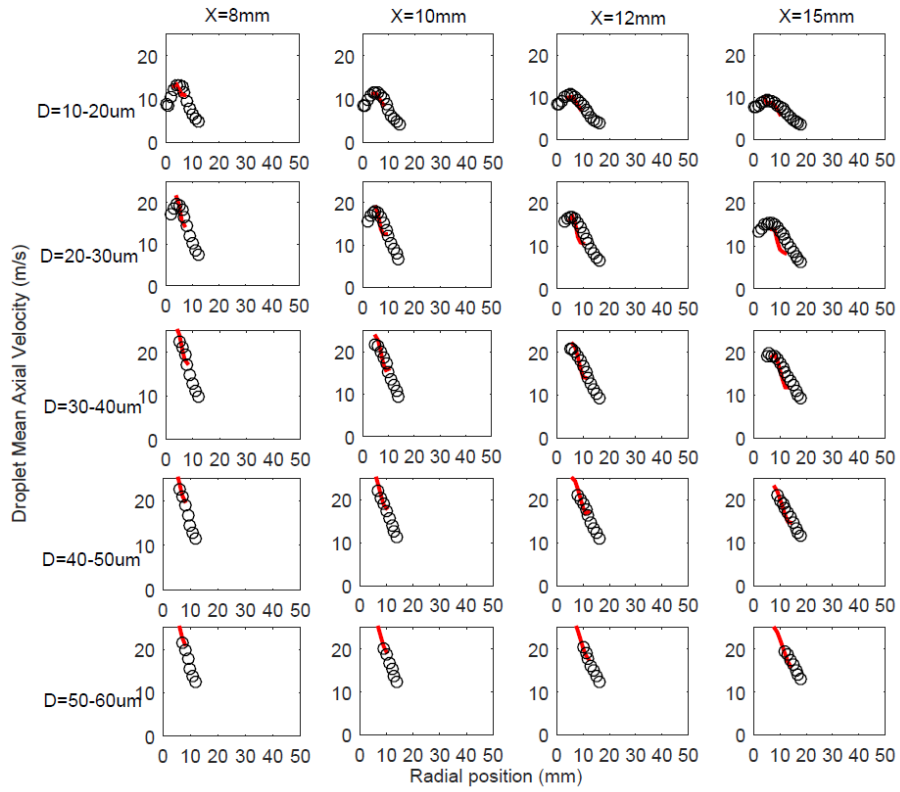


Figure 4.35 Radial profiles of mean droplet axial velocity for elevations of 8mm to 15mm for H_{III} flame with 6.5 bar injection pressure in the injection model

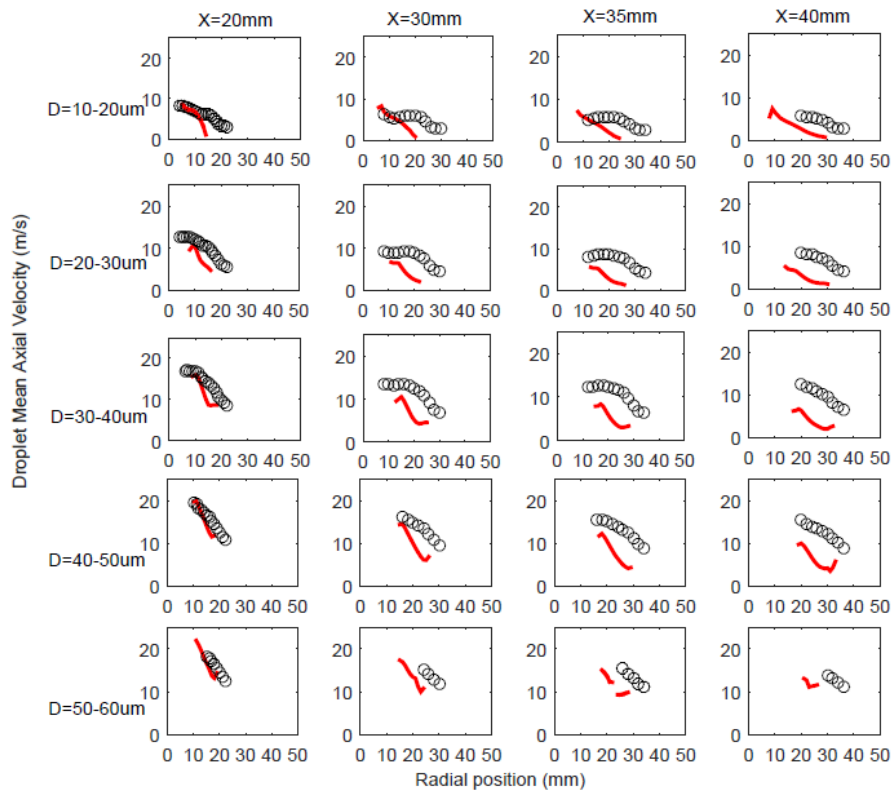


Figure 4.36 Radial profiles of mean droplet axial velocity for elevations of 20mm to 35mm for H_{III} flame with 6.5 bar injection pressure in the injection model

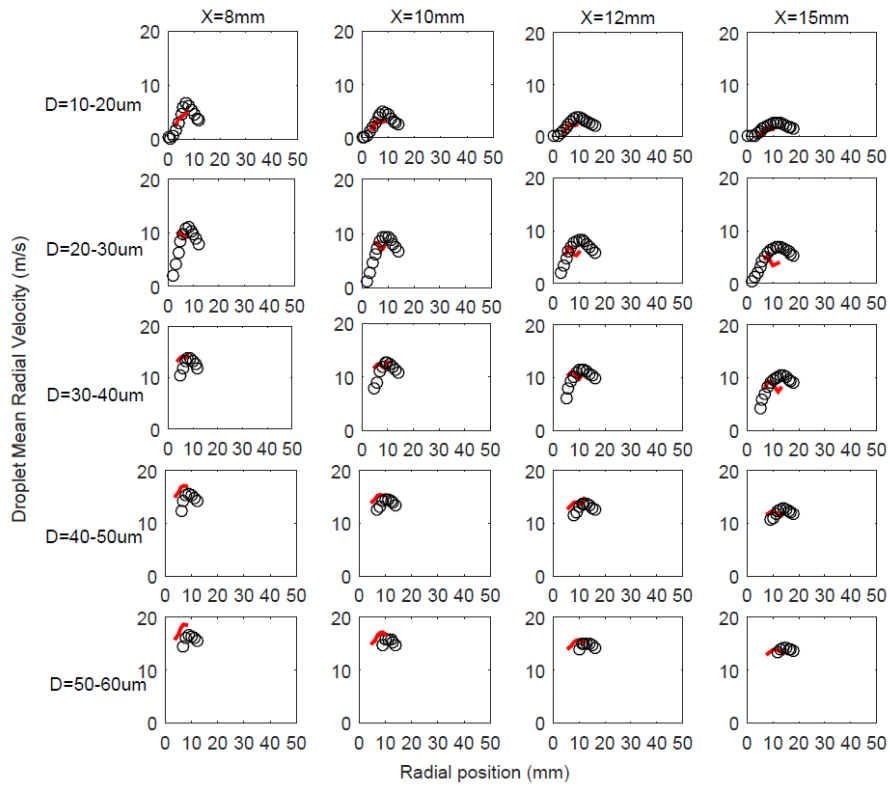


Figure 4.37 Radial profiles of mean droplet radial velocity for elevations of 8mm to 15mm for H_{III} flame with 6.5 bar injection pressure in the injection model

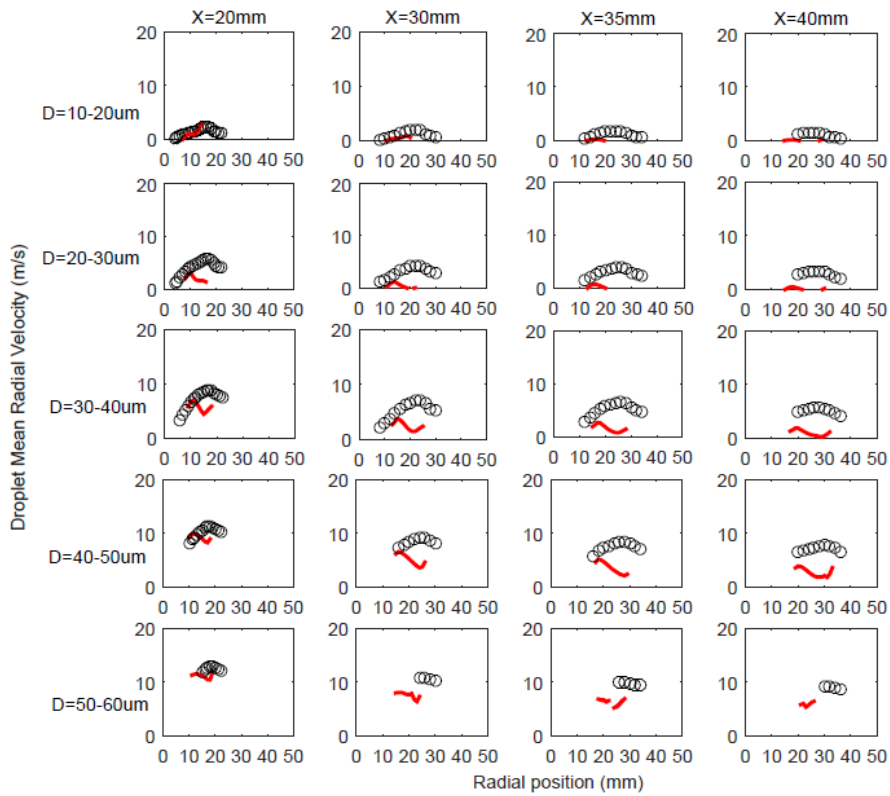


Figure 4.38 Radial profiles of mean droplet radial velocity for elevations of 20mm to 35mm for H_{III} flame with 6.5 bar injection pressure in the injection model

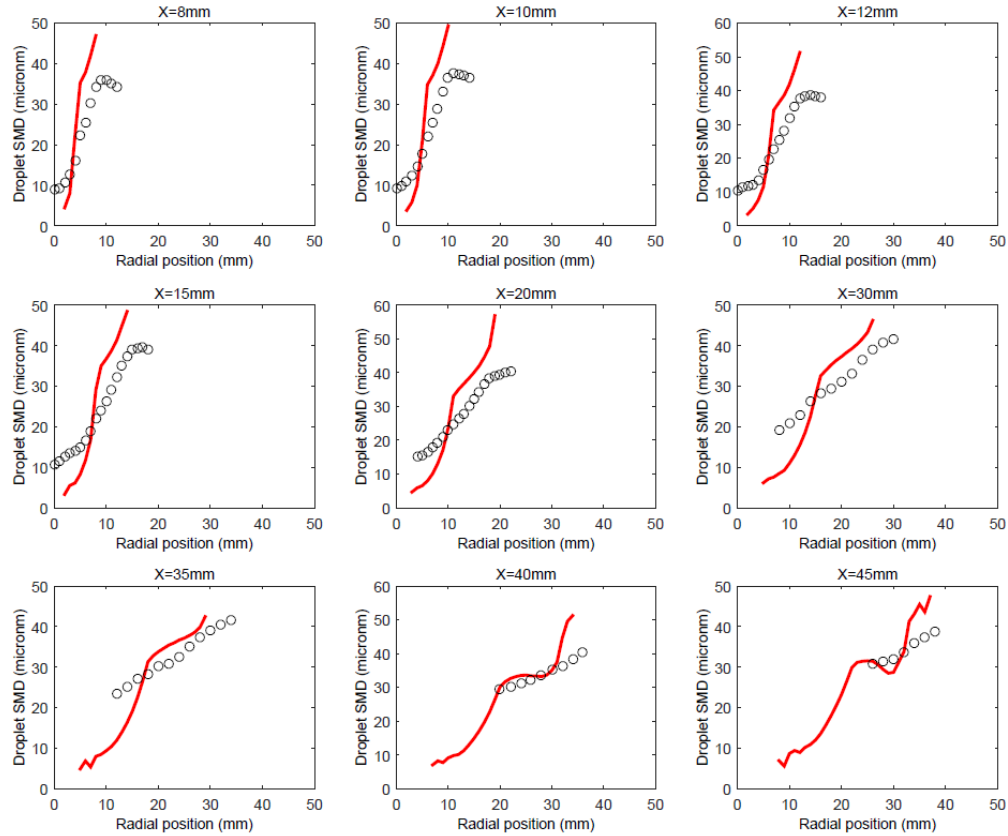


Figure 4.39 Droplet SMD for H_{III} flame with 6.5 bar injection pressure in the injection model

4.4.3 Comparison between H_I , H_{II} and H_{III} flames

The comparison of the gas phase temperature profile for H_I , H_{II} and H_{III} is shown in Figure 4.40. In the experimental data at elevation, $X=40\text{mm}$, the distance between the injector axis and the peak temperature is smaller for the H_I flame compared to the H_{III} flame. Hence the H_{III} flame is wider than H_I flame.

The physical phenomenon behind the wider H_{III} flame is due to higher penetration of droplets at lower coflow temperature (Correia Rodrigues H. , Tummers, Roekaerts, & van Veen, 2015). But in the simulation results, at the axial location of 40mm, we can observe that the H_{III} flame is not wider than H_I flame based on the distance between the peak temperature and injector axis. The wider H_{III} flame phenomenon is not captured well by the combustion model used in this study. This is attributed due to the same spray initial conditions used for all three flames. Even though the gas phase peak temperature is not predicted well by the model, the range of peak temperature is captured well where H_I flame has the highest coflow temperature and H_{III} has the lowest coflow temperature. Also, the three flame simulations predict well the temperature of the gas phase in the far-radial region.

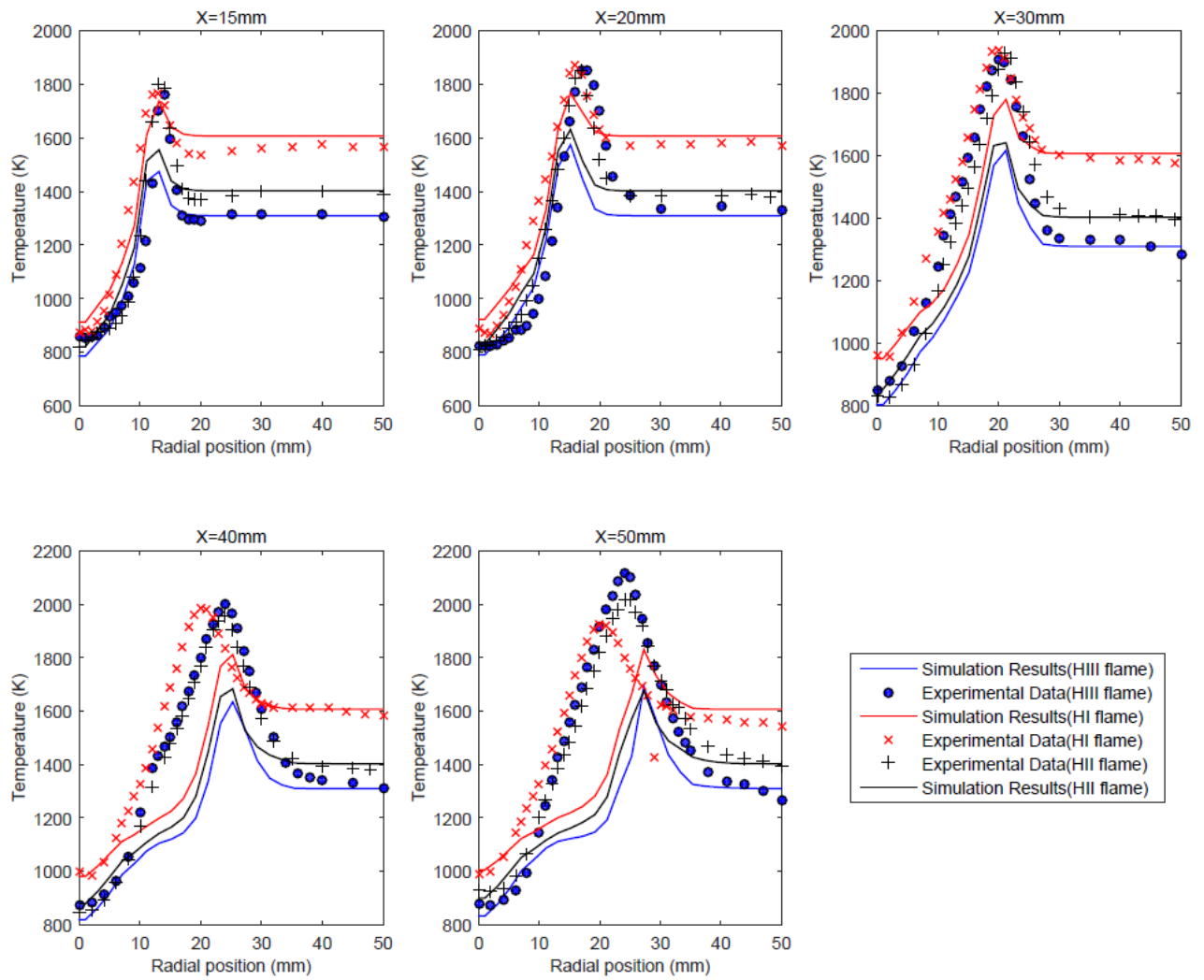


Figure 4.40 Gas phase Temperature profile comparison between H_I , H_{II} and H_{III} flames

Chapter 5

Conclusions and Recommendations

Turbulent spray combustion is a complex process with two phases involved namely the gas phase and the liquid phase. In this thesis work, OpenFOAM was used for the numerical study of ethanol spray flames in a hot-diluted condition (DSHC flame) using RANS approach. An Eulerian-Lagrangian framework was used in the sprayFoam solver with gas phase modeled using Eulerian approach and discrete phase modeled using Lagrangian approach. The interaction between the turbulence and chemical kinetics was modeled by Partially Stirred Reactor (PaSR) combustion model. The two-way coupling between the gas phase and discrete phase was taken into account in the gas phase equations through source terms representing effects of mass, momentum and energy exchange with the discrete phase. The input boundary conditions were specified for the problem using experimental data obtained from DSHC burner experiments.

The ethanol spray combustion was first studied for the hot-diluted coflow case H_{II}. The injection pressure of the liquid fuel was optimized empirically using data on velocity of the droplets and their diameter distribution for calibration. Various injection pressures were analyzed and various droplet properties like mean droplet axial, radial velocity and SMD were studied. From this study, it was found that the droplet velocity and SMD compared best with the experimental data for the injection pressure of 6 bar for the H_{II} case. During this injection pressure optimization study, it was found that at higher axial locations, the droplet axial and radial velocity profiles did not match with the experimental results. The under-predicted droplet velocities at higher elevations were due to droplet velocities being reduced as a result of drag and inertial effects acting on the spherical droplet. This was also attributed to insufficiently accurate initial spray conditions set for the simulations which affect the droplet velocity at higher axial locations. This drawback could be avoided in the future studies by taking into account all available initial spray conditions.

After this pressure optimization, a study on model performance was carried out. The different models affecting the performance of the ethanol spray combustion like evaporation, and turbulence model were studied. The evaporation model is very important in modeling turbulent spray combustion because of its influence in flame structure. Two evaporation models, Gradient diffusion model and Spalding model were compared with the help of gas phase temperature and velocity profiles. From the analysis, we concluded that even though the gas phase temperature prediction was better for Spalding model, the higher evaporation rate of the model resulted in no droplet at higher elevations. As a result, gradient diffusion model was selected for comparative study of different flames. The Spalding model gave a better gas phase temperature prediction since it takes into account, the Stefan flow in its rate equation. The bad performance of the Spalding model found in this study could possibly be avoided by optimizing the initial spray conditions.

Next, a comparison between two turbulence models used for the spray combustion was carried out. Turbulence models analyzed were standard $k-\varepsilon$ model and realizable $k-\varepsilon$ model. The gas phase temperature and velocity plots showed that realizable $k-\varepsilon$ model under-predicted the gas phase temperature. This under-prediction was attributed to the combustion model (PaSR) used in the simulations as the mean source term in PaSR model was calculated based on the turbulent mixing time which is taken proportional to turbulence frequency, ε/k . The velocity profiles followed similar trends for both the models as the mean velocity calculated was similar. Based on these observations, and since PaSR model was taken as a fixed sub-model, standard $k-\varepsilon$ model was used as a better model for the comparative study of the three flames.

A comparison between a detailed reaction mechanism (38 species and 228 reactions by Roehl and Peters (Röhl & Peters, 2009)) and global one step mechanism (K. Westbrook & L. Dryer, 1981) for the oxidation of ethanol was carried out to analyze the effects of detailed chemistry on reaction rate and the temperature distribution (refer Appendix A.1). A qualitative study of both these reaction mechanisms revealed that the gas phase temperature prediction for the detailed reaction mechanism was bad at higher axial locations. This was attributed due to non-converged solutions and the limitations of evaporation model employed for this study. The gas phase velocity prediction for detailed mechanism was also poorer than the global one (refer Appendix A.1 Figure A.3 and Figure A.4). The results could not be compared in detail with each other due to computational time limitations associated with the detailed mechanism. Since computational cost is a major concern in computational studies, global mechanism was preferred over detailed mechanism and used as the default kinetics model throughout this study.

Next, the above selected models were applied to H_I and H_{III} flames with different coflow temperature and dilution and flame behavior. A study of H_I flame using an optimized injection pressure of 6.5 bar was done and the gas phase temperature, gas phase velocity, droplet velocity, SMD was analyzed. It was found that near the injector axis, gas phase temperature was over-predicted. This was due to low evaporation rate of the droplets near the injector region which showed the importance of a need for good evaporation model. The peak gas phase temperature was also under-predicted. This under-prediction was attributed due to the reaction mechanism and combustion model's (PaSR) limitations. The gas phase axial velocity was under-predicted at higher axial locations. In experiments, droplet axial velocity for droplets of size less than $6\mu\text{m}$ was used to approximate gas phase axial velocity. From Figure 4.29, we found that small size droplets at higher axial locations had low velocities. As in experiments, the small sized droplet velocity was approximated to gas phase velocity and hence, the low droplet velocity caused gas phase velocity under-prediction. The mean droplet axial and radial velocities were predicted well except at higher axial locations. The under-prediction of droplet velocities can be explained by the same reasoning as for the H_{II} case. The SMD predictions were in better agreement with experimental data.

When the study of H_{III} flame was carried out with an optimized injection pressure of 6.5 bar, it was found that for the gas phase temperature profiles, the temperature was under-predicted near the nozzle region due to low evaporation in the nozzle region. The peak gas phase

temperature was under-predicted similar to H_I and H_{II} flames. The gas phase velocities were predicted well by the model. The mean droplet axial and radial velocity was predicted well for lower axial locations but higher axial locations called for the need of a better initial spray conditions for the problem. The SMD predictions were in agreement with the experimental data.

A final gas phase temperature comparison for all the three flames was done and it was found that for all the three flames, the temperature in the far radial region is correct. The difference in width of the peak temperature for H_I and H_{III} flames observed in experimental data due to higher droplet penetration was not captured by the numerical model. Also the phenomenon of a weak inner flame front observed in the experiments was not predicted by the RANS simulations. This can only be improved by the use of a better combustion model and good selection of initial spray conditions.

Based on these observations, following recommendations are made for further studies in spray combustion.

Evaporation model plays an important role in defining the flame structure. The shortcomings of evaporation model considered in this study can be overcome by the use of Spalding model for simulations. But in order to get better performance of the Spalding model at higher axial locations, a thorough investigation of initial spray conditions like number of parcels injected, parameters used in Rosin-Rammler size distribution (mean diameter of the droplet, spread parameter, etc) should be performed for sprayFoam solver.

The peak gas phase temperature under-prediction is due to use of global one-step reaction mechanism with turbulence and chemistry interaction modeled by Partially Stirred Reactor (PaSR) model. The results could be improved in the future by implementation of Flamelet Generated Manifold (FGM) combustion model for sprayFoam with detailed reaction mechanism using look-up tables. The main concern in this study was the computational time involved in solving for all the species in a detailed reaction mechanism. The suggested method would significantly reduce the computational time and improve the accuracy of the results.

The effect of atomization model like LISA model on droplet velocity, diameter and distribution should be investigated. Simulations can be expanded to other biofuels like biodiesel and bio methanol to investigate its range of applicability.

All these recommendations should be initially investigated for RANS simulations. Based on the results, it should be judged how to go further with Large Eddy Simulations (LES).

Bibliography

- Realizable k-epsilon model*. (2005). Retrieved July 2015, from CFD-Online: http://www.cfd-online.com/Wiki/Realisable_k-epsilon_model
- Standard k-epsilon model*. (2005). Retrieved July 2015, from CFD-Online: http://www.cfd-online.com/Wiki/Standard_k-epsilon_model
- Agency, I. E. (2010). *World Energy outlook*.
- B.E.Launder, & D.B.Spalding. (1972). *Lectures in mathematical models of turbulence*. London: Academic Press.
- Carlsson, P. (2009). *Tutorial dieselFoam*. Lulea University of Technology.
- Cavalierea, A., & Joannon, M. d. (2004). Mild Combustion. *Progress in Energy and Combustion Science*, 30(4), 329-366.
- Chrigui, M., Masri, A. R., Sadiki, A., & Janicka, J. (2013, June). Large Eddy Simulation of a Polydisperse Ethanol Spray Flame. *Flow, Turbulence and Combustion*, 90(4), 813-832.
- Correia Rodrigues, H., Tummers, M. J., Roekaerts, D. J., & van Veen, E. H. (2015, February). Effects of coflow temperature and composition on ethanol spray flames in hot-diluted coflow. *International Journal of Heat and Fluid Flow*, 309-323.
- Correia Rodrigues, H., Tummers, M. J., Roekaerts, D. J., & van Veen, E. H. (2015, March). Spray flame structure in conventional and hot-diluted combustion regime. *Combustion and Flame*, 162(3), 759-773.
- Durst, F., Melling, A., & Whitelaw, a. J. (1981). *Principles and Practices of Laser*. Academic Press.
- Engineering Toolbox - Fuels and Chemicals - Autoignition Temperatures*. (n.d.). Retrieved June 16, 2015, from Engineering Toolbox: http://www.engineeringtoolbox.com/fuels-ignition-temperatures-d_171.html
- Filho, F. L., Fukumasu, N. K., & Krieger, G. C. (2013). Numerical simulation of an ethanol turbulent spray flame with RANS and diffusion combustion model. *The Brazilian Society of Mechanical Sciences and Engineering*, 35, 189-198.
- Forums, C.-O. (n.d.). *CFD-Online*. Retrieved July 20, 2015, from CFD-Online: <http://www.cfd-online.com/Forums/openfoam-solving/145903-sprayfoam-thetaouter-thetainner.html>
- Golovitchev, V. I., & Nordin, N. (2001). Detailed Chemistry Spray Combustion Model for the KIVA Code. *International Multidimensional Engine Modeling*. Detroit: SAE Congress.

- Greenshields, C. J. (2015, May). OpenFOAM User guide and Programmer's guide.
- H.K.Versteeg, & W.Malalasekera. (2007). *An Introduction to Computational Fluid Dynamics*. Essex: Pearson Education Limited.
- Haynes, W. M. (Ed.). (2015-2016). CRC Handbook of Chemistry and Physics.
- Heye, C. R., Kourmatzis, A., Raman, V., & Masri, & A. (2014). A Comparative Study of the Simulation of Turbulent Ethanol Spray Flames. In B. Merci, & E. Gutheil, *Experiments and Numerical Simulations of Turbulent Combustion of Diluted Sprays* (pp. 31-54). Springer.
- Jamali, S. H. (2014). *Computational Modeling of Turbulent Ethanol Spray Flames in a Hot Diluted Coflow*. Delft: Master Thesis, TU Delft.
- Jenny, P., Roekaerts, D., & Beishuizen, N. (2012, December). Modeling of turbulent dilute spray combustion. *Progress in Energy and Combustion Science*, 38(6), 846-887.
- Joannon, M. D., Saponaro, A., & Cavaliere, A. (2000). Zero Dimensional Analysis of Diluted Oxidation of Methane in Rich Conditions. *Proceedings of the Combustion Institute*, 28, 1639-1646.
- K.Westbrook, C., & L.Dryer, F. (1981). Simplified Reaction Mechanisms for the Oxidation of Hydrocarbon Fuels in Flames. *Combustion Science and Technology*, 27, 31-43.
- Karrholm, F. P. (2008). *Numerical Modelling of Diesel Spray Injection, Turbulence Interaction and Combustion*. Goteborg: Chalmers University of Technology.
- Katsuki, M., & Hasegawa, T. (1998). The Science and Technology of Combustion in Highly Preheated Air Combustion. *Proceedings of the Combustion Institute*, 27, 3135-3146.
- L.Dryer, F., & K.Westbrook, C. (1981). Simplified Reaction Mechanisms for the oxidation of Hydrocarbon Fuels in Flames. *Combustion Science and Technology*, 27, 31-43.
- M.Marinov, N. (1998). A Detailed Chemical Kinetic Model for High Temperature Ethanol Oxidation. *International Journal of Chemical Kinetics*, 31, 183-220.
- Ma, L., Naud, B., & Roekaerts, D. (2015). Transported PDF Modeling of Ethanol Spray in Hot-Diluted Coflow Flame . *Flow, Turbulence and Combustion*, 1-34.
- Ma, L., Zhu, S., Correia Rodrigues, H., Tummers, M. J., Roekaerts, D. J., & van der Meer, T. (2013). Numerical Investigation of Ethanol Spray-in-Hot-Coflow Flame Using Steady Flamelet Model. *8th Mediterranean Combustion Symposium*. Izmir, Turkey.
- Masri, A. R., & Gounder, & J. (2010). Turbulent Spray Flames of Acetone and Ethanol Approaching Extinction. *Combustion Science and Technology*, 182(4-6).

- Merci, B., Roekaerts, D., & Sadiki, A. (2011). Experiments and Numerical Simulations of Diluted Spray Turbulent Combustion. *Proceedings of the 1st International Workshop on Turbulent Spray Combustion*. Springer.
- Milani, A., & Wüning, J. (2002, April). Retrieved from IFRF Online Combustion Handbook: <http://www.handbook.ifrf.net/handbook/cf.html?id=171>
- Miller, R. S., Harstad, K., & Bellan, J. (1998). Evaluation of equilibrium and non-equilibrium evaporation models for many-droplet gas-liquid flow simulations. *International Journal of Multiphase Flow*, 1025-1055.
- Nelson, R. (2014). *Environmental Science for the European Refining Industry*. Concawe.
- OpenCFD. (n.d.). *OpenFOAM Features*. Retrieved from OpenFOAM: <http://www.openfoam.org/features/>
- Poinsot, T., & Veynante, D. (2011). *Theoretical and numerical combustion*. Toulouse: CNRS.
- Rochaya, D. (2007). *Numerical simulation of spray combustion using bio-mass derived liquid fuels*. PhD Thesis, Cranfield.
- Röhl, O., & Peters, N. (2009). A Reduced Mechanism for Ethanol Oxidation. *4th European Combustion Meeting, Vienna University of Technology*. Vienna, Austria.
- S.Sazhin, S. (2006). Advanced models of fuel droplet heating and evaporation. *Progress in Energy and Combustion Science*, 162-214.
- Spalding, D. (1953). The Combustion of Liquid Fuels. *Proceedings of the 4th Symposium (International) on Combustion* (pp. 847-864). Pittsburgh: The Combustion Institute.
- Stiesch, G. (2013). *Modeling Engine Spray and Combustion Processes*. Springer.
- Surfsara. (2013). *Cartesius: the Dutch supercomputer*. Retrieved 2015, from Surfsara: <https://userinfo.surfsara.nl/systems/cartesius>
- Warnatz, J., & Maas, U. &. (2006). *Combustion : Physical and Chemical Fundamentals, Modeling and Simulation, Experiments, Pollutant Formation* (4th ed.). Berlin: Springer.
- Wüning, J., & Wüning, J. (1997). Flameless oxidation to reduce thermal NO-formation. *Progress in Energy and Combustion Science*, 23(1), 81-94.
- Zuo, B., A.M.Gomes, & C.J.Rutland. (2000). Studies of Superheated Fuel Spray Structures and Vaporization in GDI Engines. *Eleventh International Multidimensional Engine Modeling User's Group Meeting*.

Appendix

A.1 Model comparison for Chemical kinetics

In this section, the influence of the type of reaction mechanisms used for the combustion of ethanol is analyzed based on the number of reactions solved by the spray combustion solver. The different parameters analyzed are the relevant gas phase temperature profiles and the gas phase velocity profiles (axial and radial velocity). The analysis is done based on a qualitative comparison since the detailed reaction mechanism employed (38 species and 228 reactions by Roehl and Peters (Röhl & Peters, 2009)) consumes a significant amount of computational time as the solver has to solve all the 38 chemical species.

The detailed mechanism simulations are run on 240 CPU cores of supercomputer, Cartesius (Surfsara, 2013) using parallel computing for one day and continued on local computer with 6 cores for 15 days to get results up to a simulation time of 0.03s. The computational time for the one-step mechanism run on 6 CPU cores of local computer for the same simulation time (0.03s) is around 5 hours. As a result, the comparison study for both the global and detailed mechanisms is done until this time step. Therefore, we can obtain only a tentative conclusion from the plots.

The solution convergence for the detailed mechanism is shown with the help of gas phase temperature and ethanol mass fraction plotted as a function of simulation time. From these plots, we will be able to see if the values initially change as a function of time and in time reach steady state (solution convergence for unsteady simulations).

From Figure A.1 and Figure A.2, we can see that up to an elevation of 30mm, the solution convergence for both the gas phase temperature and ethanol mass fraction starts after a simulation time of 0.025s. But for higher locations, we can observe that the solution is not converged yet even after a simulation time of 0.03s. So after analyzing the convergence plots for one-step mechanism (Figure 3.1, Figure 3.2 and Figure 3.3), we can observe that a good comparison between the one-step mechanism and detailed mechanism can be done up to an elevation of 30mm since at these elevations both the mechanisms have almost converged solutions from a simulation time of 0.025s.

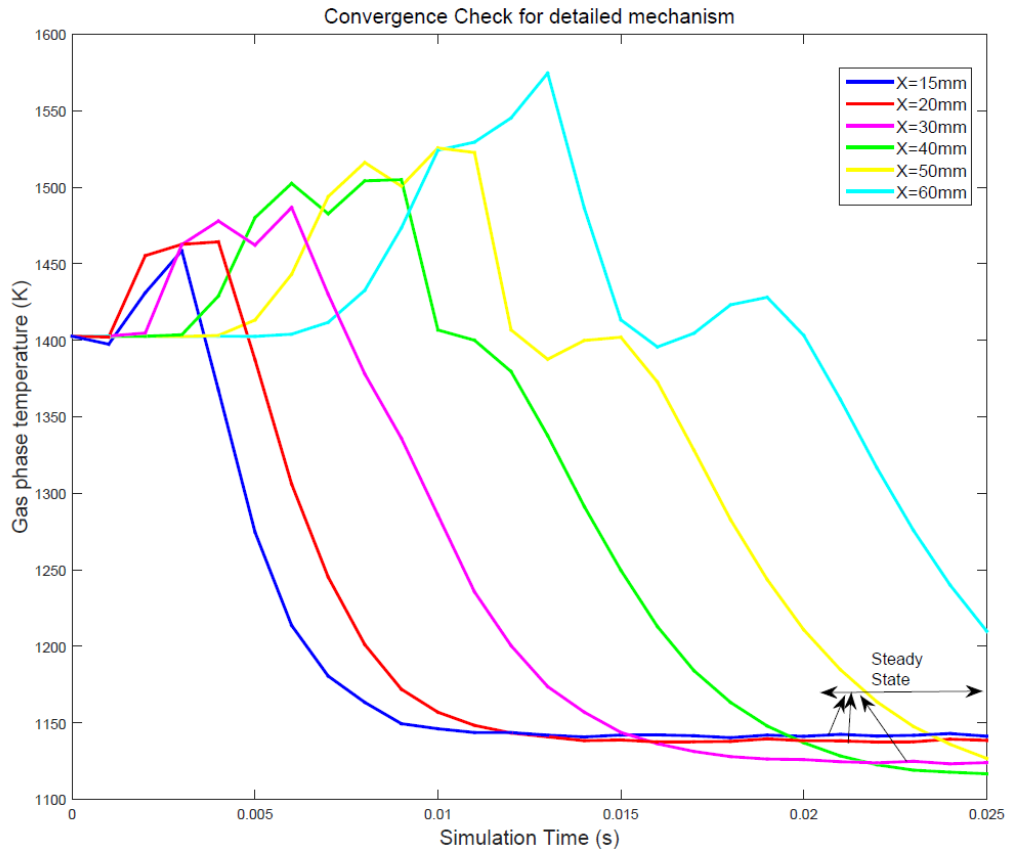


Figure A.1 Gas phase temperature convergence plot for detailed mechanism

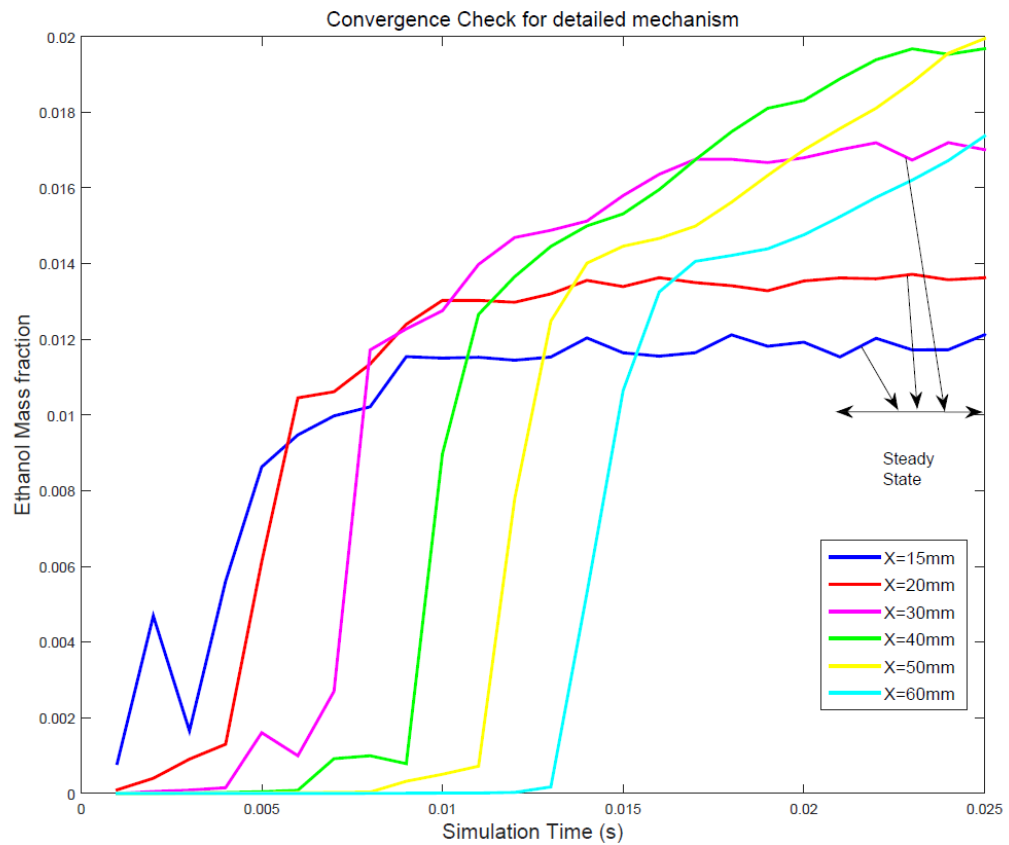


Figure A.2 Ethanol mass fraction convergence plot for detailed mechanism

The gas phase temperature profiles for different elevations are shown in Figure A.3. From the figure, we can see that the gas phase temperature profiles for both global reaction mechanism and detailed mechanism are predicted well at lower axial locations, with detailed mechanism giving results closer to experimental data.

The temperature is over-predicted in the spray centerline (injector axis). This effect is stronger for the simulation using the detailed mechanism. This over-prediction is due to the evaporation model involved in which the droplets have not yet evaporated near the injector axis. This is also evident from the high axial gas phase velocity near the injector axis in Figure A.4.

We can conclude that even though this is only a qualitative comparison, the global reaction mechanism gives slightly more accurate results. Also the lower computational cost is an advantage. Therefore, the global mechanism will be used for the study of H_I and H_{III} flames.

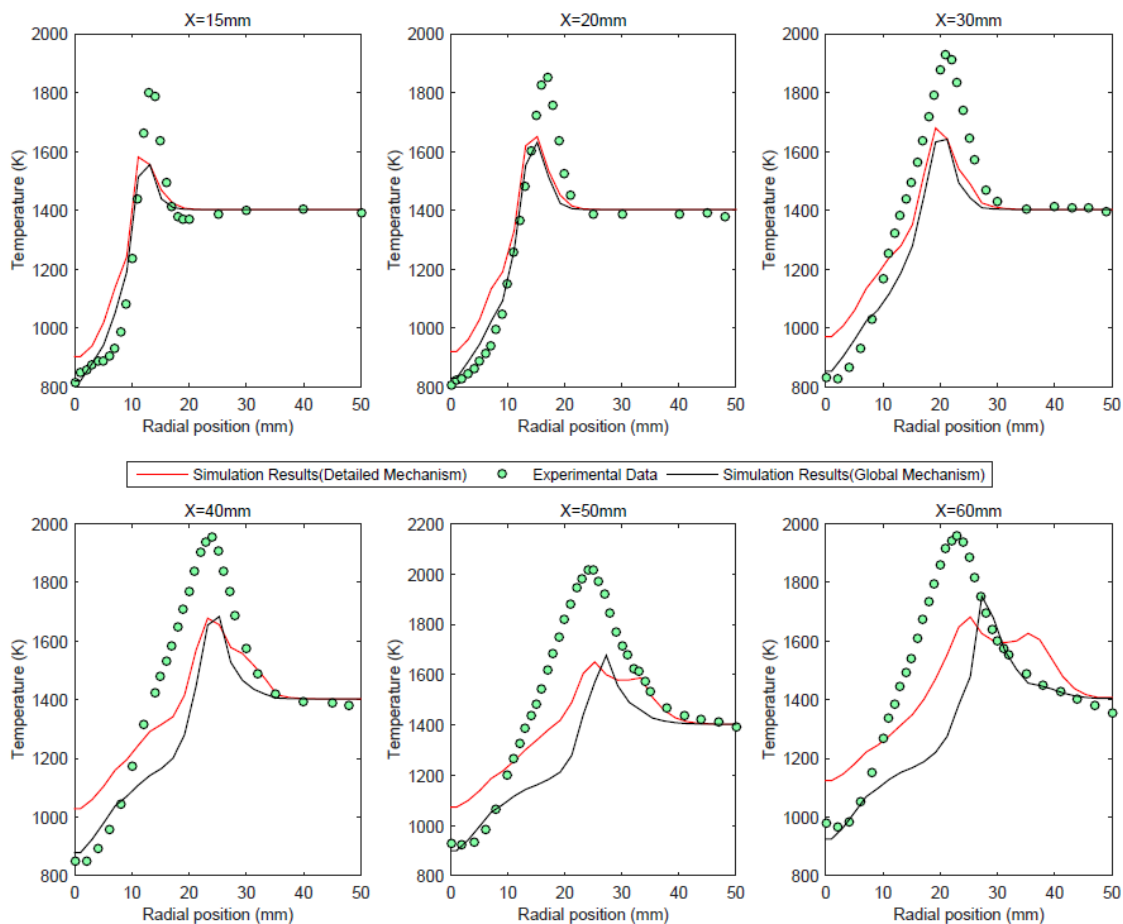


Figure A.3 Gas phase Temperature profile comparison for the reaction mechanisms at different elevations

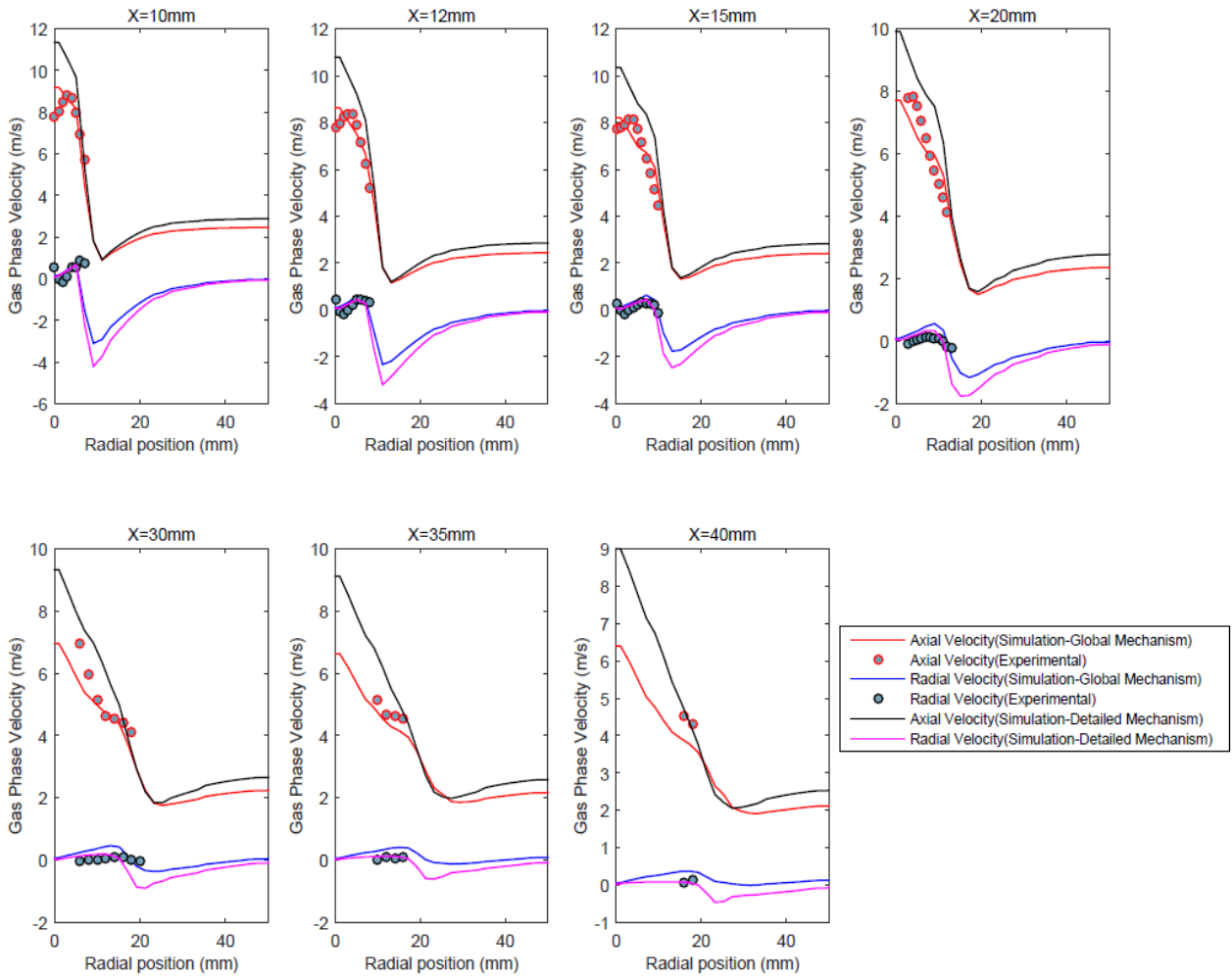


Figure A.4 Gas phase velocity profile comparison for the reaction mechanisms at different elevations

A.2 Pressure optimization with Spalding Evaporation model

The droplet velocity and diameter profiles for the pressure optimization done for 10 bar case of H_{II} flame with Spalding evaporation model is presented here. The droplet axial velocity profiles are given in Figure A.5 and Figure A.6. From the plots, we can see that the droplet axial velocities are over-predicted at all axial locations for the given size range of droplets. Also at higher axial locations, the droplets are not present due to high evaporation rate found in the Spalding model. The droplet radial velocity profiles in Figure A.7 and Figure A.8 also follow the same trend as the axial velocity profiles. The SMD profile for the case (Figure A.9) is under-predicted with respect to the experimental data.

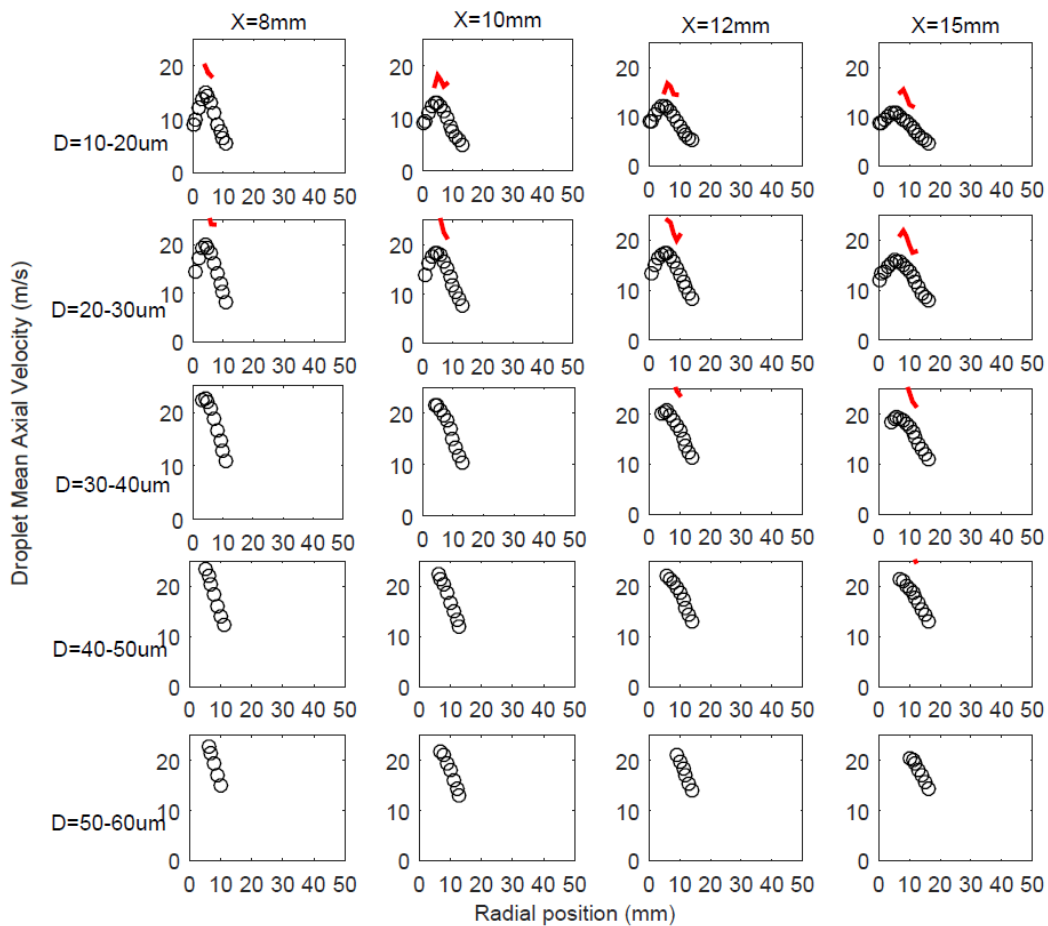


Figure A.5 Radial profiles of mean droplet axial velocity for elevations of 8mm to 15 mm at 10 bar injection pressure in the injection model with Spalding model

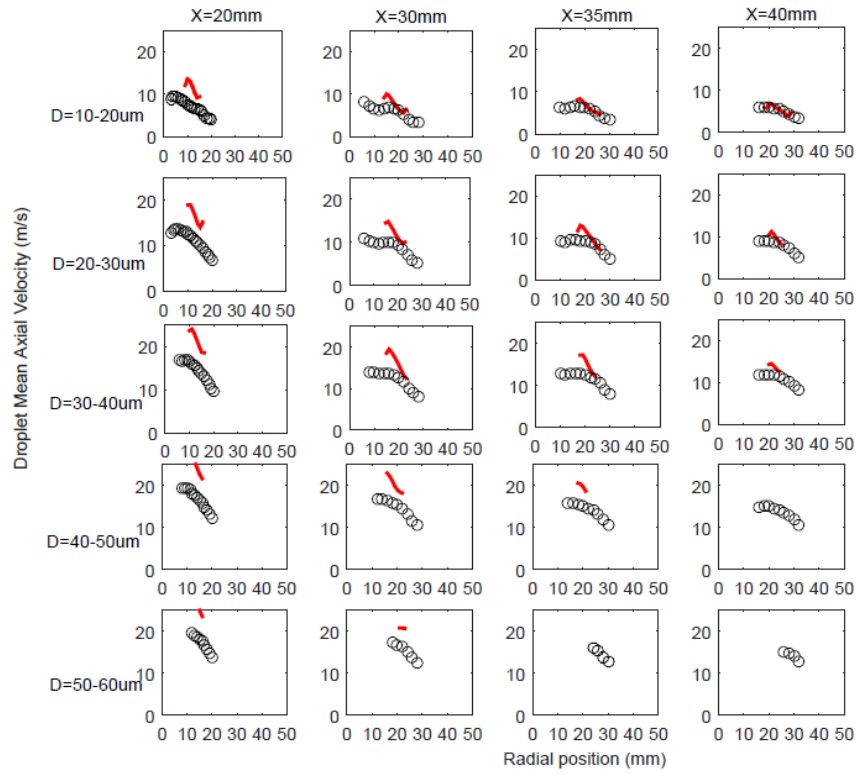


Figure A.6 Radial profiles of mean droplet axial velocity for elevations of 20mm to 40mm at 10 bar injection pressure in the injection model with Spalding model

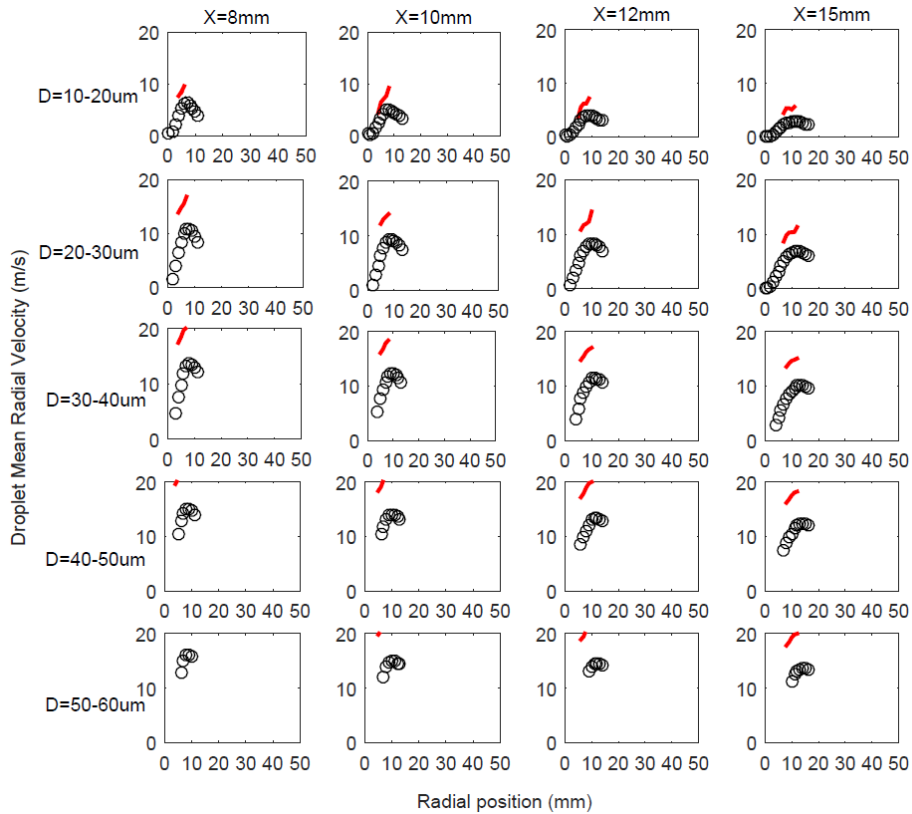


Figure A.7 Radial profiles of mean droplet radial velocity for elevations of 8mm to 15 mm at 10 bar injection pressure in the injection model with Spalding model

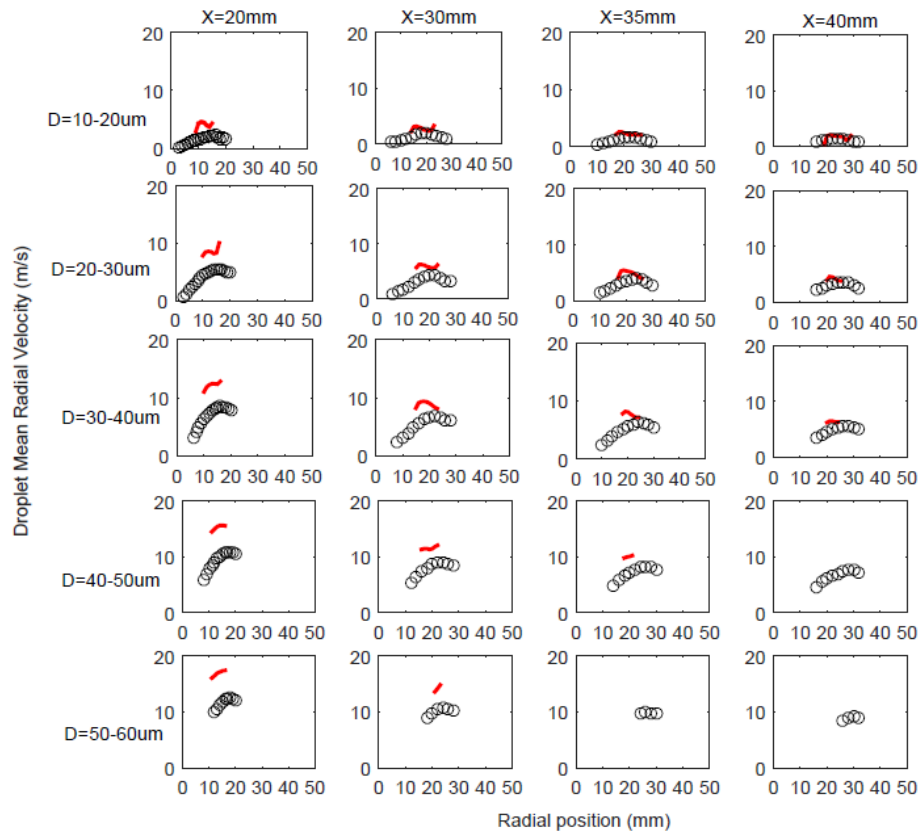


Figure A.8 Radial profiles of mean droplet radial velocity for elevations of 20mm to 40mm at 10 bar injection pressure in the injection model with Spalding model

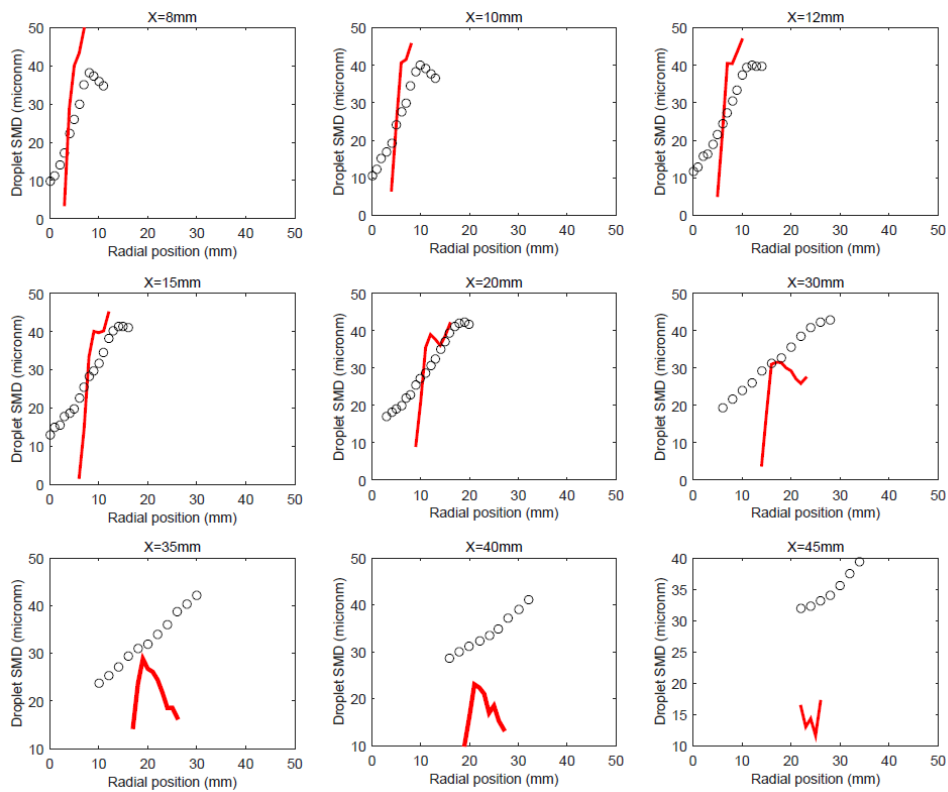


Figure A.9 SMD for the Spalding model with 10 bar injection pressure in the injection model

A.3 Spray properties used in simulations

Spray properties of H_{II} flames used for the simulations in OpenFOAM (Similar setup follows for H_I and H_{III}).

```

/*----- C++ -----*\
|=====|
| \ / Field | OpenFOAM: The Open Source CFD Toolbox |
| \ / Operation | Version: 2.3.0 |
| \ / A nd | Web: www.OpenFOAM.org |
| \ / M anipulation |
\*-----*/
FoamFile
{
    version 2.0;
    format binary;
    class dictionary;
    location "constant";
    object SprayCloudProperties;
}
// ***** //

solution
{
    active true;
    coupled true;
    transient yes;
    cellValueSourceCorrection on;
    maxCo 0.3;

    sourceTerms
    {
        schemes
        {
            rho explicit 1;
            U explicit 1;
            Yi explicit 1;
            h explicit 1;
            radiation explicit 1;
        }
    }

    interpolationSchemes
    {
        rho cell;
        U cellPoint;
        thermo:mu cell;
        T cell;
        Cp cell;
    }
}

```

```

    kappa    cell;
    p        cell;
}

integrationSchemes
{
    U        Euler;
    T        analytical;
}
}

constantProperties
{
    T0       300;
    rho0     785.12;
    Cp0      2460;

    constantVolume false;
}

subModels
{
    particleForces
    {
        sphereDrag;
    }

    injectionModels
    {
        model1
        {
            type        coneNozzleInjection;
            SOI         0;
            massTotal   4.06e-03;
            parcelBasisType mass;
            injectionMethod disc;
            flowType    pressureDrivenVelocity;
            outerDiameter 2.1e-4;
            innerDiameter 0;
            duration    10;
            position    ( 0 0 0 );
            direction   ( 1 0 0 ); //Injection in x-direction
            parcelsPerSecond 20000000;
            flowRateProfile table
            (
                (0        4.06e-04)
                (10       4.06e-04)
            );
        }
    }
}

```

```

Cd          constant 0.9;
Pinj       constant 6e+05;

thetaInner  constant 30.0;
thetaOuter  constant 45.0;

sizeDistribution
{
    type     RosinRammler;

    RosinRammlerDistribution
    {
        minValue    1e-06;
        maxValue    8e-05;
        d           0.00015;
        n           3;
    }
}

dispersionModel stochasticDispersionRAS;

patchInteractionModel standardWallInteraction;

heatTransferModel RanzMarshall;

compositionModel singlePhaseMixture;

phaseChangeModel liquidEvaporation; //liquidEvaporationBoil

surfaceFilmModel none;

atomizationModel none;

breakupModel ReitzDiwakar;

stochasticCollisionModel none;

radiation    off;

standardWallInteractionCoeffs
{
    type      rebound;
}

RanzMarshallCoeffs
{
    BirdCorrection true;
}

```

```

}

singlePhaseMixtureCoeffs
{
  phases
  (
    liquid
    {
      C2H5OH      1;
    }
  );
}

liquidEvaporationCoeffs //liquidEvaporationBoilCoeffs
{
  enthalpyTransfer enthalpyDifference;

  activeLiquids ( C2H5OH );
}

ReitzDiwakarCoeffs
{
  solveOscillationEq yes;
  Cbag      6;
  Cb       0.785;
  Cstrip    0.5;
  Cs       10;
}

}

cloudFunctions
{}

// *****

```